UNIVERSITY OF BELGRADE

FACULTY OF PHYSICS

Jakša Vučičević

SIGNATURES OF HIDDEN QUANTUM CRITICALITY IN THE HIGH-TEMPERATURE CHARGE TRANSPORT NEAR THE MOTT TRANSITION

Doctoral dissertation

Belgrade, 2015.

УНИВЕРЗИТЕТ У БЕОГРАДУ
ФИЗИЧКИ ФАКУЛТЕТ

Јакша Вучичевић

ПОКАЗАТЕЉИ СКРИВЕНЕ КВАНТНЕ КРИТИЧНОСТИ У ВИСОКО-ТЕМПЕРАТУРНОМ ТРАНСПОРТУ НАЕЛЕКТРИСАЊА У БЛИЗИНИ МОТОВОГ ПРЕЛАЗА

Докторска дисертација

Београд, 2015.

Thesis advisor, Committee member:
Dr. Darko Tanasković
Associate Research Professor
Institute of Physics Belgrade
University of Belgrade

Committee member:
Dr. Zoran Radović
Professor
Faculty of Physics
University of Belgrade

Committee member:
Dr. Đorđe Spasojević
Associate Professor
Faculty of Physics
University of Belgrade

Committee member:
Dr. Mihajlo Vanević
Assistant Professor
Faculty of Physics
University of Belgrade

Committee member:
Dr. Nenad Vukmirović
Associate Research Professor
Institute of Physics Belgrade
University of Belgrade

To my family

Acknowledgemets

Signatures of Hidden Quantum Criticality in the High-temperature Charge Transport Near the Mott Transition

Abstract

The Mott metal-insulator transition is one of the hallmarks of strong electronic correlation and is one of the most active areas of condensed matter research today. Both the experimental data and theory clearly show that the Mott transition is a first order transition, featuring a coexistence region up to some critical temperature T_c. The vicinity of the critical point has been studied extensively and is shown to display critical phenomena of the classical Ising universality class. Below T_c, the first order transition separates a paramagnetic Mott insulator and a paramagnetic metal. At lowest temperature, the two phases often develop long-range order - antiferromagnetism or superconductivity. The Mott transition separates two distinct phases all the way down to zero temperature, which makes it a quantum phase transition.

The open questions regarding the Mott transition include: can Mott mechanism in some cases produce a phenomenology drastically different from that of a first order transition? Can T_c be brought down to zero, i.e. can Mott transition be reduced to a single quantum critical point? The theory suggests that these are quite possible, but a clear experimental verification of such prediction is still lacking. Can a Mott transition be completely hidden by a superconducting ordering instability, and can critical fluctuations of a Mott transition provide a boost to the Cooper pairing mechanism? These questions are of utmost importance, but are notoriously hard to answer. Is there a universal high-temperature behavior in connection with the Mott transition, as is usually the case with other quantum phase transitions? Here we investigate this possibility and show that the answer is positive. Furthermore, we show that the linear temperature dependence of resistivity often found in the incoherent (bad metal) transport regime can be understood as the general consequence of the Mott quantum criticality.

In this thesis we numerically solve the single-site dynamical mean field (DMFT) equation for the Hubbard model, using the iterative perturbation theory (IPT) and continuous time quantum Monte Carlo (CTQMC). We focus on the supercritical

(crossover) regime of the Mott transition, which is precisely where DMFT is expected to work best - non-local effects have been thoroughly shown not to play a role when temperature is high. We calculate resistivity with high resolution throughout the phase diagram and perform a thorough analysis of the data. We first show that there is an "instability trajectory" $U^*(T)$ in the crossover region of the phase diagram, revealing a fundamental distinction between metallic-like and insulating-like behavior, and providing a continuation of the first-order transition line to the supercritical temperatures. Then, we perform a scaling analysis of the resistivity data (as routinely employed in the context of purely quantum phase transitions), to demonstrate the validity of a scaling law with temperature T in the scaling argument, rather than the distance from the critical point $|T - T_c|$. The observed scaling $\rho = \rho(U^*(T), T) \, F((U - U^*(T))/T^{1/z\nu})$ is found to be of high quality, and is corroborated by very recent experimental results on organic Mott insulators.

In the second part of our work, we focus on the doping-driven Mott transition and complete the 3D (μ, U, T) phase diagram of single-site DMFT. We document the quick reduction of T_c as U is increased and extend our scaling analysis to the case when T_c is very small. Here the chemical potential μ rather than on-site interaction U enters the scaling law $\rho = \rho(\mu^*(T), T) \, F((\mu - \mu^*(T))/T^{1/z\nu})$. We show that the phenomenology of the Mott transition resembles that of a quantum critical point and associate the corresponding quantum critical region with the linear resistivity bad metal regime. Starting from the scaling hypothesis, we derive a semi-analytic formula able to reproduce both the linearity and slope of the resistivity curves in the high-temperature part of the full DMFT result, which is found to be in good qualitative agreement with the experiment on the famous cuprate compound $\mathrm{La_{2-x}Sr_xCuO_4}$.

Keywords: strong correlations, Mott metal-insulator transition, quantum criticality, dynamical mean field theory

Scientific field: Physics

Research area: Condensed matter physics

UDC number: 538.9

Показатељи скривене квантне критичности у високо-температурном транспорту наелектрисања у близини Мотовог прелаза

Сажетак

Мотов метал-изолатор прелаз је једна од најважнијих последица јаких електронских корелација, и једна од најактивнијих области истраживања у физици кондензоване материје. И експеримент и теорија јасно указују да је Мотов прелаз фазни прелаз првог реда и да испољава коегзистенцију фаза до неке критичне температуре T_c. Транспортне и термодинамичке особине у околини критичне тачке су детаљно проучаване и показало се да могу да се опишу теоријом класичних фазних прелаза Изингове класе универзалности. Испод T_c, фазни прелаз првог реда раздваја парамагнетни Мотов изолатор и парамагнетни метал. На најнижим температурама, обе фазе често развијају дугодометно уређење - антиферомагнетизам или суперпроводност. Мотов прелаз раздваја две различите фазе све до нулте температуре што га чини квантним фазним прелазом.

Нека од важних отворених питања везаних за Мотов прелаз укључују: да ли Мотов механизам може у неким случајевима да произведе феноменологију драстично различиту од фазног прелаза првог реда? Да ли T_c може да се спусти у нулу, тј. може ли се Мотов прелаз свести на квантну критичну тачку? Теорија сугерише да је ово могуће, али таква предвиђања још увек чекају на неоспорну експерименталну потврду. Може ли Мотов прелаз да буде комплетно сакривен суперпроводном фазом, и могу ли критичне флуктуације везане за Мотов прелаз да допринесу Куперовом спаривању? Ова питања су од великог значаја, али је на њих још увек немогуће потпуно одговорити. Постоји ли универзално понашање на високој температури, повезано са Мотовим прелазом, какво се често опажа у контексту квантних ($T = 0$) фазних прелаза? Овде истражујемо такву могућност и налазимо позитиван одговор. Такође, показујемо да се линеарна температурна зависност отпорности, често опажена у некохерентном режиму транспорта, може разумети као универзална последица Мотове квантне критичности.

У овој тези нумерички решавамо једначину теорије динамичког средњег

поља за Хабардов модел (DMFT), користећи итеративни пертурбативни метод (IPT) и квантни Монте Карло метод у континуалном времену (CTQMC). Концентришемо се на прелазни високотемпературни режим између метала и изолатора, што је управо режим где су нелокалне корелације занемарљиве, па је и ДМФТ оправдана апроксимација. Рачунамо проводност са високом резолуцијом широм фазног дијаграма и детаљно анализирамо резултате. Прво показујемо да постоји "линија нестабилности" $U^*(T)$ у надкритичном делу фазног дијаграма, која открива суштинску поделу између металичног и изолаторског понашања, и представља продужетак линије фазног прелаза првог реда на надкритичне температуре. Онда, спроводимо анализу скалирања резултата за отпорност (како се то иначе чини у случају чисто квантних фазних прелаза) да бисмо утврдили важење законитости са температуром T у аргументу уместо удаљености од критичне тачке $|T - T_c|$. Пронађено скалирање $\rho = \rho(U^*(T), T) F((U - U^*(T))/T^{1/z\nu})$ је високог квалитета, и потврђено је у недавном експерименту на органским Мотовим изолаторима.

У другом делу рада, концентришемо се на Мотов прелаз изазван допирањем и употпуњавамо тродимензионални (μ, U, T) фазни дијаграм. Документујемо убрзано смањивање T_c како се повећава интеракција U и користимо нашу анализу скалирања у случају када је T_c врло мало. Сада хемијски потенцијал μ уместо јачине интеракције U улази у закон скалирања $\rho = \rho(\mu^*(T), T) F((\mu - \mu^*(T))/T^{1/z\nu})$. Показујемо да је Мотов прелаз повезан са универзалним високо-температурним понашањем типичним за квантне критичне тачке, и да се оно поклапа са режимом лошег метала са линеарном отпорношћу. Крећући од претпоставке о важењу скалирања, изводимо полу-аналитичку формулу која репродукује и линеарност и нагиб кривих отпорности у високо-температурном делу пуног DMFT резултата, који је у добром квалитативном слагању са експериментом на познатом једињењу бакар-оксида $La_{2-x}Sr_xCuO_4$.

Contents

1. Introduction

The many-body problem is arguably the single most important problem, not only in physics, but in biology/neuroscience, social science and finance. The phenomenon of emergence is so universally present, that it is impossible to even try and envision the possible gain from a better and possibly systematic understanding of complex systems. In physics, however, one deals with elementary particles which are only few in type, with well defined properties and amazingly simple interactions. This poses an unprecedented opportunity to actually work out and test theories that predict emergent behavior. The study of the many-body problem arising in condensed matter systems is, indeed, not without success. It made clear that quantum nature of the elementary constituents of matter becomes so dominant at low temperature, that it is often easily observable even on the macroscopic scales. The quantum uncertainty, entanglement and exchangeability of particles are identified as very powerful mechanisms, able to give rise to phases of matter so exotic, that they are unmatched by anything in our everyday experience of the world. A bosonic superfluid creeps out of any container, and superconducting materials seemingly violate the firmest notion that energy must always dissipate - it is a fundamental and invaluable insight, that already pairwise correlation between electrons can produce a drastic effect which is superconductivity. It is therefore of primary importance to understand the seemingly endless variety of ways quantum particles can self-organize into a collective state, and try to identify general mechanisms which lead to behavior qualitatively different from that of an ensemble of mutually non-interacting particles.

The study of condensed matter theory has brought us some very useful rules of thumb. For a system to have exotic properties, it is not sufficient that there are interactions. Interactions are a built-in property of all particles, yet most of the materials are just boring chunks of matter. Interactions get screened and most of the systems can be described using an effective single-particle picture. The conventional material is either a metal or an insulator, and this can be predicted with as

little information as is the occupancy of the valence band. What turns out to be important is that there are competing energy scales - an ambiguity in what is the energetically favorable state of the system. While the research of ordered phases is an important part of condensed matter study, the most interesting phenomena seem to go hand in hand with instability of the order. It is on the verge of a transition from an anti-ferromagnetic insulator to a paramagnetic metal that cuprate compounds exhibit superconductivity at remarkably high temperatures [1, 2, 3]. It is now widely accepted that in the vicinity of a phase transition most interesting stuff happens. At precisely the quantum critical point (QCP) systems are so indecisive of what should be their ground state, that fluctuations appear at all time and length scales. Quantum critical fluctuations may in some cases carry an effective interaction between particles, such that it produces non-trivial correlations and an emergent order of unpredicted macroscopic signature.

The most appealing aspect of quantum critical points is that they seem to display a high degree of universality [4, 5]. The finite temperature crossover region is completely dominated by the presence of a $T = 0$ quantum critical point, and this is embodied in scaling laws, as documented in numerous experiments on various systems [6, 7, 8, 9, 10, 11]. The study of phenomena associated with quantum critical points is one of the most exciting fields in condensed matter theory today. QCP's are important from the view of possible technological application, but they also prove to be a very useful playground for tackling the fundamental questions, not only in condensed matter theory, but gravity and string theory as well. The physics precisely at the QCP can be described by a conformal field theory, and as such is ideal for testing the AdS/CFT correspondence conjecture, which is an immense topic in its own right. Recent studies [12, 13, 14, 15] showed that string theory contains the necessary mathematical complexity to reproduce the strongly renormalized Fermi liquid and strange metal phases in connection with a metal-insulator transition, and is additional motivation to further study these phases from the condensed matter theory side. A related, bad metal phase and the crossover region associated with the Mott metal-insulator transition are at the focus of the work presented in this thesis.

The Mott metal-insulator transition is one of the hallmark examples of strong electronic correlation, and is well understood - the electrons in a solid tend to delocalize, but avoid to be found together on the same lattice site. If the excess Coulomb energy paid when two electrons occupy the same orbital overcomes the gain from

uncorrelated delocalization, the electrons become particle-like, acting as localized magnetic moments, and conduction is severely suppressed. However, the (paramagnetic) Mott insulator ground state is not known, neither are its properties clear from the experimental side of view. Unlike the superconducting condensate, electrons in a Mott insulator do not form bound pairs, and the structure of their many-body wave function is certainly more complex. Furthermore, in the vicinity of the Mott transition, there are many ordering instabilities, often towards medium and even high-T_c superconductivity. The connection of the Mott localization and superconductivity in these systems is still not satisfactorily resolved [2]. Most importantly, the Mott transition is by all means a quantum phase transition, but is strangely not observed as a quantum critical point. It is a first order phase transition, and its finite-temperature critical end-point is of the classical Ising type. *This thesis is an effort to reconcile these seemingly converse properties of the Mott transition.*

The results presented here suggest that the first order transition and the second order quantum critical point are just two limits of the same phenomenology, and that the finite temperature critical end-point can be tuned to zero temperature, thus reducing the entire phase coexistence region to a single QCP. Moreover, the DC resistivity is found to fit to a quantum critical scaling law in a large portion of the phase diagram, both in experiment and exact theory. At high enough temperatures, the signatures of the Mott transition are that of a $T = 0$ QCP. Most importantly, the validity of a QC scaling function is shown to be in direct connection with the T-linear resistivity at high temperatures, in agreement with experiments on cuprate films, shedding new light on the 20 years old mystery of bad metal behavior beyond the Mott-Ioffe-Regel limit.

However, a naive description of the first order Mott transition from perspective of quantum criticality runs into a problem immediately - the critical value of the parameter driving a first order transition is a function of temperature. One therefore needs to introduce a generalization of the QC scaling formula which in the original form takes only a single critical value (a number rather than a function of temperature) in its argument. One of the most important results of this work is that such generalization is possible, well defined in terms of purely thermodynamic quantities, and with solid physical justification. The extension of the "critical value" to the super-critical temperatures where no actual transition takes place is the point of maximal instability of the system. The quantum critical region therefore can be viewed in more general terms as the region on the phase diagram where the system

is least decisive of its behavior. The concept of instability lines (or quantum Widom lines) is very general and may prove useful in unrelated problems. From the technical point of view, we introduce a novel approach in numerical simulation - one may not obtain information from only the final result, but also from the intermediate results of a simulation. The dynamical mean field (DMFT) calculation employed in this work is a solution of a self-consistent equation through an iterative procedure. It turns out that it is possible to rigorously relate the stability of a state with the convergence rate of the DMFT calculation which yields the given state. In other words, one should not only look at the solution of an equation, but also at the way the solution is approached in the numerical treatment.

The rest of the thesis is organized as follows. In chapter two I discuss the emergence of quantum critical scaling at high temperatures, in the vicinity of a QCP. Then, I overview the most important aspects of the Mott transition. In chapter three I discuss theoretical methods used - the dynamical mean field theory and its properties, the numerical algorithms used for the solution of the impurity problem (or impurity solvers), and finally the analytical continuation of the imaginary axis data to the real axis. In chapter four I present the results of DMFT, map out the phase diagram of the Hubbard model, and analyze the high-temperature data in view of possible quantum critical behavior. In chapter five I make a few concluding remarks, state the remaining open questions and propose directions for future studies.

2.   Quantum phase transitions

Quantum phase transitions (QPT's) are second-order (continuous) phase transitions that occur at zero temperature when an infinitesimal variation of a Hamiltonian parameter significantly changes the properties of the ground state through level crossing (Fig. 2.1) [4]. The term "quantum" here makes a distinction from conventional second-order phase transitions which occur at finite temperature. In some cases, the classical transition corresponds to the thermal destruction of long-range order, while in others there is a first-order transition between two phases ending in a finite-temperature second-order critical end-point.

A complete theory of quantum phase transitions would have to tackle strong correlations present in interacting many-body systems, which is an impossible task in most cases. Fortunately, there is an analogy between quantum and classical systems which can be utilized to give some very general answers regarding the QPT phenomenology [16, 5]. The physics of classical phase transitions has been studied extensively over several decades, and a very complete theory of universal behavior and critical scaling has been put forward to numerous experimental verifications. It turns out that the concepts of universality classes and order parameters as developed in the study of classical models, can be successfully applied to the case of QPT's. Just as is the case in classical systems, the properties of condensed matter in the vicinity of a $(T = 0)$ quantum critical point (QCP) are insensitive to microscopic details that produce the phase transition in the first place, and are therefore universal.

2.1   Quantum-classical correspondence

The analogy between the classical and quantum systems is most easily seen upon inspection of the partition function in the quantum case

$$Z = \operatorname{Tr} \exp\left(-\beta \hat{H}\right) \tag{2.1}$$
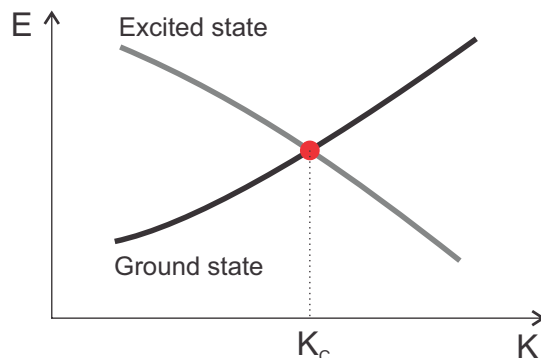
Figure 2.1: Level crossing causes $T = 0$ (quantum) phase transitions. Upon variation of a Hamiltonian parameter K through a critical value K_c, an excited state becomes the ground state of the system.

The statistical operator is formally equivalent to the operator of quantum evolution e^{itH}, but in imaginary time $\beta \rightarrow \tau = it$. This can be used to formulate the quantum problem in terms of path-integrals which sum all possible trajectories that start (at $\tau = 0$) and end (at $\tau = \beta$) in the same state. Then, the statistical operator formally plays the role of the Boltzmann weight of a given trajectory, which can now be considered a classical configuration of a $d + 1$-dimensional system. Therefore, there is a correspondence between d-dimensional quantum and $d + 1$-dimensional classical systems, where the additional dimension is the imaginary time. The transition driving parameter of the quantum Hamiltonian then enters the classical system as (artificial) temperature, and the real temperature of the quantum system only determines the compactification of the imaginary time coordinate ($\tau \in (0, \beta)$, where $\beta = 1/T$) in the classical system, thus making it finite in one direction (unless, of course, $T = 0$). Note also that the classical system is periodic in the τ direction, i.e. a quantum system with a $1D$ chain geometry corresponds to a classical system on a cylinder of circumference β.

A very famous example of the quantum-classical mapping is the case of Josephson junction arrays [17]. This 1D quantum model can be mapped to a classical 2D XY model, which has a well known behavior [18, 19] (note that this mapping is not exact but it rather preserves the universality class of the problem - all the critical exponents are known *exactly*, but far from the transition the solution of the classical model does not yield exact answers regarding the quantum model). The quantum quantity corresponding to the orientation of a classical XY rotor at the lattice site i is the phase θ_i of the complex field ψ_i describing the superconducting order parameter on a

given grain. The temperature of the classical system corresponds to the ratio of the two parameters from the quantum Hamiltonian, namely $T \sim \sqrt{E_C/E_J}$ where E_C is the capacitative charging energy, and E_J is the Josephson coupling energy. In the classical system, at low temperature, there are long-range correlations between the rotors, and they are globally aligned. At a certain temperature T_c, a phase transition occurs to a disordered phase in which correlations between the rotors are only short-ranged. In the quantum system, the voltage between the superconducting grains is conjugate to the phase $\hat{V}_i \sim \frac{\partial}{\partial \theta_i}$. Then, when the Josephson coupling constant E_J is sufficiently reduced, the temperature of the classical system goes through the critical value T_c, the XY rotors become uncorrelated ($\left\langle \frac{\partial}{\partial \theta_i} \right\rangle$ is no longer zero) and the quantum system goes from a superconducting to an insulating state where now there is finite voltage between the grains - although the individual grains are still superconducting, they are collectively incoherent and therefore insulating. Once the correspondence between quantities in the two models has been established, the conclusions regarding the classical model can be immediately applied to the quantum model.

However, the properties of even the classical systems are not known in general. Still, in the vicinity of a critical point, the physics does not depend on the microscopic details of the system, but rather on the universality class, which can be determined through considerations not necessarily including the full solution of the problem. Often, the universality class depends on dimensionality and only the basic properties of the model. Now, if universality class of a classical system is known, the behavior of the corresponding quantum system in the $T = 0$ vicinity of a QCP is also known.

Remarkably, even when quantum classical-mapping is impossible (which is generally the case with fermionic systems such as the gapless Fermi liquid), or the correspondent classical model is of an unknown universality class and impossible to solve, there are general conclusions regarding the QCP phenomenology to be drawn from the classical scaling theory, which seem to apply always.

2.2 Quantum critical (or finite size) scaling

The universality in behavior of both classical and quantum systems stems from the scale invariance of most critical points. The classical scaling theory predicts for an infinite system that precisely at the critical temperature, correlation length ξ will

diverge as

$$\xi \sim |T - T_c|^{-\nu}$$

where the exponent $\nu > 0$ is determined by the universality class of the system [4, 16]. Using the quantum-classical correspondence, the same can be said for a quantum system at $T = 0$

$$\xi \sim |K - K_c|^{-\nu}$$

where K is the parameter of the quantum Hamiltonian which corresponds to the temperature of the classical model. Note also that the correlation length diverges in all directions, including the imaginary time, although not necessarily with the same exponent

$$\xi_\tau \sim \xi^z.$$

In general, τ does not enter the classical model on the same footing as the other spatial dimensions, and here we reserve ξ_τ for the correlation length in the imaginary time direction. However, in many cases of interest, the dynamic exponent z does indeed equal 1 (a notable exception is the Hertz-Millis field theory of magnetic Fermi liquid instabilities, where $z = 2$ or 3, and the effective dimensionality is $d_{eff} = d + z$) [5]. Note also that determining the critical exponents from a mean field theory is usually good enough. However, in the nearest vicinity of the critical point (the so called Ginzburg region) critical exponents acquire corrections which can not be obtained from mean-field considerations.

Then, in the vicinity of the QCP, for an arbitrary observable measured at wave-length k and frequency ω, the scaling theory predicts no explicit dependence on the K parameter

$$\mathcal{O}(k, \omega, K) \sim \mathcal{O}(k\xi, \omega\xi_\tau)$$

since the only characteristic scales are ξ and ξ_τ. When $K = K_c$, $\xi, \xi_\tau \to \infty$, and no scale other than the measured wave-length k and frequency ω can determine observables

$$\mathcal{O}(k, \omega, K_c) = k^{d_\mathcal{O}} \mathcal{O}(k^z/\omega).$$

where d_O is the scaling dimension of the given observable. The physical meaning of this is that precisely at the quantum critical point, quantum fluctuations are present at all time and length scales.

At finite temperatures, however, additional considerations must be made. First,
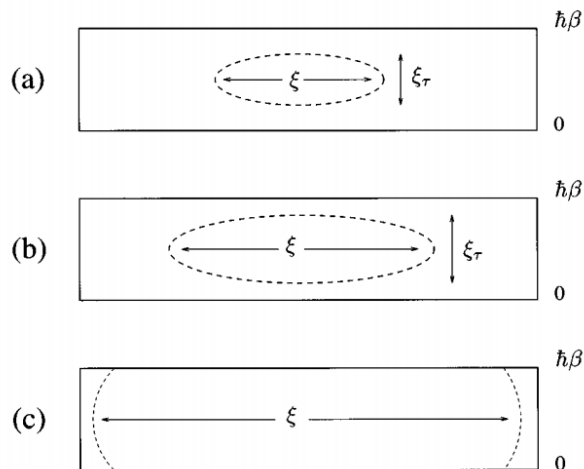
Figure 2.2: At the critical point correlation length diverges [16]. At finite temperature of the quantum system, the size of the corresponding classical system in the imaginary time direction becomes finite ($L_\tau = \beta$). Close enough to the critical point, the correlation lentgh ξ_τ outgrows the size L_τ thus making the system effectively d-dimensional, and therefore classical.

the finite temperature of the quantum system makes the classical system finite in the τ direction. Since at the critical point the correlation length diverges, close enough to the critical point, the classical system will become effectively d-dimensional (Fig. 2.2). In general, this will change the universality class of the classical system, and in some cases, the new universality class does not feature a phase transition at all. Otherwise, there will be a transition, but in the vicinity of it, the behavior of the quantum system will be purely classical, as the extra imaginary time dimension does not play a role here. So, the phenomena accompanying QPT's at $T > 0$ can be divided in two groups (although not without exceptions). Finite temperature can either destroy the phase transition altogether Fig. 2.3b, or the ordered phase can survive up to a certain temperature $T^*(K)$, at which a conventional second order phase transition takes place (red line in Fig. 2.3a; if there is no order on either side of transition, then Fig. 2.3c). The orange area around $T^*(K)$ can readily be described by the classical scaling theory because at the longest length scales, the corresponding classical system is always effectively d-dimensional, and therefore identical to the quantum system. However, this phase transition is of different universality class compared to the $T = 0$ QCP.

In all cases (Fig. 2.3), however, there is an intermediate, crossover regime that
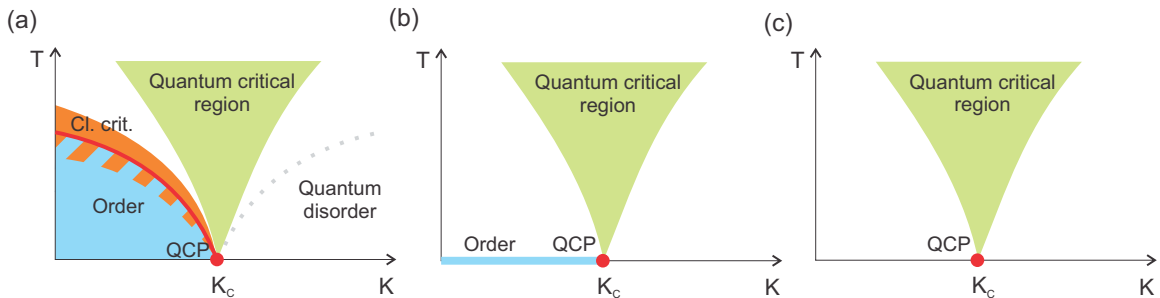
Figure 2.3: Quantum phase transitions can be extended to finite temperatures in two ways. (a) The long-range order persists to some finite temperature and is eventually destroyed by thermal fluctuations through a classical second order transition. In the orange region, classical scaling theory can be readily applied. (b) Even infinitesimal temperature destroys the phase transition, and only a crossover is observed at finite temperature. This type of phenomenology is usually observed when Mermin-Wagner theorem applies - in $d \leq 2$ there can be no spontaneous breaking of a continuous symmetry at finite temperature, and therefore the ordered phase is restricted to $T = 0$. If the transition is not between an ordered and disordered phase, then the generic phase diagram is given by (c). In all cases, an intermediate, quantum critical region is present (green). In this regime, scaling specific to QPT's is observed.

displays scaling behavior of different origin. Although strictly speaking the phase transition of the $d + 1$ universality class is necessarily absent at finite temperatures of the quantum system, it does not disappear completely, but rather gets rounded due to finite-size effects in the classical model. Around K_c, but at some finite temperature, the only characteristic scale in the system is no longer the correlation length, but there is also L_τ. So the properties are determined by the ratio between the correlation length and the size of the system in the imaginary time direction ξ_τ / L_τ, where $L_\tau = \beta$. However, even at $K = K_c$, the temperature makes a difference so for a general observable

$$\mathcal{O}(k, \omega, K, T) = \mathcal{O}_c(T) \, \mathcal{O}(k L_\tau^{1/z}, \omega L_\tau, L_\tau / \xi_\tau)$$

must hold. If the observable is measured at zero frequency and infinite wave-length, we have

$$\mathcal{O}(k = 0, \omega = 0, K, T) \equiv \mathcal{O}(K, T) = \mathcal{O}_c(T) \, \mathcal{O}(L_\tau / \xi_\tau) = \mathcal{O}_c(T) \, \mathcal{O}(|K - K_c|^{z\nu} / T).$$

$$(2.2)$$

This behavior is known as the quantum critical scaling (or finite size scaling in

classical systems) and is experimentally observed in many systems [6, 7, 8, 9, 10]. It is very important to note that the physical content of the above expression is not actually present at $T = 0$. The width of the quantum critical region (QCR) in which the above is expected to hold shrinks to a single point at $T = 0$, so all the features of the QCR stem directly from the QCP. In practice, the true discontinuity (jump) in the value of quantities possibly present at the QCP becomes a smooth crossover at finite temperature, ever smoother with increasing temperature, yet in a way precisely determined by the universality class of the $T = 0$ transition itself. The quantum critical scaling is a "magnifying glass" looking at the QCP which allows for the experimental inspection of the properties of a zero-temperature phase transition otherwise not accessible. Note also that simplest considerations yield the "hyperscaling" relation

$$\mathcal{O}_c(T) = \mathcal{O}_o T^{-d_\mathcal{O}/z} \tag{2.3}$$

but significant corrections to this law may be present, depending on the model. Otherwise, the sign of the scaling dimension determines whether the observable will go to infinity or zero at the QCP. When scaling dimension is zero, $\mathcal{O}_c(T)$ is just a constant. For example, for the resistivity in the context of non-interacting disorder driven (Anderson) metal-insulator transition, $d_\rho = d - 2$, which is also known as the Wegner scaling. Here, the scaling dimension depends on the dimensionality of the system. However, above the upper critical dimension for a transition, these simple considerations fail due to "dangerously irrelevant variables" (above the upper critical dimension for a transition, the Gaussian field theory becomes exact, but one must not immediately discard the quartic interaction term; more careful considerations must be made in determining the critical exponents, and because of this, no general result such as the hyperscaling can be obtained).

In the following, I present the hallmark examples of how quantum critical scaling of quantities can demystify the existence and properties of a QCP.

2.2.1 QHE

The quantum Hall effect is the appearance of plateaus in the Hall resistivity, precisely at multiples of the quantum of resistivity h/e^2 (when multiples are integer, then it is known as the integer QHE, otherwise - the fractional QHE). A thin sheet of a material is put in a perpendicular magnetic field, and connected to four terminals. A current is induced along one axis, and voltage is measured along the other to
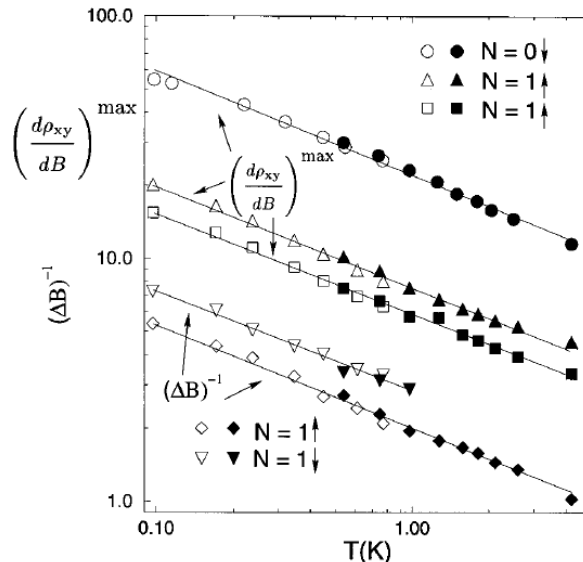
Figure 2.4: Crossover between two plateaus in quantum Hall effect displays QC scaling [10]. The maximal derivative of resistivity with respect to magnetic field is a power law of temperature, consistent with the QC scenario. The width of the crossover region ΔB increases with temperature, in the same fashion.

deduce the Hall resistivity ρ_{xy}. As magnetic field is varied, different Landau levels of cyclotron motion cross the Fermi level, which is observed as jumps in otherwise constant Hall resistivity. The behavior of resistivity in the crossover between two plateaus can be used to determine the properties of the zero-temperature transition. At the critical value of the magnetic field, resistivity is independent of temperature. Also, the jump in resistivity becomes smoother with increasing temperature, but in a fashion such that $\frac{\partial \rho}{\partial B} = T^{-z\nu}$ *precisely* (Fig. 2.4) [10, 16]. Furthermore, it turns out that the scaling exponent $z\nu$ is universal for all materials exhibiting QHE. This means that the phase diagrams of such systems feature an array of QCP's, as presented in Fig. 2.5, and that they all fall into the same universality class. The theory of QHE has been very successful in describing the position of plateaus which also displays some universality, but it is remarkable how the scaling theory captures the essential features of the crossover region without any regard to the actual Hamiltonian of these systems.
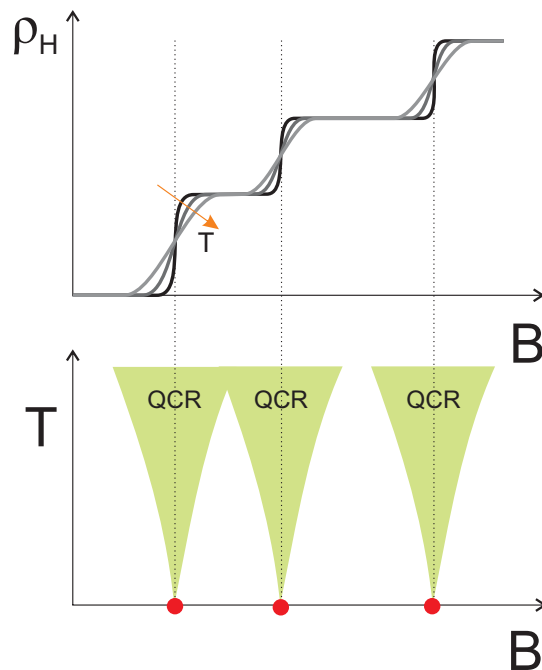
Figure 2.5: Phase diagram of the quantum Hall systems features an array of quantum critical points. At $T = 0$, Hall resistivity ρ_H has discountinuities (or "jumps") at certain values of external magnetic field. With increasing temperature, the jumps become more and more gradual. Each QCP is associated with a quantum critical region (green) where resistivity displays a behavior consistent with a quantum critical scaling law.

2.2.2   SIT in α-MoGe thin films

The α-MoGe thin films become superconducting at low temperature, but due to high level of disorder in such samples, true zero resistivity is not observed [20, 9]. Rather, the system displays inverse activation, or the exponential growth of resistivity with temperature. This behavior is due to dissipative motion of vortices, which get depinned from structural defects by the applied current (the zero resistivity is expected only at $T = 0$ when the vortices freeze in a glass-like state). As usual, magnetic field can also destroy superconductivity in these systems, in which case the electrons become weakly localized (the resistivity is a logarithmic function of temperature at high magnetic fields). It has been shown that these systems also display quantum critical scaling in the crossover region at high temperature. On Fig. 2.6, it is shown how all the resistivity data can be collapsed onto two branches, which is a standard procedure in determining whether QC scaling is observed, in
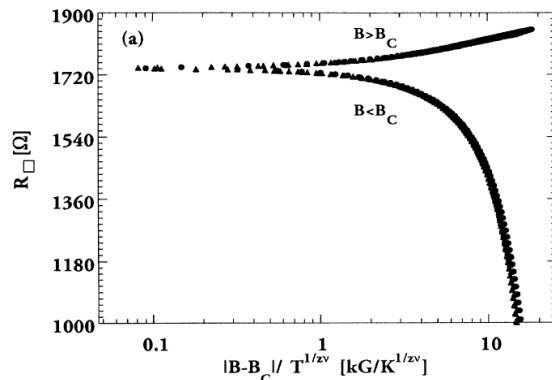
Figure 2.6: Superconductor-insulator transition in thin α-MoGe films displays characteristic quantum critical scaling of resistivity [9].

direct connection with Eq. 2.2 (more details below).

2.2.3 MIT in 2D electron gas

At the interface of two semiconductors with different gaps, it is possible to realize a truly two-dimensional free electron gas [11]. The electrons here have to overcome a gap of ~ 200K to delocalize in the z-direction, so when the experiment is performed at 2K, they become confined within barely 100Å along the z-axis. It has been long believed that such systems would always be insulating, because it was expected that in 2D, even infinitesimal disorder completely localizes the electrons. However, recent developments have shown that such systems actually exhibit a plethora of interesting phenomena. On Fig. 2.7 we show a conceptual phase diagram of the 2D electron gas realized in MOSFET systems, where the carrier concentration is controlled by (electric) field effect, and the external magnetic field is applied perpendicularly to the plane of electronic motion. We see that even at $B = 0$, there is a metal-insulator transition (MIT) at some critical value of carrier concentration, and at high fields, also fractional quantum Hall effect (FQHE) is observed. The experiments are always performed at finite temperature, and both the MIT and the transition between the Hall plateaus are observed as continuous crossovers, but the scaling of resistivity at higher temperatures indicates that they correspond to true QPT's at $T = 0$. Here we show the results of resistivity measurements in the vicinity of the $B = 0$ MIT in Si-MOSFET's.

In upper left panel of Fig. 2.8 we show zero-bias resistivity as a function of

14
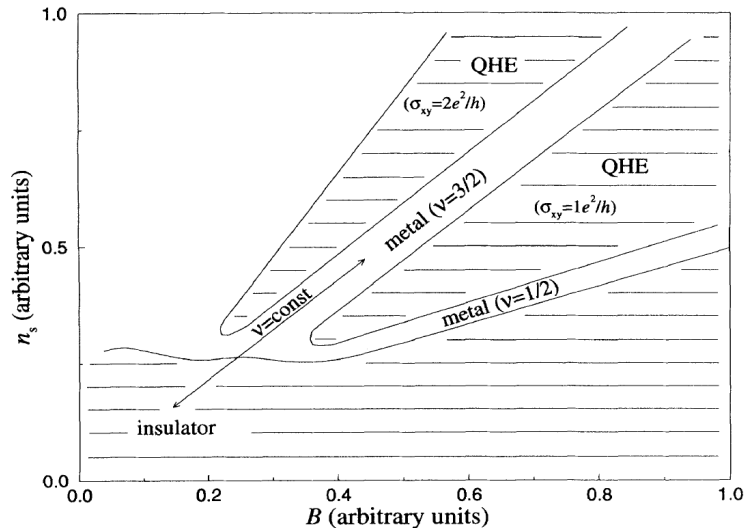
Figure 2.7: The conceptual phase diagram of 2D electron gas in MOSFET systems [11]. At zero magnetic field there is a metal-insulator transition at $T = 0$. At high fields, also quantum Hall effect is present.

electron concentration n, at different temperatures. The feature strikingly similar to the case of α-MoGe and QHE systems is that all the curves cross in a single point, i.e. at a certain value of $n = n_s$, resistivity is basically independent of temperature. Furthermore, from the upper right Fig 2.8 it can be seen that when $n > n_s$, the resistivity monotonically decreases with decreasing temperature, and when $n < n_s$, it is the other way around. This behavior is immediately reminiscent of metallic and insulating phases being separated by a single quantum critical point at $T = 0$. However, if this is true, then it is expected that resistivity displays a characteristic quantum critical form at high temperatures when $n \approx n_s$

$$\rho(n, T) = f(T/(n - n_s)^{z\nu})$$

To check this, one can rescale the temperature for each $\rho(T)|_n$ curve by hand to try and make them all collapse on two branches. This analysis is presented on the lower left panel of Fig. 2.8. To be consistent with the quantum critical scenario, the scaling parameter $T_0(n)$ should be a power law of $(n - n_s)$, and as we see in the lower right panel of Fig. 2.8, $T_0(n)$ fits perfectly to $(n - n_s)^{1.6}$. However, this does not automatically yield an estimate of the scaling parameter ν, but only of the product of ν and the dynamical exponent z. To get an estimate of the two exponents separately,

15
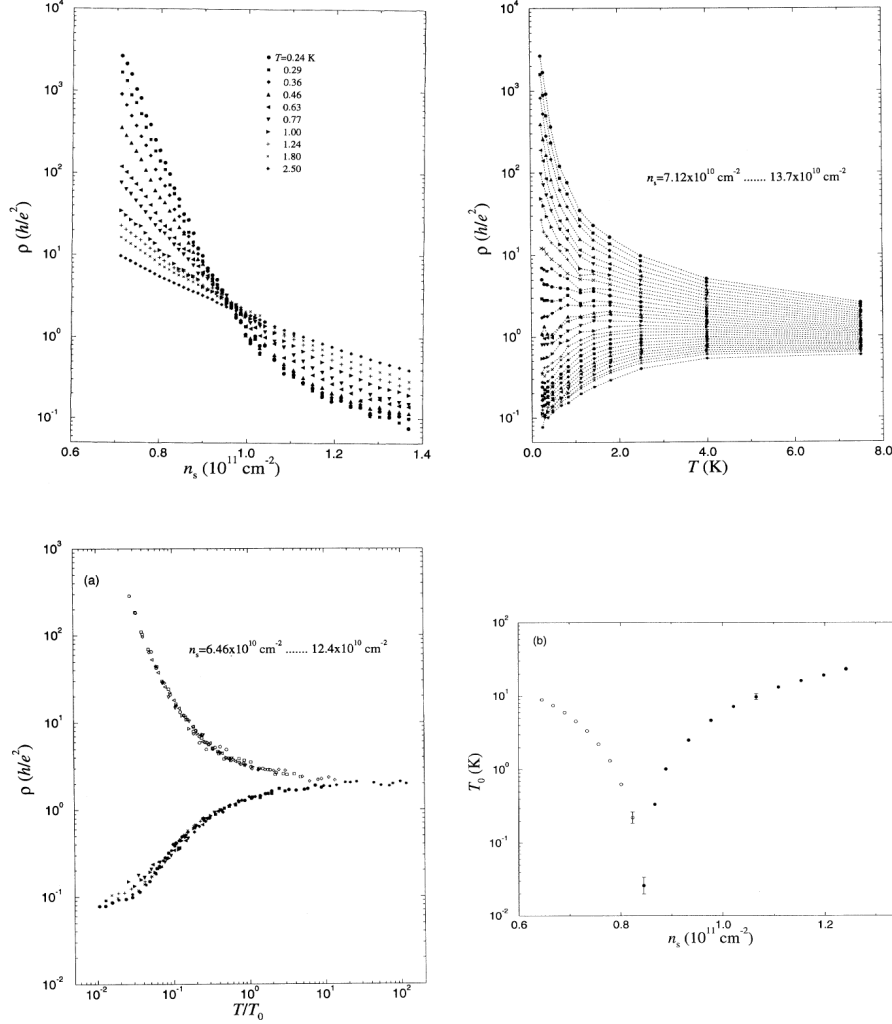
Figure 2.8: Quantum critical scaling in MOSFET systems [11]. Upper left panel: resistivity as a function of electron concentration. All curves cross in a single point. At this (critical) concentration n_c, no temperature dependence of resistivity is observed. Upper right panel: resistivity as a function of temperature. At concentrations lower than the critical value, resistivity drops exponentially with temperature, which is typical insulating behavior. Above critical concentrations, it is the other way around, and metallic behavior is observed. Lower left panel: all resistivity curves can be collapsed by rescaling the temperature with appropriately chosen parameter T_0. Lower right panel: T_0 fits well to a power law function of $\delta_n = n - n_c$, which is typical for quantum critical scaling.

one can perform a study of non-linear response, where resistivity is measured as a function of applied electric field, i.e. look at the I/V characteristic of the system

16
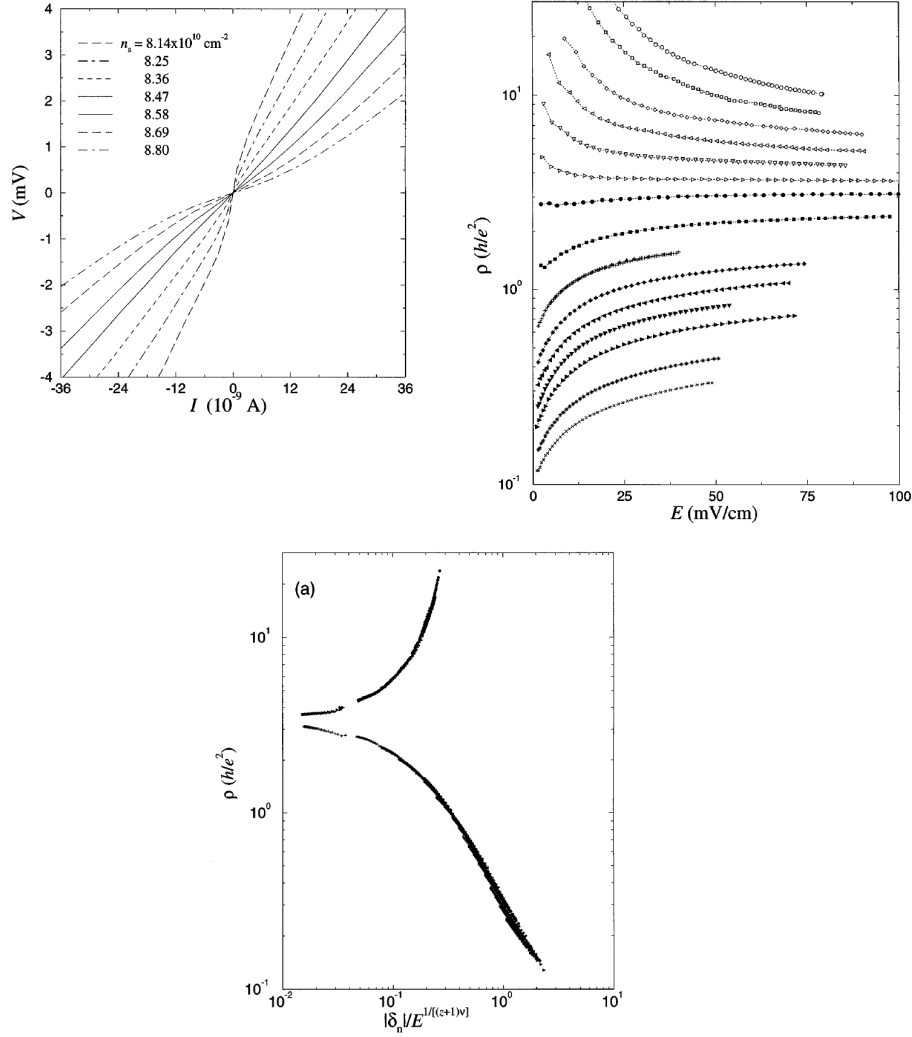
Figure 2.9: I-V characteristic of MOSFET systems also exhibits quantum critical scaling [11]. This can be used to deduce the critical exponents z and ν separately.

[21]. In this case, scaling theory predicts the following form of resistivity

$$\rho(n, E) = f_2(E/(n - n_s)^{(z+1)\nu})$$

The scaling exponents $z\nu$ and $(z + 1)\nu$ define two equations with two unknowns, which can be trivially solved. Upon analysis similar to Fig. 2.8, as presented in Fig. 2.9, one obtains that $z \approx 1$ and $\nu = 1.6$. This can be interpreted as strong evidence of the existence of a scale-invariant QCP in the 2D electron gas in Si-MOSFET's at zero magnetic field. However, the exact mechanism behind this tran-

sition remains elusive, although there are mounting evidence that Coulomb repulsion plays a crucial role in these systems. This is, however, easily understood as in such dilute electron gases ($n \approx 8 \times 10^{11} cm^{-2}$), average Coulomb energy dominates over the Fermi energy by two orders of magnitude.

Note also, that although the scaling function f is in general not known, in 2D electron gas, however, f turns out to be an exponential function

$$f\left(\frac{\delta n}{T^{\frac{1}{z\nu}}}\right) = \exp\frac{\delta n}{T^{\frac{1}{z\nu}}} \tag{2.4}$$

where $\delta n = n - n_s$. The above form can be obtained immediately by assuming that the β-function ($\beta = d\ln g/d\ln L$, where g is conductivity and L is the effective size of the system, in this context $L \sim T^{-1/z}$) is a function of only g [22]. However, for this to be true in the range of g as large as is observed in experiment (over 2 orders of magnitude), β-function needs to have a very special form. This automatically implies a very important property of the transition. Precisely at the transition, there is a mirror symmetry between the two phases, and this is observed at high temperatures as

$$f(x) = 1/f(-x) \tag{2.5}$$

When two branches of the resistivity data are plotted on the log-scale, they should appear symmetric [23]. This is precisely what is observed in experiments on the MOSFET's, but as we shall see, some recent experiments suggest that mirror symmetry may be a universal feature of metal-insulator transitions, and that it is not restricted to this particular case.

2.3 Mott metal-insulator transition

One of the most blatant effects of strong electronic correlation is the Mott metal-insulator transition [24, 25, 26]. It occurs upon an infinitesimal change of a control parameter, usually pressure or doping (through capacitor effect or chemical substitution), and is observed as a sudden change in resistivity which may cover even several orders of magnitude. Usually, Mott systems are insulating at atmospheric pressure, but become metallic if pressurized. Contrary to the case of conventional band-insulators and semiconductors which may be described in terms of effectively single-particle physics, such approach to Mott systems fails - the electronic struc-

ture calculations such as density functional theory (DFT) unanimously predict for these materials to always be metallic, with a well defined Fermi surface deep within the conduction band. There are also cases when a material exhibits pronounced "Mottness" - it is metallic but with heavily renormalized electron mass. For these systems as well, DFT yields false predictions regarding bandwidth and unit cell size.

The main clue as to what is the physical mechanism behind the Mott transition and the failure of both the Hartree-Fock (RPA) theory and DFT lies in the atomic structure. The common feature of many Mott systems are the semi-occupied valence orbitals of d or f type. Materials which fall in this group are based in 3d and 4d transition metal elements, 4f rare earth elements, 5f actinides, and their oxides. What makes d and f orbitals different from the s and p type is that they are well localized. When two electrons occupy the same localized orbital, they interact strongly, and this will cause true many-body correlation which may no longer be neglected. Even more so, the electronic correlation turns out to be the sole driving force of the Mott transition - the details of the atomic structure and possible lattice-structural effects do not play an important role. It proves sufficient to consider simple toy models and observe the Mott mechanism, but the solution of the problem must be fully quantum mechanical. The Dynamical mean field theory (DMFT) of the Hubbard model in infinite dimensions is one such solution, and it had great success in elucidating the physics of Mott transition. DMFT is the main method employed in this thesis and is discussed in detail in chapter 3.

As for the intuitive understanding of the Mott transition, it was discussed by Sir Neville Mott long before the first solution of DMFT [27]. Generally speaking, in solid state systems there is a competition between two energy scales. One is the kinetic energy and the other is the repulsive Coulomb interaction energy. The Coulomb interaction is usually well screened and in those cases the Fermi liquid theory is a good starting point for the theoretical description. The low energy excitations are then long lived wave-like states with renormalized mass. However, the high-energy excitations always experience less screened interactions. When atomic orbitals are localized, and there is little overlap between valence orbitals on adjacent sites, the energy bands are narrow, and the kinetic energy becomes comparable to the Coulomb repulsion. In those cases, the mass of the low energy states can become highly renormalized, and the high-energy states become particle-like. The higher the rate of the Coulomb to kinetic energy, the more electrons localize, and at ever lower energies. When localization reaches the Fermi level, the system becomes a

Mott insulator. Then, in experiment, when pressure is increased, the lattice spacing becomes smaller, the overlap between adjacent orbitals increases thus boosting the kinetic energy, and the system can become metallic again. As already pointed out, the lattice degrees of freedom do not play a significant role in the Mott transition, but the state of the electron gas does affect the lattice. The Mott transition is usually accompanied with (sometimes even significant) change in the specific volume. The delocalized electrons tend to be more involved in the cohesive energy of the lattice, and Mott systems in the metallic state have usually a smaller unit cell.

However, the Mott transition is not a generic quantum phase transition. It was immediately clear from experiments that it is a first order-transition, not much unlike the liquid-gas transition observed in water or noble gases [28, 29, 30, 31, 32, 33]. The Mott transition usually displays hysteresis up to some critical temperature T_c above which the abrupt change in resistivity is no longer observed, but rather a smooth crossover. On the other hand, two distinct phases often seem to persist all the way down to zero temperature, which definitely puts this transition in a wider group of quantum phase transitions. Furthermore, there is a clear connection of the Mott transition and antiferromagnetic order as most Mott insulators are antiferromagnetic at low temperature. This is easy to understand in terms of excess entropy. A paramagnetic Mott insulator has a very large entropy because the ground state can be realized in exponentially many ways. The excess entropy must be quenched somehow as $T = 0$ is approached. The huge degeneracy of the ground state is most easily lifted by antiferromagnetic ordering. Otherwise, dimerization can also occur - this way there is no long range order, but pairs of electrons on adjacent lattice sites form correlated bound states. In the presence of frustration of antiferromagnetism, a spin liquid phase with separation of charge and spin degrees of freedom is also a possibility at low temperature. Whether a paramagnetic Mott insulator can truly exist all the way down to zero temperature is actually an open question.

However, the most common scenario is the one of anti-ferromagnetic ordering. But the ordering tendency can be strong enough to disrupt even the metallic phase at low temperature. Even when the Coulomb interaction is not strong enough to drive the system into a Mott insulating state, there is still a competition between the suppression of double occupancy and virtual hopping processes which yields an effective antiferromagnetic (AF) interaction between electrons on adjacent sites. If AF interaction is strong enough to order otherwise delocalized electrons, the true Mott transition is observed only at temperatures higher than the Neel temperature

20
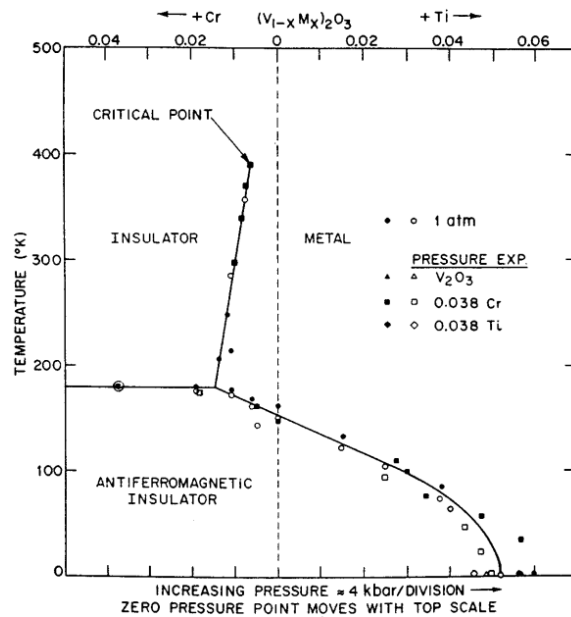
Figure 2.10: Phase diagram of the bulk 3D material V_2O_3. Depending on the level of doping or pressure, system can be either metallic or insulating. At lowest temperatures, an antiferromagnetic state is observed. [29]
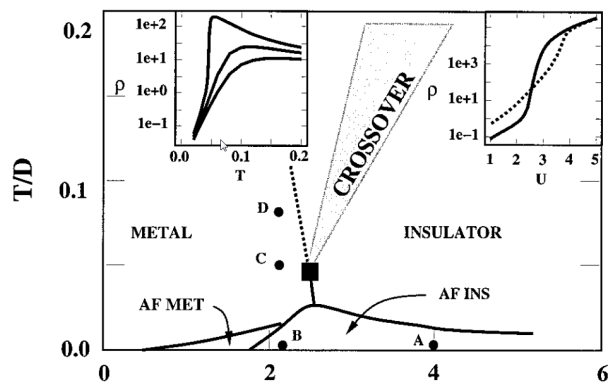
Figure 2.11: Dynamical mean-field theory qualitatively reproduces the main features of the phase diagram of V_2O_3. As frustration of antiferromagnetic correlation is increased, the Néel temperature for the AF order drops, revealing a first order Mott transition line. [34]

of the anti-ferromagnetic order. This is the case in a very famous example of Mott transition, which is the 3D bulk material vanadium-III-oxide V_2O_3. The phase diagram of this material is shown in Fig. 2.10. The antiferromagnetic insulator, however, is not exotic. It's properties are reproduced by the solution of an AF Heisenberg model. In DMFT, if breaking of spin symmetry is allowed, the phase

diagram also features only an antiferromagnetic insulator dome [34]. But as one gradually turns on frustration in the model (by including, for example, next nearest neighbor hoppings) the Néel temperature drops, and a first order Mott transition emerges above the reduced AF dome (Fig. 2.11). In this regime, no other theory can capture the properties of the DMFT solution.
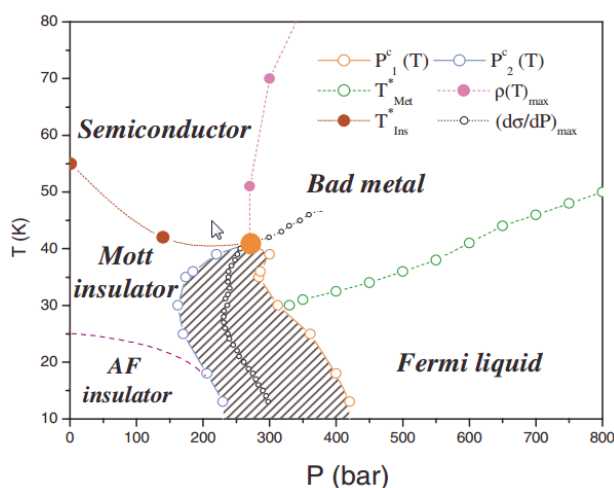
Figure 2.12: The phase diagram of κ-(BEDT-TTF)$_2$Cu[N(CN)$_2$]Cl. A first order Mott transition with a coexistence region is present. The insulating state becomes anti-ferromagnetic at low temperature [30].
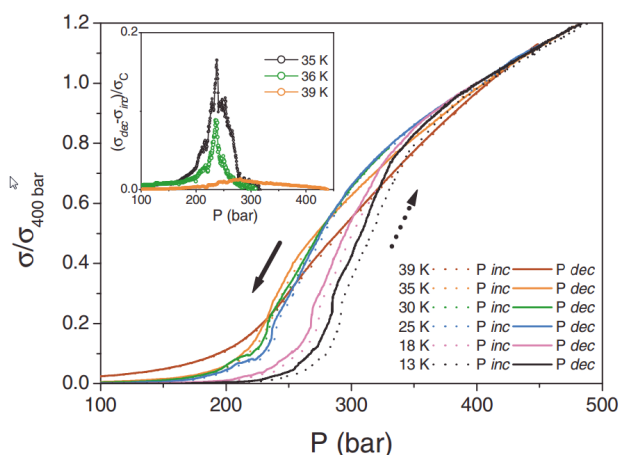
Figure 2.13: The resistivity exhibits hysteresis - in the coexistence region two different states are stable [30].

Another large class of materials, the κ-organics, pose a good example of a pure Mott transition. The lattice structure in these materials is very complicated, but
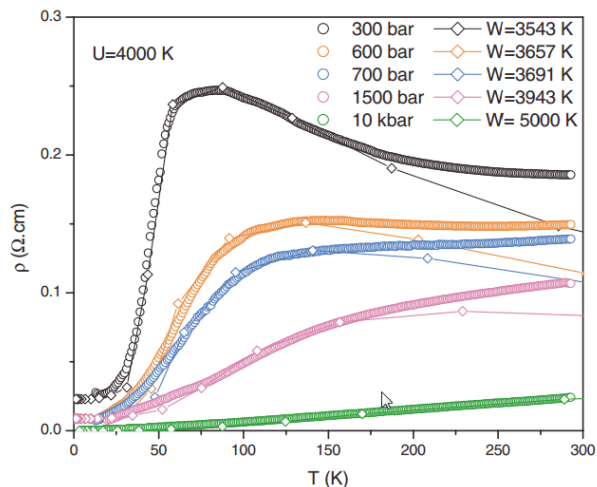
Figure 2.14: The non-monotonic resistivity is a hallmark of strong correlations, and is observed close to the Mott transition, on the metallic side. DMFT result reproduces the position and height of the maxima in resistivity with high accuracy (diamonds - DMFT, circles - experiment) [30].

extensive DFT calculations suggest that it can effectively be described using a half-filled single-band Hubbard model on a triangular lattice [35]. Due to geometrical frustration in these materials, antiferromagnetism is usually suppressed, but in the vicinity of the transition, a high-T_c superconducting dome emerges, which makes the Mott transition even more intriguing. Examples of phase diagrams and transport in κ-organics are shown in Figs. 2.12,2.13,2.14 and 2.15. In cases when the triangular lattice is anisotropic, the antiferromagnetism is not completely suppressed and at low temperatures, the Mott insulator develops the AF order. Otherwise, a gapped spin liquid characterization of the low temperature Mott insulator is possible. However, in all cases, a first order transition and a coexistence region is observed up to some temperature, and in the supercritical region, the system is neither a good metal nor a good insulator, and its resistivity can be tuned continuously through several orders of magnitude. This constitutes the crossover region of the Mott transition, and will be in focus in section 4.1.7.

The most important question addressed in this thesis is whether quantum critical scaling (as introduced in the previous section) can be observed in Mott systems. The phenomenology of the Mott transition makes a significant departure from the standard QCP scenario, because the phase transition is not restricted to zero-temperature, but is rather extended by a first order-transition line to finite
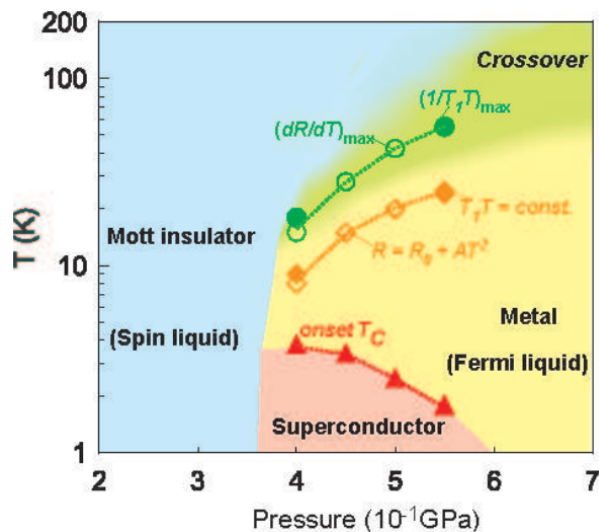
Figure 2.15: Phase diagram of κ-$(ET)_2Cu_2(CN)_3$. Metallic state is superconducting at lowest temperature. AF order is frustrated, and the Mott insulator remains paramagnetic at low temperature [31].

temperatures. Note that this is different from the case in Fig. 2.3a where the ordered phase survives up to $T^*(K)$ - neither the metallic nor the insulating phase break any symmetries and the transition is not of the order-disorder type. However, a classical treatment of the second order critical-end point (CEP) is still possible because it is at finite temperature. The behavior of the system in the vicinity of the CEP is found to correspond to critical phenomena of the classical Ising universality class with $\nu = 1$ [36]. Still, the T_c is generally low and is not expected to be make significant difference at high T, where quantum critical scaling is expected to hold. In this thesis we recognize the possibility of Mott T_c going to zero [37, 38], in which case the Mott transition reduces to a single QCP (Fig. 2.16). In view of this, the first order transition and the pure QCP are considered as two limits of the same phenomenology, and it seems even less likely that the QCR is entirely absent from the phase diagram of materials exhibiting the first-order Mott transition (Fig. 2.17).
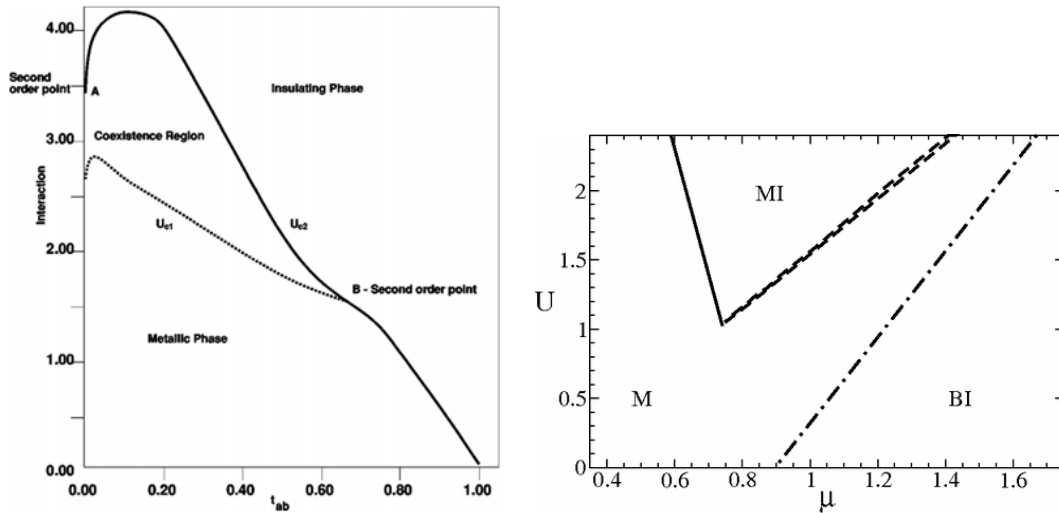
Figure 2.16: At least in theory, the T_c for the first order Mott transition can be brought to zero by varying Hamiltonian parameters [37, 38]. Left: the phase diagram of the double Bethe lattice; the parameter to vary - interlattice hopping. Right: The phase diagram of the Anderson lattice model; abbreviations: MI - Mott insulator, M - metal, BI - band insulator; the Mott transition between the hole-doped metal and the integer filled Mott insulator displays no coexistence, while the transition between the integer filled Mott insulator and the electron doped metal has a T_c becoming smaller as U is decreased.
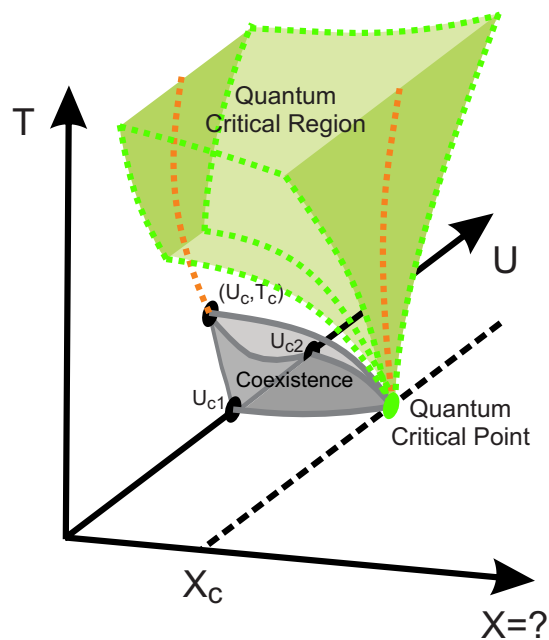
Figure 2.17: The main focus of our work is the possibility of the phenomenology illustrated above.

3. Methods

In this chapter I review the methods used in this thesis. The main method employed is the dynamical mean field theory (DMFT) which is used to solve the Hubbard model. The solution of DMFT reduces to a solution of the Anderson impurity problem, with a self-consistently determined hybridization bath. How the original problem is mapped onto this self-consistent calculation is explained in sections 3.1 and 3.3. In section 3.1 I discuss the properties of the DMFT theory, and layout a very general approach which can be used to derive it. In section 3.3 I use a more straight-forward approach to derive DMFT. There I show how in the limit of infinite dimensionality, an explicit form of the DMFT equation (ready for numerical treatment), can be obtained by performing a hybridization expansion around a single site. The limit of infinite dimensions and its implications for the calculation of optical conductivity (as performed throughout this thesis) is discussed in section 3.2. The numerical solution of the impurity problem by stochastic summation of diagrams and perturbation theory is explained in section 3.4. Finally, in section 3.5 I describe the method used to analytically continue the result of DMFT to the real axis. This is a very important step in numerical solution of DMFT, because its result is in some cases the imaginary time-dependent local Green's function, yet for the calculation of frequency dependent response functions we need the real frequency Green's function.

3.1 Dynamical mean field theory

The dynamical mean field-theory (DMFT) in its simplest form provides a prescription for the solution of the fermionic single-band Hubbard model, although it can be easily generalized for various lattice models. It falls in a wider group of methods which transform an interacting many-body problem into a simpler, representative (or effective) model, which is supplemented with a self-consistency condition [26]. All these methods can be traced back to a very general formalism which relies on the Legendre transformation of the grand potential. The procedure yields a closed

TABLE 2. Comparison of theories based on functionals of a local observable

Theory	MFT	DFT	DMFT
Quantity	Local magnetization m_i	Local density $n(x)$	Local GF $G_{ii}(\omega)$
Equivalent system	Spin in effective field	Electrons in effective potential	Quantum impurity model
Generalised Weiss field	Effective local field	Kohn-Sham potential	Effective hybridisation

Figure 3.1: Legendre transform approach can reproduce various theories. In each case one chooses one quantity of interest, and defines a representative (effective, or equivalent) local model coupled to an external, generalized Weiss field [26].

form self-consistent equation which is in itself exact. However, not all terms in the equation may be known in general, and then for practical purposes some approximations must be made. On the other hand, even if the equation is completely known and solved, the method guarantees only the knowledge of the quantity A which was used in the Legendre transform. Other quantities may be possible to calculate, but note that the physical meaning of the quantities in the representative model may not coincide with that in the original model, and that correspondence between the original and effective models may be unclear.

The Legendre transform formalism can be used to reproduce also the general mean-field theory (for example the Weiss theory of classical Ising model, or WMFT) and more importantly the density functional theory (DFT) (see table). In view of this formalism, the difference between DFT and DMFT is in the choice of the quantity in focus and also the representative model which needs to be solved (Fig. 3.1). In DFT, the quantity in focus is the local single-particle density $\hat{n}(x)$, and the representative model is a single-particle Schrödinger equation in an effective potential $V_{KS}(x)[n]$ which is a functional of the density $n(x)$. Hence the term density functional theory. In DMFT, the quantity in focus is the local propagator $G(\tau)$, and the representative problem is that of a local impurity coupled to an effective bath , which is in turn defined by a functional of the local propagator, the hybridization function $\Delta(\tau)[G]$. The main difference between DFT and DMFT is that in DFT, the representative model is non-interacting, while in DMFT it is a full many-body problem, although with only a few degrees of freedom such that it can be solved by means of numerical simulation. Furthermore, in DFT, the self-consistent equation is never known entirely. The problematic exchange-correlation potential term

can be obtained from an empirical fit to a QMC result of some simple model, but the applicability of such approximation may not be well understood. On the other hand, in DMFT, the self-consistent equation is known *entirely* in one specific case - the limit of infinite lattice dimensionality. As we shall see, the problematic term here is the total kinetic-energy - while the general formula for kinetic energy is of course known, it may not always be possible to express it in terms of only the local propagator. The approximation that needs to be made here is to assume that the self-energy is purely local

$$\Sigma_{\mathbf{k}} \longrightarrow \Sigma \tag{3.1}$$

but this is exact in the limit of infinite dimensions. See section 3.2 for details. DMFT is also exact in the non-interacting and atomic limits, but it is very important that there is at least one non-trivial limit in which DMFT is exact because this ensures that all the quantities will be physical (respecting causality etc.). Anyhow, the locality of self-energy turns out not to be far fetched, and therefore the approximation made when DMFT is used to treat 2D or 3D systems is not crude at all. At high energy, high temperatures, or in the presence of geometrical frustration, DMFT approximation is shown to be basically exact - the result coincides with experiments on cold quantum gases in optical lattices as well as large scale quantum Monte Carlo calculations, and the self-energy is proven to be only weakly dependent on the wave vector $\mathbf{k}$ [39, 40, 41, 42, 26]. Most importantly, solution of the DMFT equation has brought significant insight to the understanding of strong correlation and its hallmark embodiment, namely the Mott transition. DMFT has been successfully used to reproduce experimental phase diagrams and various response functions such as optical conductivity (see section 3.2.1), spin and charge susceptibility and double occupancy [43, 44, 26]. The local self-energy calculated in DMFT can be used to reconstruct the spatially resolved spectral function, and successfully reproduce results of the angle-resolved photo emission spectroscopy experiments [45, 24]. Unlike DFT where the single particle excitation spectrum can not be calculated rigorously even within a given approximation of the self-consistent equation, energy resolution is built-in in DMFT by construction. This proves to be a very important aspect of the theory - electrons at different energies may behave drastically differently, and this *can* be captured by DMFT. Namely, while the low energy electrons (around the Fermi level) are wave-like, the high-to-intermediate-energy electrons may be experiencing strong interactions and localize. This information is contained in self-energy

which, although local, has a very non-trivial energy dependence. There are also extensions of DMFT (cellular DMFT and dynamic cluster approximation) which reintroduce some of the **k** dependence in the self-energy by constructing the effective impurity problem in a way that it is not purely local. Although approximate, these methods have shed light on sector selective Mott transition, which is very important for the understanding of strongly correlated electrons in low dimensions. However, most information can be obtained from the combination of both DFT and DMFT (namely, the DFT+DMFT approach), which is currently the cutting edge tool for modeling complex materials [44].

In the following I overview the Legendre transform approach and then show how it is applied to the Hubbard model.

3.1.1   Legendre transform approach

Let $\hat{H}$ be the lattice Hamiltonian of interest. Then we can split it in two parts, such that one part is solvable, say $\hat{H}_1$

$$\hat{H} = \hat{H}_1 + \hat{H}_2 \tag{3.2}$$

Furthermore, we need to decide what quantity we want to calculate, say $\hat{A}$. Now we define an operator

$$\hat{H}_\alpha[\lambda, a] = \hat{H}_1 + \alpha\hat{H}_2 - \sum_i \lambda_i(\hat{A}_i - a_i) \tag{3.3}$$

The index i counts lattice sites, and $\hat{A}_i$ is a local observable. One can also switch to the continuum limit where the sums are replaced by integrals over space. If the quantity A is time dependent or non-Hermitian, one must switch to path integral formalism, where the above operator has the meaning of an action. The operator $\hat{H}_\alpha[\lambda, a]$ a function of a single real number α, and a functional of real or complex fields $\lambda \equiv \{\lambda_i\}$ and $a \equiv \{a_i\}$. λ_i's have the meaning of local Lagrange multipliers. Now we immediately see that the observables do not depend on a because it enters only as an irrelevant constant through λa. Therefore, the statistical average of the quantity in focus depends only on λ and α

$$\langle A \rangle_\alpha[\lambda] \tag{3.4}$$

We are interested in calculating

$$\langle A \rangle_{\alpha=1}[\lambda = 0] = ? \tag{3.5}$$

which corresponds to the statistical average in the original Hamiltonian. The grand potential (or Free energy) now is given by

$$\Omega_\alpha[\lambda, a] = -\frac{1}{\beta} \ln \text{Tr} \exp\left(-\beta \hat{H}_\alpha[\lambda, a]\right) \tag{3.6}$$

This form of the grand potential is known as the Legendre transform of the original grand potential $\Omega = -\frac{1}{\beta} \ln \text{Tr} \exp(-\beta \hat{H})$. Immediately,

$$\frac{\partial \Omega_\alpha[\lambda, a]}{\partial \lambda_i} = a_i - \langle \hat{A}_i \rangle_\alpha[\lambda] \tag{3.7}$$

Now for a given a, one can always find λ such that $\langle \hat{A}_i \rangle_\alpha[\lambda] = a_i$. Therefore, the solution of

$$\frac{\partial \Omega_\alpha[\lambda, a]}{\partial \lambda_i} = 0 \tag{3.8}$$

with respect to λ yields a Lagrange multiplier configuration implicitly dependent on a and α which we denote $\lambda_\alpha[a]$ and

$$\langle \hat{A}_i \rangle_\alpha[\lambda_\alpha[a]] \overset{def}{=} a_i \tag{3.9}$$

We now introduce a new potential, defined only in the stationary points of Ω

$$\Gamma_\alpha[a] \equiv \Omega_\alpha[\lambda_\alpha[a], a] \tag{3.10}$$

Note that this functional has no explicit dependence on λ. Taking the above definition, we have quite generally

$$\frac{\partial \Gamma_\alpha[a]}{\partial a_i} = -\lambda_{i\alpha}[a] \tag{3.11}$$

so we have

$$\frac{\partial \Gamma_{\alpha=1}[a = \langle A \rangle_{\alpha=1}[\lambda = 0]]}{\partial a_i} = 0 \tag{3.12}$$

which is easy to understand. When we request that the statistical average $\langle A \rangle$ is that of the original Hamiltonian, and α=1, no field λ is actually needed to ensure

this. Also, it is clear that the solution of the original problem can be obtained by minimizing $\Gamma_{\alpha=1}$. This can not be done straightforwardly, but the following considerations provide a very general way to circumvent the main difficulty lying in the H_2 part of the Hamiltonian, and find the minimum of $\Gamma_{\alpha=1}$ by only considering the derivatives of Γ_α with respect to α and a which may be easier to calculate.

We can always write

$$\Gamma_{\alpha=1}[a] = \Gamma_{\alpha=0}[a] + \int_0^1 d\alpha \frac{\partial \Gamma_\alpha[a]}{\partial \alpha} \tag{3.13}$$

which is a very general statement, and is known as coupling constant integration. We also know

$$\frac{\partial \Gamma_\alpha[a]}{\partial \alpha} = \langle H_2 \rangle_\alpha [\lambda_\alpha[a]] \tag{3.14}$$

Now we introduce a notational shortcut $a^* \equiv \langle A \rangle_{\alpha=1}[\lambda = 0]$. Plugging Eq. 3.11 and Eq. 3.12 into Eq. 3.13 we obtain

$$\frac{\partial \Gamma_{\alpha=1}[a^*]}{\partial a_i} = \frac{\partial \Gamma_{\alpha=0}[a^*]}{\partial a_i} + \frac{\partial}{\partial a_i} \int_0^1 d\alpha \frac{\partial \Gamma_\alpha[a^*]}{\partial \alpha} = 0 \tag{3.15}$$

and therefore

$$\lambda_{i\,\alpha=0}[a^*] = \frac{\partial}{\partial a_i} \int_0^1 d\alpha \langle H_2 \rangle_\alpha [\lambda_\alpha[a^*]] \tag{3.16}$$

Now we have everything we need to work out the following general expression

$$a_i^* = \langle A_i \rangle_{\alpha=0}[\lambda_{\alpha=0}[a^*]] \tag{3.17}$$

which can be read and understood in the following way - *the true value a_i^* of $\langle A_i \rangle$ corresponding to the original Hamiltonian is the one corresponding to the Legendre transformed Hamiltonian with $\alpha = 0$, but with λ such that it brings $\langle A_i \rangle$ to a_i^*.* This statement is invaluable in practical terms. The solution of the full Hamiltonian with respect to some quantity A can be recast in terms of a different, simpler Hamiltonian, assuming the knowledge of the statistical average of this quantity $a = \langle A \rangle$. The fact that a_i^* appears on both sides of Eq. 3.17 makes it a self-consistent equation. When solved for a_i^*, it yields the *exact* solution of the original problem. For this prescription to have practical value, one needs to be able to solve the representative (or effective) $\alpha = 0$ model with a non-zero λ (in case of WMFT, λ is the effective Weiss field acting on a single Ising spin; in case of DFT, λ is the effective potential entering
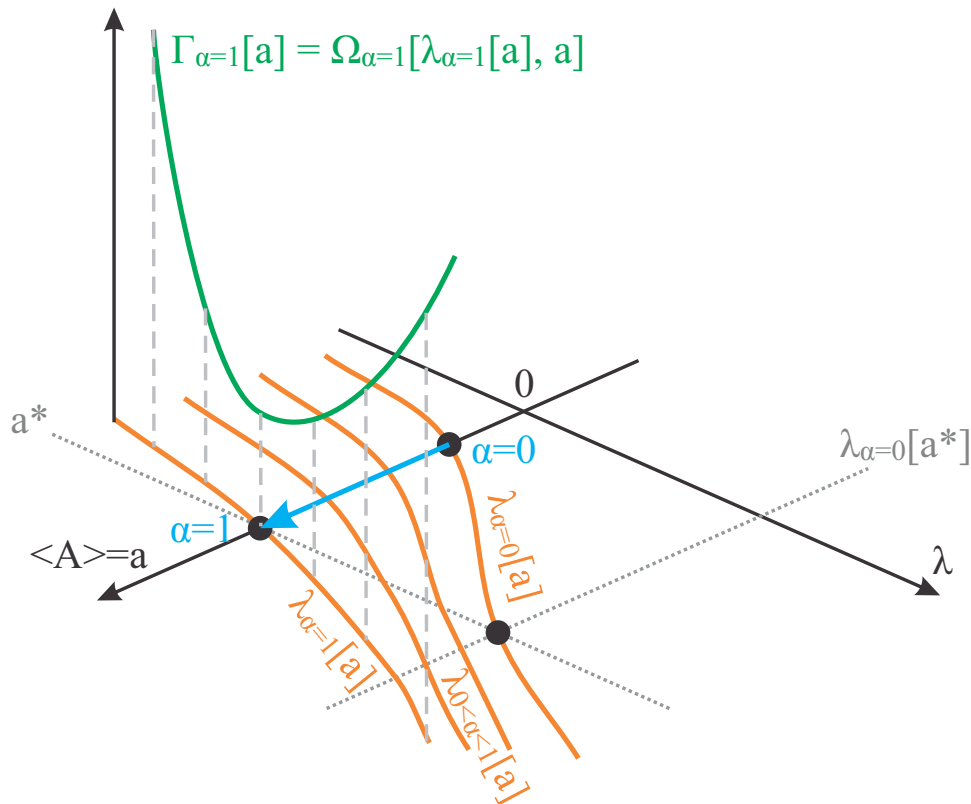
Figure 3.2: Instead of solving the full $\alpha = 1$ problem, one can solve the simpler $\alpha = 0$ problem but with λ such that $\frac{\partial \Gamma_{\alpha=1}\left[\langle A \rangle_{\alpha=0}[\lambda]\right]}{\partial a} = 0$, and that way obtain a^*.

the single-particle Schroedinger equation; in case of DMFT it is the hybridization function in the single-site impurity problem). Also, one needs to be able to express $\langle H_2 \rangle$ in terms of $\langle \hat{A}_i \rangle$, i.e. work out Eq. 3.14, which when plugged into Eq. 3.17, yields a more explicit form

$$a_i^* = \langle A_i \rangle_{\alpha=0} \left[\left\{ \lambda_i = \frac{\partial}{\partial a_i} \int_0^1 d\alpha \langle H_2 \rangle_\alpha [\lambda_\alpha[a^*]] \right\} \right] \tag{3.18}$$

However, it is not always possible to evaluate $\langle \hat{H}_2 \rangle_\alpha [\lambda_\alpha[a]]$. If, for example, $\hat{H}_2$ is purely quartic, i.e. the two-particle interaction term of the original Hamiltonian, then the average value is always possible to split in the disconnected (or mean-field) and connected (correlation) parts. If the correlation part is just assumed zero, the theory reduces to usual mean field theory. Any approximation of the correlation part then introduces corrections beyond the mean-field level. As we shall see, in DMFT, $\hat{H}_2$ is not quartic and therefore $\langle \hat{H}_2 \rangle$ can not be split in two, but the full

statistical average is possible to express in terms of a when the lattice is of infinite dimensionality.

Note also that even if all terms in the self-consistent equation are known, the self-consistent equation may not have a solution at all. There is the fundamental issue of representability - can one find a finite and physical λ such that $\langle A_i \rangle_{\alpha=0}[\lambda] = a^*$? In other words, can one solve Eq. 3.8 for any a? On Fig. 3.2 the problem would correspond to orange line $\lambda_{\alpha=0}[a]$ having no intersection with the grey dotted a^* line. Still, in cases of interest this proves not to be the case.

A few more remarks are here in order, regarding the grand potential landscape in the vicinity of a stationary point. Since the grand potential must be analytic, one can always Taylor expand it in terms of derivatives with respect to λ. Close enough to $\lambda[a], a$ one may keep only the second order term

$$\Omega_\alpha[\lambda \approx \lambda_\alpha[a], a] = \Omega_\alpha[\lambda_\alpha[a], a] + \sum_{ij} \frac{\partial^2 \Omega_\alpha[\lambda, a]}{\partial \lambda_i \partial \lambda_j} (\lambda_i - \lambda_{i\alpha}[a])(\lambda_j - \lambda_{j\alpha}[a]) \quad (3.19)$$

We can switch to matrix notation

$$\Omega_\alpha[\lambda \approx \lambda_\alpha[a], a] = \Omega_\alpha[\lambda_\alpha[a], a] + \delta\vec{\lambda}\, \mathbf{M}\, \delta\vec{\lambda} \quad (3.20)$$

where $\mathbf{M}$ is the fluctuation matrix

$$M_{ij} = \frac{\partial^2 \Omega_\alpha[\lambda, a]}{\partial \lambda_i \partial \lambda_j} \quad (3.21)$$

and

$$(\delta\vec{\lambda})_i = \lambda_i - \lambda_{i\alpha}[a] \quad (3.22)$$

Then, the gradient of the grand potential is

$$\frac{\partial \Omega_\alpha[\delta\lambda, a]}{\partial \lambda_i} = \left(\mathbf{M}\, \delta\vec{\lambda} \right)_i = \left(\sum_m \epsilon_m \left(\delta\vec{\lambda} \right)_m \vec{e}_m \right)_i = \left(\vec{a} - \langle \vec{A} \rangle_\alpha[\lambda] \right)_i \quad (3.23)$$

where m labels eigenvalues ϵ_m and eigenstates $\vec{e}_m$ of the matrix $\mathbf{M}$; $\left(\delta\vec{\lambda} \right)_m$ is the m-th component of $\delta\vec{\lambda}$ in the eigenbasis of $\mathbf{M}$. Note now that the above holds for any α including $\alpha = 0$. This equation is very important, as it will later be used to connect the convergence rate of the forward recursion loop leading to the solution of the self-consistent equation, and the curvature of the Free energy functional in

the vicinity of the stationary point $a^*, \lambda_{\alpha=0}[a^*]$.

In the following, I sketch how the above formalism can be straightforwardly applied to the case of the Hubbard model.

3.1.1.1 Application to the Hubbard model

We start from the general Hubbard Hamiltonian

$$\hat{H} = -\sum_{ij\,\sigma} \left(t_{ij}\, c_{i\sigma}^{\dagger} c_{j\sigma} + \text{h.c.} \right) + U\sum_i n_{i\uparrow} n_{i\downarrow} - \mu \sum_{i\,\sigma} n_{i\sigma} \qquad (3.24)$$

The first term is the total kinetic energy $\hat{T}$ and will play the role of $\hat{H}_2$. The second term is the interaction energy $\hat{U}$. Although this term is quartic in fermionic operators, a single site with interactions is not impossible to solve, and this oportunity is used in DMFT. Together with chemical potential $\mu\hat{N}$, $\hat{U}$ plays the role of the solvable $\hat{H}_1$, which in this case is purely local.

The quantity of interest in DMFT is the local single-particle propagator, or Green's function

$$G_{ii\,\sigma}(\tau - \tau') = \langle T_\tau c_{i\sigma}(\tau) c_{i\sigma}^{\dagger}(\tau') \rangle \qquad (3.25)$$

where T_τ denotes the time-ordered product, and $c_{i\sigma}(\tau)$, $c_{i\sigma}^{\dagger}(\tau')$ are field operators in Heisenberg picture. The Legendre transformed grand potential can be written in the path-integral form

$$\Omega[\Delta, G, \alpha] = -\frac{1}{\beta} \ln \int \mathcal{D}[c^+, c] e^{-S[c^+, c; \Delta, G, \alpha]} \qquad (3.26)$$

($\mathcal{D}[c^+, c]$ denotes the integral over all possible configurations of the time dependent Grassman fields) where

$$
\begin{aligned}
S[c^+, c; \Delta, G, \alpha] \;=\; & \int_0^\beta d\tau \left(\sum_{ij\,\sigma} c_{i\sigma}^+(\tau) \left(\delta_{ij}(\partial_\tau - \mu) - \alpha\, t_{ij} \right) c_{j\sigma}(\tau) \right. \qquad (3.27) \\
& \left. + U\sum_i c_{i\uparrow}^+(\tau) c_{i\downarrow}^+(\tau) c_{i\downarrow}(\tau) c_{i\uparrow}(\tau) \right) \\
& - \int_0^\beta d\tau d\tau' \sum_{i\,\sigma} \Delta_{ii\,\sigma}(\tau - \tau') \left(G_{ii\,\sigma}(\tau - \tau') - c_{i\sigma}(\tau) c_{i\sigma}^+(\tau') \right)
\end{aligned}
$$

Here, Δ plays the role of the Lagrange multiplier λ and will have the physical

meaning of hybridization function in the representative, impurity model. G plays the role of a and $c_{i\sigma}(\tau)c_{i\sigma}^+(\tau')$ is A. Without loss of generality, in the following I restrict to homogeneous paramagnetic solutions such that $G_{ii\sigma} = G$ (and also $\Delta_{ii\sigma} = \Delta$. The representative model is obtained by letting $\alpha = 0$. The fermionic operators do not couple to G, and since hopping terms vanish with $\alpha = 0$, our representative model is a set of decoupled single impurity problems which all yield a same solution for the same hybridization bath Δ, so it is sufficient to solve only one.

$$
\begin{aligned}
S_i[c^+, c; \Delta, \alpha = 0] &= \int_0^\beta d\tau \left(\sum_\sigma c_{i\sigma}^+(\tau) \left(\partial_\tau - \mu \right) c_{i\sigma}(\tau) + U c_{i\uparrow}^+(\tau) c_{i\downarrow}^+(\tau) c_{i\downarrow}(\tau) c_{i\uparrow}(\tau) \right) \\
&\quad - \int_0^\beta d\tau d\tau' \sum_\sigma c_{i\sigma}^+(\tau) \Delta(\tau - \tau') c_{i\sigma}(\tau')
\end{aligned}
\tag{3.28}
$$

Although the fields Δ and G are uniform, they are frequency dependent and need to be evaluated at all Matsubara frequencies n. In the following, $G(i\omega_n) \equiv G_n$.

The self-consistent equation is then given immediately by

$$
G_n^* = G_n \Big[\Delta[G^*, \alpha = 0], \alpha = 0 \Big]
\tag{3.29}
$$

where $G_n [\Delta, \alpha = 0]$ is the solution of the impurity problem stated in Eq. 3.28, for a given Δ. More explicitly, and omitting the asterisk in superscript

$$
G_n = G_n \left[\left\{ \Delta_n = \frac{\partial}{\partial G_n} \int_0^1 d\alpha \langle \hat{T} \rangle [G, \alpha] \right\}, \alpha = 0 \right]
\tag{3.30}
$$

The above two equations correspond directly to equations Eq. 3.17 and Eq. 3.18 in the general discussion. However, the kinetic energy is defined in terms of the spatially resolved Green's function and dispersion $\varepsilon_\mathbf{k}$

$$
\langle \hat{T} \rangle = \sum_{\mathbf{k},n} \varepsilon_\mathbf{k} \, G_{\mathbf{k}n}
\tag{3.31}
$$

and in general is not possible to express in terms of only the local propagator. However, if the self-energy is assumed local and therefore equal to the local self-energy of the impurity problem, the issue is easily resolved. If we have calculated the self-energy in the impurity problem, then the spatially resolved propagator is
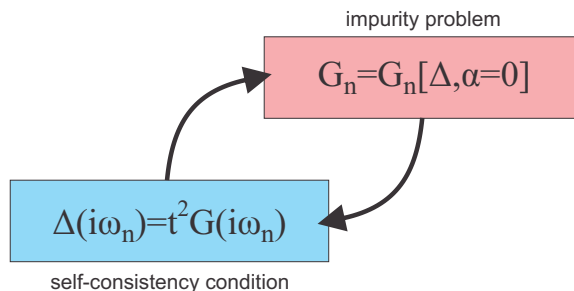
Figure 3.3: Self-consistency in the DMFT equation is achieved by forward recursion.

easily obtained through the general expression

$$G_{\mathbf{k}n} = \frac{1}{i\omega_n + \mu - \varepsilon_{\mathbf{k}} - \Sigma_n}$$

(3.32)

Once again, in infinite dimensions this is not an approximation, and the self-consistent equation can be worked out completely. In the case of the infinitely dimensional Bethe lattice (a.k.a. the Cayley tree - a connected cycle-free graph) with only the nearest neighbor hopping t, it is even very simple - similarly to the local density approximation in DFT where the exchange-correlation potential is no longer considered a functional but rather a *function* of $n(x)$ $(V_{xc}(x)[n] \rightarrow V_{xc}(n(x), x))$, here Δ_n becomes a function of G_n

$$G_n = G_n \left[\left\{ \Delta_n = t^2 \, G_n \right\}, \alpha = 0 \right]$$

(3.33)

This self-consistent equation can be solved most easily by forward recursion as depicted in Fig. 3.3.

However, the prescription for the evaluation of the local propagator in the representative $\alpha = 0$ problem here is not yet specified, and although possible in principle, is not easy. In the following I discuss the infinite dimensionality limit and later use the obtained conclusions to straightforwardly prove the validity (exactness) of DMFT in $d = \infty$. It can be shown that hybridization expansion of the Hubbard model around a single site leads to a completely explicit self-consistent equation (Eq. 3.99, section 3.3.2.1) of the above form. The practical value of Eq. 3.99 is that its right-hand side is ready for a numerical evaluation by stochastic summation of diagrams, i.e. continuous time quantum Monte Carlo which is discussed in section 3.4.1. Furthermore, Eq. 3.99 can be translated to path integral form and "unrolled" to yield the $\alpha = 0$ action which is the impurity model stated in Eq. 3.28. The meth-

ods used for achieving self-consistency of the DMFT equation are also discussed in
section 3.3.2.1.

3.2   Limit of infinite dimensions

The prerequisite for the exact mapping of the Hubbard model onto a model of an
interacting single-site impurity coupled to a non-interacting bath is that the self-
energy (and the irreducible vertex function) are fully local. The physical meaning
of this is that intersite (non-local) correlations are negligible, even for nearest neigh-
bors. When the lattice is infinitely dimensional or at least the coordination number
(the number of neighbors of each lattice site) is infinite, this condition is satisfied.
However, for the Hubbard Hamiltonian to retain its physical meaningfulness in the
(unphysical) limit of infinite lattice dimensionality, it is necessary to rescale the hop-
ping amplitude with $\sqrt{Z}$ where Z is the coordination number [46, 24]. Otherwise,
terms other than the kinetic energy would be completely negligible, and the solution
would be trivial.

It is easily verified that for a tight-binding Hamiltonian with nearest neighbor
hopping of amplitude t, intersite Green's function falls off with the power of Man-
hattan distance between the sites

$$G_{ij}(\omega) = \left\langle i \left| \left(\frac{1}{(\omega + \mu)\hat{I} - \hat{t}} \right)^{-1} \right| j \right\rangle \sim t^{|i-j|} \tag{3.34}$$

where $\hat{t}$ is the hopping matrix, and $\hat{I}$ is the identity matrix. In the limit of infinite
coordination $Z \to \infty$, $t \to \frac{t}{\sqrt{Z}}$, and therefore, $G_{ij}(\omega)$ goes to zero. However, this does
not mean that we can discard all the non-local Green's functions immediately. The
k-dependence of the Green's function is retained even in this limit, because although
a single $G_{ij}(\omega)$ is infinitesimal, a sum over infinitely many Green's functions may
still be finite (and even infinite).

However, a similar conclusion does not hold for all quantities. Most importantly,
the self-energy is necessarily purely local in infinite dimensions. Consider a second
order skeleton diagram in the interaction expansion of the local propagator (Fig. 3.4).

$$G_{ii}^{(2)}(\tau) = U^2 \, G_{ij}(\tau') \, G_{jk}^2(\tau'' - \tau') \, G_{kj}(\tau' - \tau'') \, G_{ki}(\tau - \tau'') \tag{3.35}$$

The summation over internal degrees of freedom (in this case times τ', τ'' and lattice
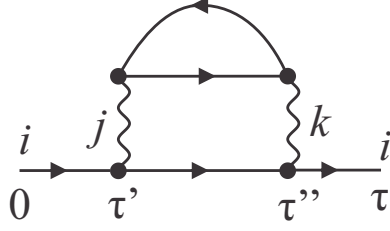
Figure 3.4: Example of the second order skeleton diagram. In infinite dimensions, the only contribution comes from the $j = k = i$ term.

sites j and k) is implicit. Say we want to evaluate the above on a $d = \infty$ hyper-cubic lattice with only the nearest neighbor hopping t. The number of different sites at a Manhattan distance R from the site 0 (located at $\mathbf{r}_0 = 0$) is equal to the surface area of a hypercube of size R, i.e. $2d\,R^{d-1}$. Then, the number of first neighbors Z is proportional to d. In the case $i \neq j \neq k$, if $|i - j|$ and $|j - k|$ are independent, $|i - k|$ can be anywhere from 1 to $|i - j| + |j - k|$. For a given configuration of times, the order of the diagram is then at most

$$\sum_{jk} \left(\frac{1}{\sqrt{d}} \right)^{|i-j|+3|j-k|+|k-i|} \lesssim \sum_{R_1, R_2 \geq 1} d^2 \left(\frac{1}{\sqrt{d}} \right)^{R_1 + 3R_2 + 1} \lesssim \frac{1}{\sqrt{d}} \tag{3.36}$$

The situation is not different even on the infinitely dimensional Bethe lattice (a.k.a. the Cayley tree). When each branch of the tree is the root of another d branches, the number of neighbors at a distance R goes as d^R. Nothing, however, changes

$$\sum_{jk} \left(\frac{1}{\sqrt{d}} \right)^{|i-j|+3|j-k|+|k-i|} \lesssim \sum_{R_1, R_2 \geq 1} d^{R_1 + R_2} \left(\frac{1}{\sqrt{d}} \right)^{R_1 + 3R_2 + 1} \lesssim \frac{1}{\sqrt{d}} \tag{3.37}$$

Although longer distance contributions are now less severely suppressed, they still amount to zero. As long as there are at least 3 propagators connecting any two internal vertices at sites j and k, the non-local ($j \neq k$) contribution of the diagram will be zero. In such diagrams, one can readily replace all the propagators with their local counterparts, simply ignoring the momentum conservation at all vertices. This is the case for any proper self-energy skeleton diagram, except for the first order (Hartree-Fock mean field) diagram, but this one is fully local in any case. In infinite dimensions,

$$\Sigma_{ij}(i\omega) = \delta_{ij}\Sigma_{ii}(i\omega) \implies \Sigma_{\mathbf{k}}(i\omega) = \Sigma(i\omega) \tag{3.38}$$

38

The same stands for the two-particle irreducible vertex function Γ - when calculating many-body Green's functions in infinite dimensions, one needs to consider only vertices with all four terminals at the same site, i.e. Γ looses all the $\mathbf{k}, \mathbf{k}', \mathbf{q}$ dependence. This has important implications for the derivation of DMFT, as well as calculation of two-particle correlation functions, most notably the frequency dependent uniform optical conductivity $\sigma(\mathbf{q} = 0, i\nu)$.

3.2.1 Implications of $d = \infty$ limit for optical conductivity

The quantity in primary focus of this thesis is the zero-frequency (DC) linear-response resistivity. Although in general, evaluating this quantity requires a summation of an infinite series of diagrams, in infinite dimensions, the irreducible vertex function Γ (and therefore also the full vertex function F) is purely local making the contribution of all the higher order (order larger than 2) terms cancel exactly. This can be most easily proven in the case of the $d = \infty$ hypercubic lattice, but holds as well in the case of the Bethe lattice [47, 48]. In this work, we solve the DMFT equations for the $d = \infty$ Bethe lattice, and therefore calculate resistivity using only the first, bare bubble term which is not particularly hard to evaluate. In the following I derive the equation used in this purpose.

Let $\mathcal{O}(\mathbf{q})$ be an operator of the form.

$$\mathcal{O}(\mathbf{q}) = \sum_{\mathbf{k},\sigma} v_{\mathbf{k}\sigma} c^\dagger_{\mathbf{k}\sigma} c_{\mathbf{k}+\mathbf{q}\sigma} \tag{3.39}$$

defined by the vertex factor $v_{\mathbf{k}\sigma}$. Then, the corresponding linear response function is given by

$$
\begin{aligned}
\chi(\mathbf{q}, i\nu) &= \int_0^\beta d\tau e^{i\nu\tau} \langle \mathcal{O}(\mathbf{q}, \tau)\mathcal{O}(-\mathbf{q}, 0) \rangle \tag{3.40} \\
&= \sum_{i\omega,\mathbf{k},\sigma} v_{\mathbf{k}\sigma} G^{i\omega}_{\mathbf{k}\sigma} G^{i\omega+i\nu}_{\mathbf{k}+\mathbf{q}\sigma} v_{\mathbf{k}+\mathbf{q}\sigma} \\
&\quad + \sum_{i\omega,\mathbf{k},i\omega',\mathbf{k}',\sigma,\sigma'} v_{\mathbf{k}\sigma} G^{i\omega}_{\mathbf{k}\sigma} G^{i\omega+i\nu}_{\mathbf{k}+\mathbf{q}\sigma} \Gamma^{i\omega\,i\omega'\,i\nu}_{\mathbf{k}\mathbf{k}'\mathbf{q}\sigma\sigma'} G^{i\omega'}_{\mathbf{k}\sigma'} G^{i\omega'+i\nu}_{\mathbf{k}'+\mathbf{q}\sigma'} v_{\mathbf{k}'+\mathbf{q}\sigma'} + \dots
\end{aligned}
$$

where $G^{i\omega}_{\mathbf{k}\sigma}$ is the full single-particle propagator given by

$$G^{i\omega}_{\mathbf{k}\sigma} = \frac{1}{\omega + \mu - \varepsilon_{\mathbf{k}\sigma} - \Sigma^{i\omega}_{\mathbf{k}\sigma}}. \tag{3.41}$$
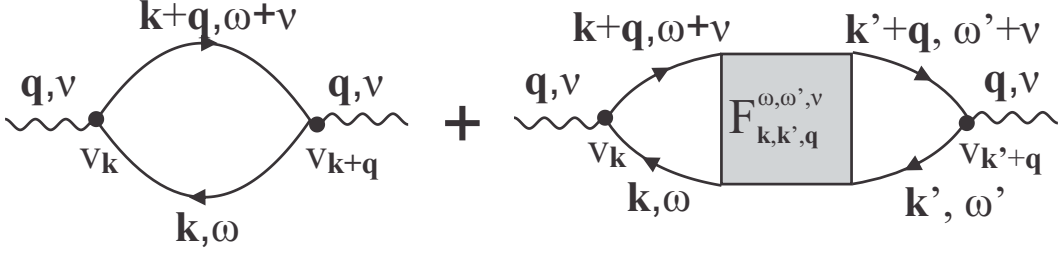
Figure 3.5: When the full vertex function is local, $\mathbf{q} = 0$ and $v_{\mathbf{k}} = -v_{-\mathbf{k}}$, the response function can be calculated from the bare bubble term only.

See Fig. 3.5. The compact notation with frequencies omitted or denoted in the superscript will be used occasionally throughout this thesis, for the sake of clarity. In infinite dimensions, $\Sigma_{\mathbf{k}} = \Sigma$, and $\Gamma_{\mathbf{k}\mathbf{k}'\mathbf{q}} = \Gamma$. If the system is invariant under coordinate inversion $x \longrightarrow -x$ (which is the case for most lattices), and spin-symmetry is preserved at the level of the non-interacting Hamiltonian, $\varepsilon_{\mathbf{k}\sigma} = \varepsilon_{\mathbf{k}} = \varepsilon_{-\mathbf{k}}$, and therefore, $G_{\mathbf{k}} = G_{-\mathbf{k}}$. Then, if $\mathbf{q} = 0$ and

$$\sum_{\mathbf{k},\sigma} v_{\mathbf{k}\sigma} = 0 \tag{3.42}$$

all the vertex corrections get canceled, and one needs to evaluate only the bare bubble term (it can not be canceled as $v_{\mathbf{k}\sigma}^2$ is always positive). In the case of current-current correlation along the x direction, vertex factor is nothing but the group velocity

$$v_{\mathbf{k}\sigma} = \frac{\partial \varepsilon_{\mathbf{k}}}{\partial k_x} \tag{3.43}$$

which on the hypercubic lattice is spin independent and yields

$$v_{\mathbf{k}} = -2t \frac{\partial \sum_{i=1}^{\infty} \cos k_{x_i}}{\partial k_{x_j}} = 2t \sin k_{x_j} \tag{3.44}$$

so

$$v_{\mathbf{k}} = -v_{-\mathbf{k}} \tag{3.45}$$

This expression satisfies Eq. 3.42 and therefore, the uniform current-current correlation function can be calculated from the knowledge of the single-particle properties only

$$\Lambda(i\nu) = T \sum_{i\omega,\mathbf{k},\sigma} v_{\mathbf{k}}^2 \, G_{\mathbf{k}\sigma}^{i\omega} \, G_{\mathbf{k}\sigma}^{i\omega+i\nu} \tag{3.46}$$

where T denotes temperature. The uniform optical conductivity is calculated from the uniform current-current correlation function

$$\sigma(i\nu) = \frac{\Lambda(0) - \Lambda(i\nu)}{\nu} \tag{3.47}$$

This expression can be analytically continued to the real frequency. First we note that

$$G_{\mathbf{k}}^{i\omega} = -\int d\omega' \frac{A_{\mathbf{k}}^{\omega'}}{i\omega - \omega'} \tag{3.48}$$

where $A_{\mathbf{k}}^{\omega} = -\frac{1}{\pi}\mathrm{Im}\, G_{\mathbf{k}}^{\omega}$ is the spectral function. This expression corresponds to the analytical continuation from the real to the imaginary axis. Plugging this back in the expression for the current-currect correlation function, we obtain

$$\Lambda(i\nu) = 2\sum_{\mathbf{k}} v_{\mathbf{k}}^2 \int d\omega' A_{\mathbf{k}}^{\omega'} \int d\omega'' A_{\mathbf{k}}^{\omega''}\, T \sum_{i\omega} \frac{1}{(i\omega - \omega')(i\omega + i\nu - \omega'')} \tag{3.49}$$

where the prefactor 2 comes from the summation over spin. The Matsubara sum can be now performed for each ω' and ω'' to yield

$$\Lambda(i\nu) = -2\sum_{\mathbf{k}} v_{\mathbf{k}}^2 \int d\omega' A_{\mathbf{k}}^{\omega'} \int d\omega'' A_{\mathbf{k}}^{\omega''}\, \frac{f(\omega') - f(\omega'')}{\omega' - \omega'' + i\nu} \tag{3.50}$$

where f is the Fermi distribution

$$f(\omega) = (\exp(\beta\omega) + 1)^{-1} \tag{3.51}$$

Now only the denominator depends on the matsubara frequency and one can perform the analytical continuation by formally letting $i\nu \to \nu$. However, the integrand now has poles at $\omega' - \omega'' + \nu = 0$. The well known relation

$$\lim_{\eta \to 0} \frac{1}{x + i\eta} = \mathcal{P}\frac{1}{x} - i\pi\delta(x) \tag{3.52}$$

yields for the imaginary part in our case

$$\mathrm{Im}\Lambda(\nu) = 2\pi \sum_{\mathbf{k}} v_{\mathbf{k}}^2 \int d\omega' A_{\mathbf{k}}^{\omega'} A_{\mathbf{k}}^{\omega'+\nu}\, (f(\omega') - f(\omega' + \nu)) \tag{3.53}$$

We see immediately that in real frequency

$$\text{Im}\Lambda(\nu = 0) = 0 \qquad (3.54)$$

end therefore the real part of the optical conductivity, obtained with $\frac{1}{\nu} = \frac{i}{i\nu} \rightarrow \frac{i}{\nu}$ and $\omega \equiv \nu$

$$\text{Re}\,\sigma(\omega) = \frac{2}{\pi} \sum_{\mathbf{k}} \int d\omega'\, v_{\mathbf{k}}^2 \,\text{Im}G_{\mathbf{k}}^{\omega'} \,\text{Im}G_{\mathbf{k}}^{\omega+\omega'} \,\frac{f(\omega') - f(\omega' + \omega)}{\omega} \qquad (3.55)$$

On the Bethe lattice, translational symmetry is not satisfied, and $\mathbf{k}$ is not a good quantum number. However, the same considerations apply and the group velocity can be shown to depend on the energy of the non-interacting state as

$$v(\varepsilon) = \pm\sqrt{W^2 - \varepsilon^2} \qquad (3.56)$$

where $W = 2t$ is the half-bandwidth. One can then switch to the integral over energy

$$\text{Re}\,\sigma(\omega) = \frac{2}{\pi} \int d\varepsilon d\omega'\, v^2(\varepsilon)\rho(\varepsilon) \,\text{Im}G_{\varepsilon}^{\omega'} \,\text{Im}G_{\varepsilon}^{\omega+\omega'} \,\frac{f(\omega') - f(\omega' + \omega)}{\omega} \qquad (3.57)$$

where ρ is the non-interacting density of states (DOS) on the Bethe lattice, $G_{\varepsilon\sigma}^{\omega}$ is simply $(\omega + \mu - \varepsilon - \Sigma(\omega))^{-1}$. Note that up to a prefactor, $v(\varepsilon)$ is the same as the non-interacting density of states on the Bethe lattice. The vertex factor can be absorbed into DOS to yield the "transport density of states" which is only slightly different than the original DOS. It has been shown earlier and confirmed in this work as well, that excluding this vertex factor altogether (setting it to 1) does not change the result noticably (only up to a multiplicative constant). The zero frequency limit is

$$\sigma_{DC} \equiv \text{Re}\,\sigma(\omega = 0) = -\frac{2}{\pi} \int d\varepsilon d\omega'\, v^2(\varepsilon)\rho(\varepsilon) \left(\text{Im}G_{\varepsilon}^{\omega'}\right)^2 \left.\frac{\partial f}{\partial \omega}\right|_{\omega=0} \qquad (3.58)$$

which is the formula used throughout this thesis.

3.3 Explicit DMFT self-consistent equation

In this section I derive the DMFT self-consistent equation by performing a hybridization expansion of the local propagator around a single lattice site of the Hubbard model [49]. The derivation is kept general in section 3.3.1 where I discuss the hybridization expansion in the context of a generalized impurity problem. Then in section 3.3.2 I identify the impurity and bath Hamiltonians with a single lattice site and the rest of the lattice. In the end, a detailed prescription for achieving self-consistency of the DMFT equation is given in form of a simple algorithm. The derivation is carried out for the $d = \infty$ Bethe and hypercubic lattices.

3.3.1 Hybridization expansion of a generalized impurity model

We start from a general (particle number conserving) Hamiltonian such that it can be split in 3 parts

$$\hat{H} = \hat{H}_a + \hat{H}_b + \hat{H}_{hyb} \tag{3.59}$$

Hamiltonians a and b depend on disjunct sets of fermionic degrees of freedom d_i and c_i respectively, and the third part $\hat{H}_{hyb}$ defines the hybridization between the two subsystems, i.e. connects some of d_i's with some of c_i's. In general

$$\hat{H}_{hyb} = \sum_{\alpha,p} (V_p^{\alpha*} \, d_\alpha^\dagger c_p + \text{h.c.}) \tag{3.60}$$

α enumerates the "flavor" (merged spin, band, site index etc.) of the states in the a subsystem, and p of the states in the b subsystem. $V_p^{\alpha*}$ is the hybridization amplitude between the states α and p and in general may be complex. The type of Hamiltonian $\hat{H}$ corresponds to a general impurity problem.

To calculate the expectation value of an operator $\hat{A}$ one must evaluate the following expression

$$\langle \hat{A} \rangle = \frac{1}{Z} \text{Tr} \left[T_\tau \hat{A}(\tau_1, \tau_2, ...) \, e^{-\int_0^\beta d\tau \hat{H}(\tau)} \right] \tag{3.61}$$

where $\beta = 1/T$ is the inverse temeprature, τ is the imaginary time, T_τ is the time-order operator. If the Hamiltonian $\hat{H}$ is interacting, then the trace is taken over a many-body basis. We first analyze the partition function Z. After plugging our

Hamiltonian in the general expression for Z, we obtain

$$Z = \text{Tr}\left[T_\tau\, e^{-\int_0^\beta d\tau(\hat{H}_a + \hat{H}_b + \hat{H}_{hyb})}\right] \quad (3.62)$$

Here we assume that the Hamiltonian is only trivially dependent (not actually dependent) on time, but in general, this may not be the case (e.g. phonon mediated interactions are usually retarded; effects of screening may also be included as frequency dependence of on-site interaction). We can now Taylor-expand in the hybridization part of the Hamiltonian so we get

$$Z = \text{Tr}\left[T_\tau\, e^{-\int_0^\beta d\tau(\hat{H}_a + \hat{H}_b)}\ \sum_{k=0}^\infty \frac{(-1)^k}{k!}(\int_0^\beta d\tau \hat{H}_{hyb})^k\right] \quad (3.63)$$

$$\begin{aligned}
Z\ =\ &\text{Tr}\Big[T_\tau\, e^{-\int_0^\beta d\tau(\hat{H}_a + \hat{H}_b)} \\
&\times \sum_{k=0}^\infty \frac{(-1)^k}{k!} \int_0^\beta d\tau_1 \int_0^\beta d\tau_2 ... \int_0^\beta d\tau_k\ \hat{H}_{hyb}(\tau_1)\hat{H}_{hyb}(\tau_2)...\hat{H}_{hyb}(\tau_k)\Big]
\end{aligned} \quad (3.64)$$

Now we introduce notation

$$\hat{H}_{hyb} = \hat{H}_h^\dagger + \hat{H}_h \quad (3.65)$$

where

$$\hat{H}_h^\dagger = \sum_{\alpha,p} V_p^{\alpha*}\, d_\alpha^\dagger c_p$$

$$\hat{H}_h = \sum_{\alpha,p} V_p^\alpha\, c_p^\dagger d_\alpha \quad (3.66)$$

We also note that

$$\int_0^a \int_0^a ... \int_0^a dx_1 dx_2 ... dx_N f(x_1)f(x_2)...f(x_N) \quad (3.67)$$

$$= N! \int_0^a \int_{x_1}^a ... \int_{x_{N-1}}^a dx_1 dx_2 ... dx_N f(x_1)f(x_2)...f(x_N) \quad (3.68)$$

so we have

$$
\begin{aligned}
Z \;=\; & \sum_{k=0}^{\infty} (-1)^k \int_0^\beta d\tau_1 \int_{\tau_1}^\beta d\tau_2 ... \int_{\tau_{k-1}}^\beta d\tau_k \, \mathrm{Tr}\left[T_\tau \, e^{-\int_0^\beta d\tau (\hat{H}_a + \hat{H}_b)} \right. \\
& \left. \times (\hat{H}_h^\dagger(\tau_1) + \hat{H}_h(\tau_1)) ... (\hat{H}_h^\dagger(\tau_k) + \hat{H}_h(\tau_k)) \right]
\end{aligned}
\tag{3.69}
$$

Because both Hamiltonians (H_a and H_b) conserve the number of particles, only the terms with equal number of $H_h^\dagger$ and H_h can give non-zero trace, so we're left with only the even orders k and only a fraction of 2^k terms for each k - for a given k we get $(2k)!/(k!)^2$ terms with k $H^\dagger$ and k H factors

$$
\begin{aligned}
Z \;=\; & \sum_{k=0}^{\infty} \int_0^\beta d\tau_1 \int_{\tau_1}^\beta d\tau_2 ... \int_{\tau_{2k-1}}^\beta d\tau_{2k} \\
& \mathrm{Tr}\left[T_\tau \, e^{-\int_0^\beta d\tau (\hat{H}_a + \hat{H}_b)} \times \sum_{P=1}^{(2k)!/(k!)^2} \prod_{i=1}^{2k} \hat{H}_h^{(X_i(P))}(\tau_i) \right]
\end{aligned}
\tag{3.70}
$$

where P goes over all possible choices $\{X_i\}$ such that exactly k out of $2k$ operators are "daggered" (each X is either $\dagger$ or 1). Now let's look at a concrete example, say $k = 2$. We have

$$
\int_0^\beta d\tau_1 \int_{\tau_1}^\beta d\tau_2 \int_{\tau_2}^\beta d\tau_3 \int_{\tau_3}^\beta d\tau_4
\tag{3.71}
$$

$$
\times \left(H_h^\dagger(\tau_1) H_h^\dagger(\tau_2) H_h(\tau_3) H_h(\tau_4) + \right.
\tag{3.72}
$$

$$
H_h^\dagger(\tau_1) H_h(\tau_2) H_h^\dagger(\tau_3) H_h(\tau_4) +
\tag{3.73}
$$

$$
H_h^\dagger(\tau_1) H_h(\tau_2) H_h(\tau_3) H_h^\dagger(\tau_4) +
\tag{3.74}
$$

$$
H_h(\tau_1) H_h^\dagger(\tau_2) H_h^\dagger(\tau_3) H_h(\tau_4) +
\tag{3.75}
$$

$$
H_h(\tau_1) H_h^\dagger(\tau_2) H_h(\tau_3) H_h^\dagger(\tau_4) +
\tag{3.76}
$$

$$
\left. H_h(\tau_1) H_h(\tau_2) H_h^\dagger(\tau_3) H_h^\dagger(\tau_4) \right)
\tag{3.77}
$$

Now, we can conveniently rewrite the above expression by noting that each term can be obtained from the first one by an appropriate exchange of the indices, respectively $2 \leftrightarrow 3, 2 \leftrightarrow 4, 1 \leftrightarrow 3, 1 \leftrightarrow 4$ and both $2 \leftrightarrow 4, 1 \leftrightarrow 3$. So instead of always having $\tau_4 > \tau_3 > \tau_2 > \tau_1$ we can rearrange the integration limits to allow $\tau_1 > \tau_3$, $\tau_1 > \tau_4$, $\tau_2 > \tau_3$, $\tau_2 > \tau_4$, but keep $\tau_1 < \tau_2$ and $\tau_3 < \tau_4$ and this way account for all the terms only once. Note that this is possible because all the terms will in the end be time

ordered, so nothing depends on the order of operators at this stage - only which operator ($H_h^\dagger$ or H_h) acts at what time is important. We have

$$
\begin{aligned}
Z \;=\; & \sum_{k=0}^{\infty} \int_0^\beta d\tau_1 \int_{\tau_1}^\beta d\tau_2 ... \int_{\tau_{k-1}}^\beta d\tau_k \int_0^\beta d\tau_1' \int_{\tau_1'}^\beta d\tau_2' ... \int_{\tau_{k-1}'}^\beta d\tau_k' \\
& \mathrm{Tr}\left[T_\tau \, e^{-\int_0^\beta d\tau(\hat{H}_a+\hat{H}_b)} \right. \\
& \left. \times \hat{H}_h^\dagger(\tau_1)\hat{H}_h^\dagger(\tau_2)...\hat{H}_h^\dagger(\tau_k) \, \hat{H}_h(\tau_1')\hat{H}_h(\tau_2')...\hat{H}_h(\tau_k') \right]
\end{aligned}
\tag{3.78}
$$

where we have two sets of k times - one associated with $H_h^\dagger$ and the other with H_h. Now let's write the operators explicitly

$$
\begin{aligned}
Z \;=\; & \sum_{k=0}^{\infty} \int_0^\beta d\tau_1 \int_{\tau_1}^\beta d\tau_2 ... \int_{\tau_{k-1}}^\beta d\tau_k \int_0^\beta d\tau_1' \int_{\tau_1'}^\beta d\tau_2' ... \int_{\tau_{k-1}'}^\beta d\tau_k' \\
& \mathrm{Tr}\left[T_\tau \, e^{-\int_0^\beta d\tau(\hat{H}_a+\hat{H}_b)} \sum_{\alpha_1...\alpha_k} \sum_{\alpha_1'...\alpha_k'} \sum_{p_1...p_k} \sum_{p_1'...p_k'} V_{p_1}^{\alpha_1*}...V_{p_k}^{\alpha_k*} V_{p_1'}^{\alpha_1'}...V_{p_k'}^{\alpha_k'} \right. \\
& \left. \times d_{\alpha_1}^\dagger(\tau_1)c_{p_1}(\tau_1)...d_{\alpha_k}^\dagger(\tau_k)c_{p_k}(\tau_k)c_{p_1'}^\dagger(\tau_1')d_{\alpha_1'}(\tau_1')...c_{p_k'}^\dagger(\tau_k')d_{\alpha_k'}(\tau_k') \right]
\end{aligned}
\tag{3.79}
$$

Since the Hamiltonian $\hat{H}_a + \hat{H}_b$ does not mix α and p states, we can do the trace independently with respect to d and c operators

$$
\begin{aligned}
Z \;=\; & \sum_{k=0}^{\infty} \int_0^\beta d\tau_1 \int_{\tau_1}^\beta d\tau_2 ... \int_{\tau_{k-1}}^\beta d\tau_k \int_0^\beta d\tau_1' \int_{\tau_1'}^\beta d\tau_2' ... \int_{\tau_{k-1}'}^\beta d\tau_k' \\
& \times \sum_{\alpha_1...\alpha_k} \sum_{\alpha_1'...\alpha_k'} \mathrm{Tr}_d\left[T_\tau \, e^{-\int_0^\beta d\tau \hat{H}_a} d_{\alpha_1}^\dagger(\tau_1)...d_{\alpha_k}^\dagger(\tau_k)d_{\alpha_1'}(\tau_1')...d_{\alpha_k'}(\tau_k') \right] \\
& \times \sum_{p_1...p_k} \sum_{p_1'...p_k'} V_{p_1}^{\alpha_1*}...V_{p_k}^{\alpha_k*} V_{p_1'}^{\alpha_1'}...V_{p_k'}^{\alpha_k'} \\
& \times \mathrm{Tr}_c\left[T_\tau \, e^{-\int_0^\beta d\tau \hat{H}_b} c_{p_1}(\tau_1)...c_{p_k}(\tau_k)c_{p_1'}^\dagger(\tau_1')...c_{p_k'}^\dagger(\tau_k') \right]
\end{aligned}
\tag{3.80}
$$

However, if both H_a and H_b are interacting, evaluating these traces is in general an impossible task. It is only possible if both a and b systems are small (of the order of 10 states), but if they are non-interacting, the calculation is rather straight-forward even for infinite systems. Note that both traces correspond to evaluating k-body

propagators. If partial Z_a and Z_b are known than we can rewrite

$$
\begin{aligned}
Z \;=\; & Z_a Z_b \sum_{k=0}^{\infty} \int_0^{\beta} d\tau_1 \int_{\tau_1}^{\beta} d\tau_2 ... \int_{\tau_{k-1}}^{\beta} d\tau_k \int_0^{\beta} d\tau_1' \int_{\tau_1'}^{\beta} d\tau_2' ... \int_{\tau_{k-1}'}^{\beta} d\tau_k' \\
& \times \sum_{\alpha_1 ... \alpha_k} \sum_{\alpha_1' ... \alpha_k'} G^a_{\alpha_1',...,\alpha_k',\alpha_1,...,\alpha_k}(\tau_1', ..., \tau_k', \tau_1, ..., \tau_k) \\
& \times \sum_{p_1 ... p_k} \sum_{p_1' ... p_k'} V^{\alpha_1 *}_{p_1} ... V^{\alpha_k *}_{p_k} V^{\alpha_1'}_{p_1'} ... V^{\alpha_k'}_{p_k'} \\
& \times G^b_{p_1,...,p_k,p_1',...,p_k'}(\tau_1, ..., \tau_k, \tau_1', ..., \tau_k')
\end{aligned}
\tag{3.81}
$$

where G^a and G^b are the many-body Green's functions, evaluated with respect to a and b Hamiltonians. See Fig. 3.6
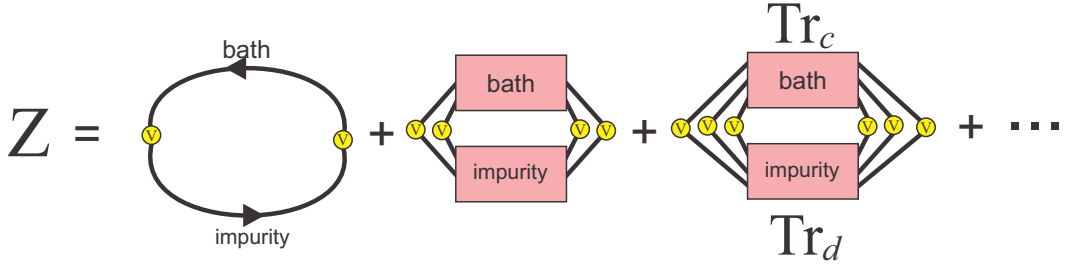
Figure 3.6: The hybridization expansion series of partition function diagrams. "Bath" and "impurity" correspond to b and a Hamiltonians respectively.

3.3.2 Hybridization expansion of the Hubbard model around a single site

So far, the analysis has been completely general. We will now focus on concrete example of the Hubbard model in infinite dimensions. Let $\hat{H}$ be the Hubbard Hamiltonian

$$
\hat{H} = -t \sum_{\langle i,j \rangle, \sigma} \left(c_i^\dagger c_j + \text{h.c.} \right) + U \sum_i n_{i\uparrow} n_{i\downarrow} - \mu \sum_{i,\sigma} n_{i,\sigma}
\tag{3.82}
$$

where the rescaling of the hopping amplitude is assumed implicit $t \equiv t/\sqrt{d}$. μ is the chemical potential and U is the on-site interaction amplitude. We now split this Hamiltonian to resemble the impurity model. We single out one site and make it subsystem a (the atomic part), the rest of the lattice is then the bath b, and the hopping terms between a and b are the hybridization part of the Hamiltonian H_{hyb}.

$$\hat{H}_a = -\mu \sum_\sigma n_{0\sigma} + U n_{0\uparrow} n_{0\downarrow} \qquad (3.83)$$

and

$$\hat{H}_b = \hat{H}^{(0)} = -t \sum_{\langle i,j \rangle, i,j \neq 0, \sigma} \left(c_i^\dagger c_j + \text{h.c.} \right) + U \sum_{i \neq 0} n_{i\uparrow} n_{i\downarrow} - \mu \sum_{i \neq 0, \sigma} n_{i,\sigma} \qquad (3.84)$$

where $\hat{H}^{(0)}$ denotes the full hamiltonian with site 0 excluded, even from the hopping terms, and therefore

$$\hat{H}_{hyb} = -t \sum_{\langle 0,j \rangle, \sigma} \left(c_0^\dagger c_j + \text{h.c.} \right) \qquad (3.85)$$

Here we make an indetification $d^\dagger \equiv c_0^\dagger$, i.e. the atomic Hamiltonian has only 2 states ($d_\uparrow$ and $d_\downarrow$), so α counts only spins and will be replaced by σ. Note that there is now a restriction on the order of appearance of the d operators because $d_\uparrow^\dagger d_\uparrow^\dagger = 0$, so creation and annihilation operators of the same spin must appear in alternating order. Hybridization amplitudes are now purely real and all the same $-t$.

$$
\begin{aligned}
Z &= Z_a Z_b \sum_{k=0}^\infty \int_0^\beta d\tau_1 \int_{\tau_1}^\beta d\tau_2 ... \int_{\tau_{k-1}}^\beta d\tau_k \int_0^\beta d\tau_1' \int_{\tau_1'}^\beta d\tau_2' ... \int_{\tau_{k-1}'}^\beta d\tau_k' \\
&\times \sum_{\sigma_1 ... \sigma_k} \sum_{\sigma_1' ... \sigma_k'} G^a_{\sigma_1', ..., \sigma_k', \sigma_1, ..., \sigma_k}(\tau_1', ..., \tau_k', \tau_1, ..., \tau_k) \\
&\times \sum_{p_1 ... p_k} \sum_{p_1' ... p_k'} t^{2k} G^b_{p_1, ..., p_k, p_1', ..., p_k'}(\tau_1, ..., \tau_k, \tau_1', ..., \tau_k') \qquad (3.86)
\end{aligned}
$$

Note that p indices do not necessarily run over all states in the bath (though this is true for the fully connected lattice), but only over the nearest neigbors of site 0. Until now we haven't specified the type of the lattice. Now we analyze the bath propagator on two $d = \infty$ lattices of interest.

3.3.2.1 Bethe lattice

Between any two sites on the Bethe lattice, there is only one independent path. When a site is taken out from this lattice, all its nearest neighbors become completely disconnected. As p states go over the nearest neighbors of the site 0 which is the

one site missing in b, we immediately see that

$$G^b_{pp'} = \delta_{pp'} G^b_{pp} \tag{3.87}$$

Note also that p and p' need to have the same spin because both H_a and H_b do not mix spins. Furthermore, in the thermodynamic limit, nothing must change when we cut one single branch off the Bethe lattice. Therefore,

$$G^b_{pp} = G^{a+b+hyb}_{pp} \equiv G_{pp} \tag{3.88}$$

In a homogenous phase, also must hold

$$G_{pp} = G, \forall p \tag{3.89}$$

So, in the first order $k = 1$, we loose one sum, but we have d nearest neighbors to cancel the rescaling of the hopping amplitude. We have

$$\frac{t^2}{d} \sum_{pp'} G_{pp'} = \frac{t^2}{d} \sum_{p} G_{pp} = \frac{t^2}{d} d\, G = t^2\, G \tag{3.90}$$

where the rescaling factor of the hopping amplitude is written explicitly.

Now, let's see what happens in the second order, where the summation is carried over the two-particle propagators

$$\frac{t^4}{d^2} \sum_{ijkl} G^b_{ijkl}. \tag{3.91}$$

Here we use i, j, k, l to denote the p states for clarity. The times $\tau_1..\tau_2'$ are assumed fixed. In the non-interacting limit, many-particle propagators can be expressed in terms of the single-particle propagator, using the Wick theorem. In our case, Hamiltonian conserves the number of particles, so anomalous Green's functions do not contribute. We get two terms

$$G_{ijkl} = G_{ij}G_{kl} - G_{il}G_{kj} \tag{3.92}$$

When there are interactions, however, this is not possible. Even if the full single-particle propagator is known, all the possible arrangements of vertices still must
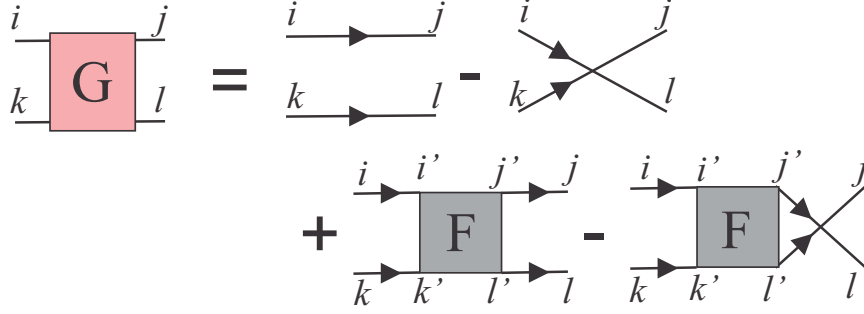
Figure 3.7: The direct space Bethe-Salpeter equation.

be included. These are summed in the full vertex function F. The Bethe-Salpeter equation for the two-particle propagators reads (Fig. 3.7)

$$
\begin{aligned}
G_{ijkl} &= G_{ij}G_{kl} - G_{il}G_{kj} \\
&\quad + G_{ii'}G_{kk'}\,F_{i'j'k'l'}\,G_{j'j}G_{l'l} \\
&\quad - G_{ii'}G_{kk'}\,F_{i'j'k'l'}\,G_{i'l}G_{l'j}
\end{aligned}
\tag{3.93}
$$

where the summation over the internal site indices and intergration over internal times are implicit. In our case, i, j, k and l are disconnected, so only the propagators with all indices doubled are different from 0

$$
G^b_{iijj} = G_{ii}G_{jj} + G_{ii'}G_{jj'}\,F_{i'j'i''j''}\,G_{i''i}G_{j''j}
\tag{3.94}
$$

and

$$
G^b_{ijij} = -G_{ii}G_{jj} - G_{ii'}G_{jj'}\,F_{i'j'i''j''}\,G_{i''i}G_{j''j}
\tag{3.95}
$$

where i', i'' run over the sites in the i branch, and j', j'' over the sites in j branch. As no interactions can occur between electrons on different (disconnected) branches, unless $i = j$, F here is strictly zero. Note that the single-particle propagators are already dressed - the full vertex function only includes interactions between the two incoming fermionic lines (which may be mediated by bubbles, but if the two lines can not meet at the same site, no vertices can appear). We obtain

$$
\frac{t^4}{d^2}\sum_{ijkl}G^b_{ijkl} = \frac{t^4}{d^2}\left(\sum_i G^b_{iiii} + \sum_{ij,i\neq j} G^b_{iijj} + \sum_{ij,i\neq j} G^b_{ijij}\right)
\tag{3.96}
$$
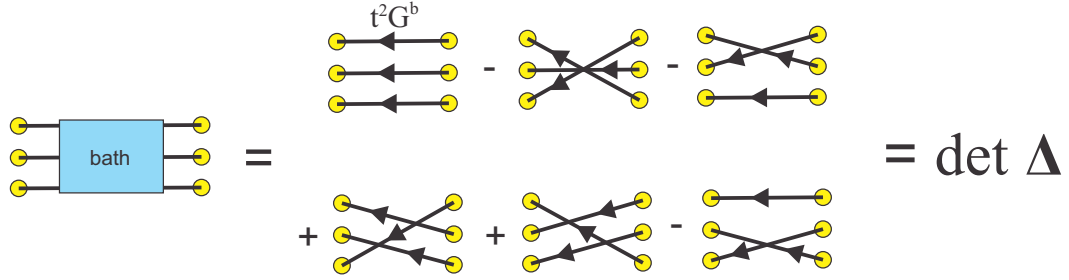
Figure 3.8: No two-body vertices can appear in the many-body Green's function through the bath, i.e. the bath is effectively non-interacting. Just as in the non-interacting case, the many-bopdy propagator reduces to a sum of products of single-particle propagators.

However, the first term contains only one sum, so its contribution will be zero

$$\frac{t^4}{d^2} \sum_i G_{iiii}^b \sim \frac{t^4}{d^2}\, d \sim \frac{1}{d} \tag{3.97}$$

So, even though the H_b contains interactions, the two-body (and any many-body) propagator in expression Eq. 3.86 can be calculated in a Wick-like manner, i.e. the bath is effectively non-interacting and can be expressed entirely in terms of the local Green's function of the whole lattice $(a + b + hyb)$. Using the notation from Eq.3.88 and stating the times explicitly

$$\frac{t^4}{d^2} \sum_{ijkl} G_{ijkl}^b = t^4 \left(G(\tau_1, \tau_1')G(\tau_2, \tau_2') - G(\tau_1, \tau_2')G(\tau_2, \tau_1') \right) \tag{3.98}$$

$$= t^4 \det \begin{pmatrix} G(\tau_1, \tau_1') & G(\tau_1, \tau_2') \\ G(\tau_2, \tau_1') & G(\tau_2, \tau_2') \end{pmatrix}$$

Note that the Hamiltonian preserves time translation symmetry, so nothing must depend on the times but only on the difference between times.

A similar analysis can be carried out for the arbitrary order of diagram k to

obtain the mean-field self-consistent equation

$$
\begin{aligned}
G_\sigma(\tau' - \tau) \;=\; & \sum_{k=0}^{\infty} \int_0^\beta d\tau_1 \int_{\tau_1}^\beta d\tau_2... \int_{\tau_{k-1}}^\beta d\tau_k \int_0^\beta d\tau_1' \int_{\tau_1'}^\beta d\tau_2'... \int_{\tau_{k-1}'}^\beta d\tau_k' \\
& \times \sum_{\sigma_1...\sigma_k} \sum_{\sigma_1'...\sigma_k'} \mathrm{Tr}_d \left[T_\tau\, e^{-\int_0^\beta d\tau\, \hat{H}_a}\, d_\sigma^\dagger(\tau) d_\sigma(\tau') d_{\sigma_1}^\dagger(\tau_1)...d_{\sigma_k}^\sigma(\tau_k) d_{\sigma_1'}(\tau_1')...d_{\sigma_k'}(\tau_k') \right] \\
& \times \det \boldsymbol{\Delta}_k
\end{aligned}
\tag{3.99}
$$

where

$$
\boldsymbol{\Delta}_k = \begin{pmatrix}
\Delta_{\sigma_1\sigma_1'}(\tau_1 - \tau_1') & \Delta_{\sigma_1\sigma_2'}(\tau_1 - \tau_2') & ... & \Delta_{\sigma_1\sigma_k'}(\tau_1 - \tau_k') \\
\Delta_{\sigma_2\sigma_1'}(\tau_2 - \tau_1') & \Delta_{\sigma_2\sigma_2'}(\tau_2 - \tau_2') & ... & \Delta_{\sigma_2\sigma_k'}(\tau_2 - \tau_k') \\
... & ... & ... & ... \\
\Delta_{\sigma_k\sigma_1'}(\tau_k - \tau_1') & \Delta_{\sigma_k\sigma_2'}(\tau_k - \tau_2') & ... & \Delta_{\sigma_k\sigma_k'}(\tau_k - \tau_k')
\end{pmatrix}
\tag{3.100}
$$

and the t^2 has been absorbed into what will have the physical meaning of the hybridization function in the effective impurity problem

$$
\Delta_{\sigma\sigma'}(\tau) = t^2\, G_{\sigma\sigma'}(\tau)
\tag{3.101}
$$

See Fig. 3.8 and Fig. 3.9.

As the Hamiltonian does not mix spins, we know $G_{\sigma\sigma'} = \delta_{\sigma\sigma'} G_\sigma$. However, this is not a restriction - a DMFT treatment of Hamiltonians including spin-orbit interaction is possible, and in that case, the Green's function is not spin diagonal. Otherwise, furher simplification of the above expressions is possible. As $\Delta_{\sigma\sigma'} = \delta_{\sigma\sigma'}\Delta_\sigma$, the matrix $\boldsymbol{\Delta}$ can always be rearranged in the block diagonal form with two blocks corresponding to spin up and down (the blocks need not be of the same size). Then, the total determinant is

$$
\det \boldsymbol{\Delta} = \det \boldsymbol{\Delta}_\uparrow \det \boldsymbol{\Delta}_\downarrow
\tag{3.102}
$$

and one can deal with the two matrices separately. Also, on the Bethe lattice, the antiferromagnetism is not frustrated, and one may even look for solutions where $G_\sigma \neq G_{\bar{\sigma}}$.

Note that the expression Eq. 3.99 is formally identical to what one obtains by performing the hybridization expansion of a single-site impurity model in which the
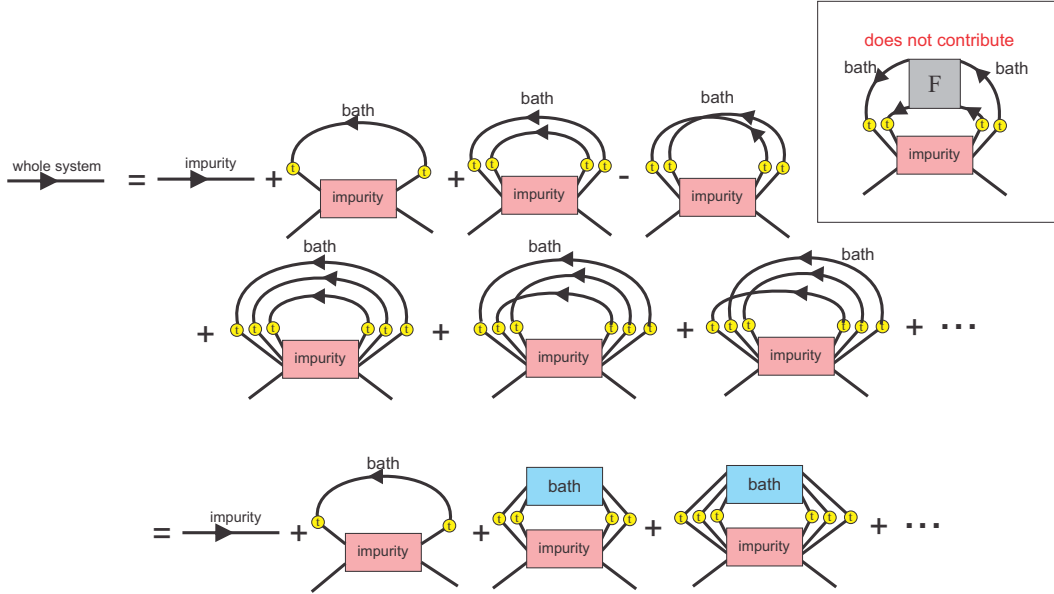
Figure 3.9: The hybridization expansion is the sum of all "crab jumping rope" diagrams.

bath is non-interacting. In this case, the hybridization part of the Hamiltonian can always be rewritten in terms of the eigenstates m of the Hamiltonian b, and the hybridization function is just

$$\Delta(\tau) = \sum_m |V_m|^2 \, G_m(\tau) \tag{3.103}$$

where the non-interacting Green's function depends only on the energy of the state m and can be obtained by Fourier transformation of the general expression

$$G_m(i\omega) = \frac{1}{i\omega - \varepsilon_m} \tag{3.104}$$

Having this in mind, after switching to the path-integral formalism, the Taylor series can be unrolled back up into the exponent. Due to the linked cluster theorem

$$1 + \sum (\text{all diagrams}) = \exp(\sum \text{connected diagrams}) \tag{3.105}$$

all the higher order terms drop out as they are necessarily disconnected (no vertices can appear). This yields a much more compact and elegant statement of DMFT

Given the local single-particle propagator of the entire lattice, the action of the

Hubbard model can be expressed as that of an interacting impurity coupled to a non-interacting bath

$$
\begin{aligned}
S \;=\; & \sum_\sigma \int d\tau \, d\tau' \; \bar{d}_\sigma(\tau) \left(\delta_{\tau,\tau'}(\partial_\tau - \mu) - \Delta_\sigma(\tau - \tau') \right) d_\sigma(\tau') \\
& + U \int d\tau \bar{d}_\uparrow(\tau) \bar{d}_\downarrow(\tau) d_\downarrow(\tau) d_\uparrow(\tau)
\end{aligned}
\tag{3.106}
$$

Solving this impurity problem for the local Green's function self-consistently such that Eq. 3.101 is achieved is equivalent to solving the Hubbard model on a $d = \infty$ Bethe lattice exactly.

The prescription for the solution of DMFT then goes as follows

1. start with an initial guess for the hybridization function $\Delta_\sigma(i\omega)$

2. solve for the local impurity Green's function $G_\sigma(i\omega)$ in the problem of an interacting single-site impurity coupled to a non-interacting bath determined by $\Delta_\sigma(i\omega)$

3. calculate a new hybridization function using $\Delta_\sigma(i\omega) = t^2 G_\sigma(i\omega)$

4. repeat 2-3 until the calculation converges.

This method of solving self-consistent equations is known as the forward recursion. There are, however, more sofisticated methods which yield the solution in fewer iterations (Broyden root finding algorithm, Conjugate gradient method) and also in cases where forward recursion fails completely (phase space extension method can converge a solution in the vicinity of a critical point and can even converge unstable solutions). In the work presented in this thesis, forward recursion and sometimes Broyden root finding are used.

Note that DMFT as an exact solution is *not* specific to the Bethe lattice, and can be derived even for the general $d = \infty$ translatory symmetric lattice, although the derivation is a bit more involved, and the connection between the hybridization function and the local Green's function of the lattice is less simple.

3.3.2.2 General translatory symmetric $d = \infty$ lattice

On a general translatory symmetric lattice, taking out one lattice site does not disconnect the rest of the lattice, so already in the first order diagrams, we need

to take into account both the local and the intersite Green's functions, i.e. G_{ij}^b's may not be immediately discarded. However, intersite propagators still go to zero in the $d = \infty$ limit, and we first need to evaluate the order of contribution of the single-particle terms. On the cubic lattice, the Manhattan distance between the nearest neighbors of site 0 through the bath is either 2 or 4, but note that for each site i, there is only one site $j(i)$ such that $|i - j| = 4$ and that is the site which is opposite of i with respect to site 0. Note also, that there are $\sim d$ nearest neighbors to each site.

$$
\begin{aligned}
\frac{t^2}{d} \sum_{ij} G_{ij}^b &= \frac{t^2}{d} \left(\sum_{ij, i \neq j, j(i)} G_{ij}^b + \sum_i G_{ii}^b + \sum_i G_{ij(i)}^b \right) \qquad (3.107) \\
&\sim \frac{t^2}{d} \left(d^2 \left(\frac{1}{\sqrt{d}} \right)^2 + d + d \left(\frac{1}{\sqrt{d}} \right)^4 \right) \sim 1
\end{aligned}
$$

We see, that although not all intersite propagators contribute, most of them do so we keep this expression as is, for now. Note also, that $G_{ij}^b \neq G_{ij}$. The bath part of the system is not even translationally symmetric because it is missing the site at $\mathbf{r} = 0$. However, the rotational symmetry in all planes around $\mathbf{r} = 0$ is preserved, so all the pairs ij such that $|i - j| = 2$ are equivalent, so there must be only one distinct G_{ij}^b that contributes to the above expression.

We now turn to the second order terms. As before, the full two-particle propagator can be expressed with the Bethe-Sapleter equation. However, all the neighbors of site 0 belong now to the same sublattice, so the full vertex F is never immediately zero. In infinite dimensions, however, it is still always local. That means that if $i \neq j \neq k \neq l$, we need to bring both particles to the same site before they can interact. To place an interaction vertex in a diagram of the interaction expansion of G_{ijkl}^b, it would have to bring in at least a factor of $(1/\sqrt{d})^{|i-j|+|k-i|+|i-l|}$, as can be seen from Fig. 3.7, and we know that $|i - j| \geq 2, \forall i, j$.

$$
\begin{aligned}
\frac{t^4}{d^2} \sum_{ijkl, i \neq j \neq k \neq l} G_{ijkl}^b &= \frac{t^4}{d^2} \sum_{ijkl, i \neq j \neq k \neq l} \left(G_{ij}^b G_{kl}^b - G_{il}^b G_{kj}^b + G_{ii}^b G_{ki}^b F_{iiii}^b G_{ij}^b G_{il}^b + ... \right) \\
&\lesssim \frac{1}{d^2} \left(d^4 \left(\frac{1}{\sqrt{d}} \right)^4 + d^4 \left(\frac{1}{\sqrt{d}} \right)^6 \right) \sim 1 + \frac{1}{d} \sim 1 + 0 \quad (3.108)
\end{aligned}
$$

As a counter example, G_{iiij}^b needs to bring only $(1/\sqrt{d})^{|i-j|}$, but here we lose two

sums

$$\frac{t^4}{d^2} \sum_{ij, i \neq j} G_{ii}^b G_{ii}^b F_{iiii}^b G_{ii}^b G_{ij}^b \gtrsim \frac{1}{d^2} \, d^2 \left(\frac{1}{\sqrt{d}} \right)^2 \sim \frac{1}{d} \sim 0$$

It is clear now that even for the arbitrary translatory symmetric $d = \infty$ lattice, vertices play no role, and that $\hat{H}_b$ part of the Hubbard model is in Eq. 3.86 effectively non-interacting. The Taylor expansion can again be rolled back to obtain the effective action of the Hubbard hubbard model, but now the effective Hybridization function is given by

$$\Delta_\sigma(\tau) = t^2 \sum_{ij} G_{ij\,\sigma}^b(\tau) \tag{3.109}$$

and $G_{ij}^b(\tau)$ is not yet known - we need to relate it to the local Green's function of the whole lattice for the method to be practical.

First we note that since the bath is effectively non interacting, the following expansion is possible, for any i and j (Fig. 3.10)
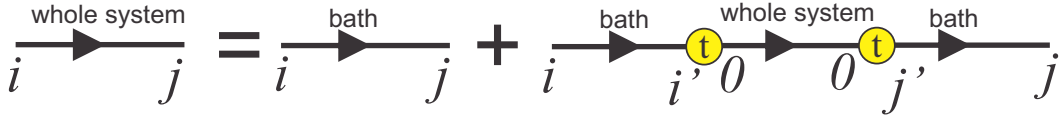
Figure 3.10: On going from i to j sites, an electron can either avoid the site 0, or go over it any number of times.

$$G_{ij} = G_{ij}^b + G_{ii'}^b \, t \, G_{00} \, t \, G_{j'j}^b \tag{3.110}$$

The summation over nearest neighbors of site 0 (i', j') and integration over internal times is implicit. The integration over times makes Eq. 3.110 a coupled system of equations, where each equation corresponds to a different time τ on the lefthand side. However, if Fourier transformed, energy conservation can be used to decouple the equations for each Matsubara frequency. In the following, all quantities are assumed to be at the same frequency. Note that there are no further terms with $t^4, t^6, ...$ because going away from site 0 and comming back to it arbitrary number of times is already included in G_{00}. We also know

$$G_{i0} = G_{ii'}^b \, t \, G_{00} \tag{3.111}$$

and therefore

$$G_{ij}^b = G_{ij} - \frac{G_{i0}G_{0j}}{G_{00}}. \tag{3.112}$$

We will now use this to relate G_{00} with G_{ij}^b. In a homogeneous solution, $G_{00} = G$.

The effective Hybridization function is given by

$$\Delta = t^2 \sum_{ij} G_{ij}^b = t^2 \sum_{ij} \left(G_{ij} - \frac{G_{i0}G_{0j}}{G} \right) \tag{3.113}$$

Now we take into account

$$G_{ij} = \sum_{\mathbf{k}} e^{i\mathbf{k}\cdot(\mathbf{r}_i - \mathbf{r}_j)} G_{\mathbf{k}}$$

and obtain:

$$\Delta = t^2 \sum_{ij} \left(\sum_{\mathbf{k}} e^{i\mathbf{k}\cdot(\mathbf{r}_i - \mathbf{r}_j)} G_{\mathbf{k}} - \frac{\sum_{\mathbf{k}} e^{i\mathbf{k}\cdot(\mathbf{r}_i - \mathbf{r}_0)} G_{\mathbf{k}} \sum_{\mathbf{k}'} e^{i\mathbf{k}'\cdot(\mathbf{r}_0 - \mathbf{r}_j)} G_{\mathbf{k}'}}{G} \right) \tag{3.114}$$

$$\Delta = \sum_{\mathbf{k}} G_{\mathbf{k}} \sum_i t e^{i\mathbf{k}\cdot\mathbf{r}_i} \sum_j t e^{-i\mathbf{k}\cdot\mathbf{r}_j} - \frac{\sum_{\mathbf{k}} G_{\mathbf{k}} \sum_i t e^{i\mathbf{k}\cdot(\mathbf{r}_i - \mathbf{r}_0)} \sum_{\mathbf{k}'} G_{\mathbf{k}'} \sum_j t e^{\mathbf{k}'\cdot(\mathbf{r}_0 - \mathbf{r}_j)}}{G} \tag{3.115}$$

Furthermore, we know the general expression for the electron dispersion

$$\varepsilon_{\mathbf{k}} = \sum_j t_{ij}\, e^{i\mathbf{k}\cdot(\mathbf{r}_i - \mathbf{r}_j)}$$

In this expression, j goes over *all* sites of the lattice. However, in our Eq. 3.113, i and j go over only the nearest neighbors of site 0. Still, we can use the above identity since in our model t_{0j} for all sites j except the nearest neighbors of site 0 is 0, and otherwise it is t. Furthermore $\mathbf{r}_0 = 0$. We obtain

$$\Delta = \sum_{\mathbf{k}} \varepsilon_{\mathbf{k}}^2 G_{\mathbf{k}} - \frac{(\sum_{\mathbf{k}} \varepsilon_{\mathbf{k}} G_{\mathbf{k}})^2}{G} \tag{3.116}$$

We can now evaluate the **k**-sums:

$$\sum_{\mathbf{k}} \varepsilon_{\mathbf{k}} G_{\mathbf{k}} = \sum_{\mathbf{k}} \frac{\varepsilon_{\mathbf{k}}^2}{i\omega_n + \mu - \varepsilon_{\vec{\mathbf{k}}} - \Sigma(i\omega)} = \sum_{\mathbf{k}} \frac{\varepsilon_{\mathbf{k}} - \xi + \xi}{\xi - \varepsilon_{\vec{\mathbf{k}}}} = -1 + \xi \sum_{\mathbf{k}} G_{\mathbf{k}} = -1 + \xi G_{00} \tag{3.117}$$

Here we have introduced a notational shortcut $\xi = i\omega + \mu - \Sigma(i\omega)$ and we used the locality of self-energy to pull ξ out of the sum.

$$\sum_{\mathbf{k}} \varepsilon_{\mathbf{k}}^2 G_{\mathbf{k}} = \sum_{\mathbf{k}} \frac{\varepsilon_{\mathbf{k}}(\varepsilon_{\mathbf{k}} - \xi) + \varepsilon_{\mathbf{k}}\xi}{\xi - \varepsilon_{\vec{\mathbf{k}}}} = -\sum_{\mathbf{k}} \varepsilon_{\mathbf{k}} + \xi \sum_{\mathbf{k}} \varepsilon_{\mathbf{k}} G_{\mathbf{k}} \tag{3.118}$$

The first term is explicitly 0 and the other term we have already evaluated:

$$\sum_{\mathbf{k}} \varepsilon_{\mathbf{k}}^2 G_{\mathbf{k}} = \xi(-1 + \xi G) = -\xi + \xi^2 G \tag{3.119}$$

Plugging these back into the previous equation yields:

$$\begin{aligned} \Delta &= -\xi + \xi^2 G - \frac{(-1 + \xi G)^2}{G} \tag{3.120} \\ &= -\xi + \xi^2 G - \frac{1 + \xi^2 G^2 - 2\xi G}{G} \\ &= -\xi + \xi^2 G - G^{-1} - \xi^2 G + 2\xi \end{aligned}$$

and finally

$$\Delta = i\omega + \mu - \Sigma - G^{-1} \tag{3.121}$$

As we see, the relation between Δ and the local Green's function of the whole lattice now involves also the (local) self-energy of the whole lattice. To fix all three quantities (G, Σ and Δ) in the self-consistent calculation, we need another equation - the one that connects the lattice Green's function with the lattice self-energy

$$G(i\omega) = \int d\varepsilon \frac{\rho(\epsilon)}{i\omega + \mu - \varepsilon - \Sigma(i\omega)} \tag{3.122}$$

where $\rho(\epsilon)$ is the non-interacting density of states of the whole lattice. Note that the above expression and Eq. 3.121 are both completely general and can also be used in the case of the Bethe lattice. The prescription for solution of DMFT by forward recursion goes as follows

1. start with an initial guess for the hybridization function $\Delta_\sigma(i\omega)$

2. solve for the local impurity Green's function $G_\sigma(i\omega)$ (and/or self-energy $\Sigma_\sigma(i\omega)$) in the problem of an interacting single-site impurity coupled to a non-interacting bath determined by $\Delta_\sigma(i\omega)$

3. if only $G_\sigma(i\omega)$ is known, calculate $\Sigma_\sigma(i\omega)$ from $\Sigma = i\omega + \mu - \Delta - G^{-1}$. Otherwise, skip this step.

4. calculate the new lattice Green's function from self-energy using $G_{new}(i\omega) = \int d\varepsilon\, \rho(\epsilon)\, (i\omega + \mu - \varepsilon - \Sigma(i\omega))^{-1}$

5. calculate a new hybridization function using $\Delta = i\omega + \mu - \Sigma - G_{new}^{-1}$

6. repeat 2-5 until the calculation converges.

Note that the Eq. 3.121 can be derived with much less effort by relating the hybridization function with the impurity Green's function and self-energy. As we shall see in the next section, the equation obtained is identical to Eq. 3.121 and since the self-consistency requires that both the local Green's function and self-energy on the impurity are the same as everywhere else on the lattice, we need not consider the connection between the lattice Green's function, lattice self-energy and hybridization function on general grounds at all, and so the derivation from Eq. 3.110 to Eq. 3.121 is unnecessary.

3.3.3 Interaction expansion of the effective impurity model

Now that we have shown that the bath is effectively non-interacting, some further considerations can be made. We first split the atomic part of the Hamiltonian into noninteracting and purely interacting parts

$$\hat{H} = \hat{H}_a^0 + \hat{H}_a^i + \hat{H}_b + \hat{H}_{hyb} \tag{3.123}$$

$$\hat{H}_a^0 = -\mu \sum_\sigma n_{0\sigma} \tag{3.124}$$

$$\hat{H}_a^i = U n_{0\uparrow} n_{0\downarrow} \tag{3.125}$$

The Green's function calculated at the impurity with respect to only $\hat{H}_a^0$ is then simply

$$G_0^a = \frac{1}{i\omega + \mu} \tag{3.126}$$

Because the bath is effectively non-interacting, the local single-particle propagator $\mathcal{G}_0$ calculated at the impurity site with respect to $\hat{H}_a^0 + \hat{H}_b + \hat{H}_{hyb}$ can be expanded
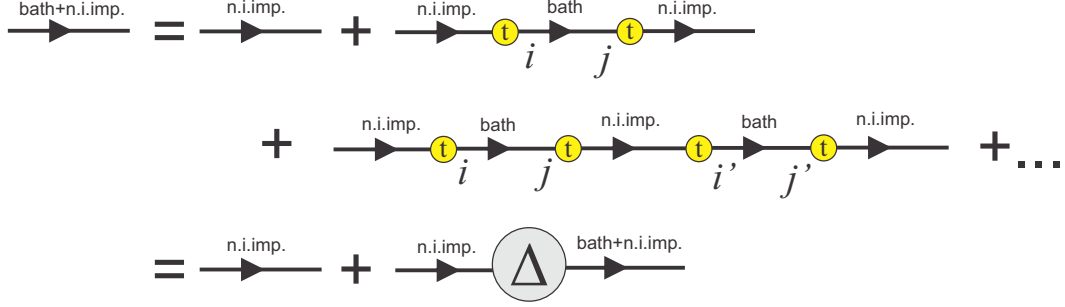
Figure 3.11: When the interaction on the impurity is turned off, the hybridization expansion becomes very simple.

in terms of $\hat{H}_{hyb}$ much more simply (Fig. 3.11)

$$
\begin{aligned}
\mathcal{G}_0 &= G_0^a + G_0^a \, t \, G_{ij}^b \, t \, G_0^a + G_0^a \, t \, G_{ij}^b \, t \, G_0^a \, t \, G_{i'j'}^b \, t \, G_0^a + ... \\
&= G_0^a + G_0^a \, t \, G_{ij}^b \, t \, \left(G_0^a + G_0^a \, t \, G_{i'j'}^b \, t \, G_0^a + ... \right) \\
&= G_0^a + G_0^a \, t \, G_{ij}^b \, t \, \mathcal{G}_0
\end{aligned}
\tag{3.127}
$$

where summation over site indices is again implicit. Now we write it explicitly

$$
(G_0^a)^{-1} = \mathcal{G}_0^{-1} + t^2 \sum_{ij} G_{ij}^b
\tag{3.128}
$$

where we immediately recognize $\Delta = t^2 \sum_{ij} G_{ij}^b$ as the hybridization function of the impurity model. We have

$$
\mathcal{G}_0 = ((G_0^a)^{-1} - \Delta)^{-1} = \frac{1}{i\omega + \mu - \Delta}
\tag{3.129}
$$

The propagator $\mathcal{G}_0$ has the physical meaning of the Weiss field in the effective impurity problem, because it contains all the processes except the on-site interaction.

Now, the full single-particle propagator (at the impurity site) of the impurity problem can be obtained by interaction-expansion around the non-interacting part of the Hamiltonian so

$$
G = \mathcal{G}_0 + \mathcal{G}_0 \Sigma G
\tag{3.130}
$$

where Σ is assumed to be proper (irreducible), and of course

$$
\mathcal{G}_0^{-1} = G^{-1} + \Sigma
\tag{3.131}
$$

which is the well known Dyson equation. Plugging this back into Eq. 3.129, we obtain an expression formally and physically equivalent to Eq. 3.121

$$\Delta = i\omega + \mu - \Sigma - G^{-1} \tag{3.132}$$

because the G and Σ of the whole lattice must be the same as the ones on the impurity.

Now, the DMFT self-consistent equation can be restated in terms of the Weiss field. The explicit Taylor series in $\hat{H}_a^i$ yields (Fig. 3.12)

$$
\begin{aligned}
G_\sigma(\tau - \tau') \;=\; & \sum_{k=0}^{\infty} (-U)^k \int_0^\beta d\tau_1 ... \int_{\tau_{k-1}}^\beta d\tau_k \\
& \times \mathrm{Tr}\left[T_\tau e^{-\int_0^\beta (\hat{H}_a^0 + \hat{H}_b + \hat{H}_h yb)} d_\sigma^\dagger(\tau') d_\sigma(\tau) \right. \\
& \times \left. d_\uparrow^\dagger(\tau_1) d_\downarrow^\dagger(\tau_1) d_\downarrow(\tau_1) d_\uparrow(\tau_1) ... d_\uparrow^\dagger(\tau_k) d_\downarrow^\dagger(\tau_k) d_\downarrow(\tau_k) d_\uparrow(\tau_k) \right]
\end{aligned}
\tag{3.133}
$$

The many-body Green's function can be now expressed solely in terms of the local
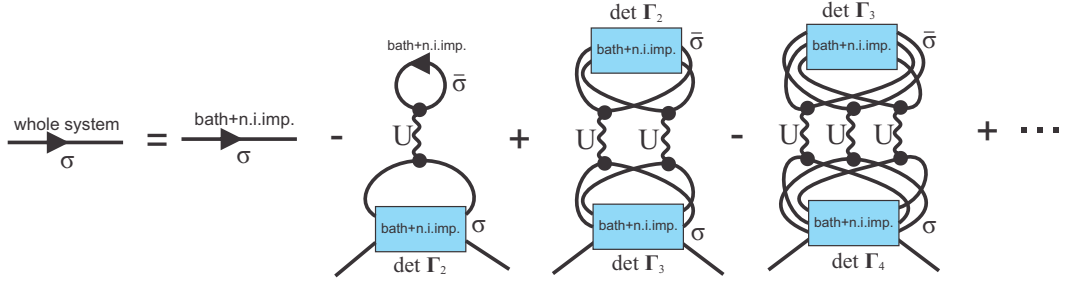
Figure 3.12: The interaction expansion series.

propagator $\mathcal{G}_0$

$$G_\sigma(\tau - \tau') \;=\; \sum_{k=0}^{\infty} (-U)^k \int_0^\beta d\tau_1 ... \int_{\tau_{k-1}}^\beta d\tau_k \, \det\boldsymbol{\Gamma}_\sigma^{k+1} \det\boldsymbol{\Gamma}_{\bar{\sigma}}^{k} \tag{3.134}$$

where

$$
\boldsymbol{\Gamma}_\sigma^k =
\begin{pmatrix}
\mathcal{G}_{0\sigma}^{-1}(0) & \mathcal{G}_{0\sigma}^{-1}(\tau_2 - \tau_1) & ... & \mathcal{G}_{0\sigma}^{-1}(\tau_k - \tau_1) \\
\mathcal{G}_{0\sigma}^{-1}(\tau_1 - \tau_2) & \mathcal{G}_{0\sigma}^{-1}(0) & ... & \mathcal{G}_{0\sigma}^{-1}(\tau_k - \tau_2) \\
... & ... & ... & ... \\
\mathcal{G}_{0\sigma}^{-1}(\tau_1 - \tau_k) & \mathcal{G}_{0\sigma}^{-1}(\tau_2 - \tau_k) & ... & \mathcal{G}_{0\sigma}^{-1}(0)
\end{pmatrix}
\tag{3.135}
$$

and the extra two operators are absorbed as an extra row and column in the matrix $\boldsymbol{\Gamma}$ of corresponding spin.

This equation is, however, not practical as even and odd orders k will have a different sign, and a naive summation of this series would lead to a serious sign problem. However, this can be resolved easily by performing a simple transformation of the d operators. Further discussion on how to do stochastic summation of interaction expansion diagrams can be found elsewhere and is of no relevance for the results presented in this thesis.

Note also, that the summation in Eq. 3.134 includes *all* the diagrams, including the disconected and reducible ones. One can of course restrict to only connected and proper self-energy diagrams, in which case the algorithm is called the diagrammatic quantum monte-carlo.

3.4 Solution of the effective impurity model

Identifying the solution of the Hubbard model with the solution of an impurity model with a self-consistently determined hybridization function is only the first step. Solving the impurity model in itself is still not easy, and there is a variety of numerical methods which aproach this problem in different ways. First, the starting point of the approach can be either the hybridization expansion from Eq. 3.99 or the interaction expansion in Eq. 3.134. Then, a number of approximations may be utilized. Either the series of diagrams is cut off at some order (perturbation theory) [50, 51] or only some subclasses of diagrams are summed (OCA, NCA) to all orders semi-analytically [52]. Otherwise, the bath can be approximated with a finite set of states, and then the problem can be solved by exact diagonalization of the effective Hamiltonian [53]. However, this scheme introduces the systematic error of finite system size, and is also restricted to zero temperature. If instead of exact diagonalization a renormalization group method is used (NRG, DMRG), a larger system can be treated to lessen the finite size effects, but then the solution is again not exact [54, 55]. Finally, one can use stochastic (Monte Carlo) summation of all the diagrams. These methods necessarily introduce Gaussian numerical error as calculation is always performed a finite amount of time. The simplest approach is to decouple the interaction at the impurity using a Hubbard-Stratonowich transformation, and this way reduce the book-keeping task to going over all configurations of a single 1D Ising-like field (the Hirsch-Fye method) [56]. However, this approach

suffers from an additional systematic error introduced by a finite discretization of the imaginary time coordinate. The cutting edge methods overcome this by going through all time configurations of the diagram explicitly and are therefore called the continuous-time methods [57, 58]. However, the main limitations are common to all stochastic methods - very low temperatures (of order 10^{-3} non-interacting bandwidth and lower) are inaccessible and in some cases the fermionic sign problem is prohibitive of getting meaningful results.

In the work presented in this thesis, only the hybridization-expansion continuous time quantum Monte Carlo (HYB-CTQMC) and second order perturbative impurity solvers are used. In the next two sections I review the numerical challenges arising in these methods.

3.4.1 Hybridization expansion continuous-time quantum Monte Carlo

Hybridization expansion continuous-time quantum Monte Carlo (HYB-CTQMC) carries on from Eq. 3.99 [49, 57, 58]. The problem to solve is threefold

1. how to obtain a reliable estimate of the infinite sum of diagrams?

2. how to evaluate the trace over the impurity degrees of freedom of a given diagram?

3. how to efficiently calculate the hybridization determinant and measure Green's function?

Here I deal with the three issues separately.

3.4.1.1 Stochastic summation

In Eq. 3.99, the sum over diagram orders k goes all the way to infinity, but it turns out that the diagrams of order higher than some k_{max} contribute negligibly. However, this k_{max} in practice is not small, and one needs a way to evaluate highly dimensional integrals. For a diagram of order k, the variables of the integrand are $2k$ different times and the choices of $2k$ different σ indices, altough Pauli exclusion renders most of the possible choices of $\{\sigma\}$ irrelevant.

The cutting edge tool for calculation of highly dimensional integrals is the Monte Carlo method. It relies on a stochastic, importance sampling of integration variables,

and in this context, the sampling will run over diagrams of different orders, and different configurations of the internal degrees of freedom of the diagrams ($\{\tau\}$ and $\{\sigma\}$).

We start with some general considerations. Say we want to calculate an integral of the form

$$a = \int A(x)dx \tag{3.136}$$

and that the function A can be calculated as a product of two other functions

$$A(x) = B(x)p(x) \tag{3.137}$$

so we have

$$a = \int B(x)p(x)dx \tag{3.138}$$

The variable x may be a vector of arbitrary dimension and in present context I will refer to it as 'configuration'. Now it is enough to perform the random sampling such that any configuration x is visited at a rate proportional to $p(x)$ (i.e. perform importance sampling with respect to $p(x)$), and then we have

$$a = \langle B(x) \rangle_{MC} \tag{3.139}$$

When we do the Monte Carlo average - we only sum the B quantity, and the weight $p(x)$ is automatically included.

In our problem, the configuration x corresponds to a vector $(k, \{\tau\}, \{\sigma\})$ and the function A is the Green's function

$$\langle T_\tau d_\sigma(\tau') d_\sigma^\dagger(\tau) \rangle = \frac{1}{Z} \mathrm{Tr} \left[T_\tau d_\sigma(\tau') d_\sigma^\dagger(\tau) \, e^{- \int_0^\beta d\tau \hat{H}(\tau)} \right] \tag{3.140}$$

It is immediately clear that if one were to calculate the Green's function straightforwardly, the integral would have to be performed many times, for each value of $\tau' - \tau$, and this is not very efficient. The way to perform the measurement of the Green's function is to pick two operators from the existing ones, and "cut" the hybridization line that connects them - i.e. remove the corresponding row and column in Δ. The measure of Green's function at a given configuration is then

$$G_{\sigma_i \sigma_j'}(x; \; \tau_j' - \tau_i) = \mathrm{Tr}_d[T_\tau \, e^{- \int_0^\beta d\tau \hat{H}(\tau)}] \det \boldsymbol{\Delta}^{(i,j)} = \frac{\det \boldsymbol{\Delta}^{(i,j)}}{\det \boldsymbol{\Delta}} Z(x) \tag{3.141}$$

where $\mathbf{\Delta}^{(i,j)}$ is the matrix $\mathbf{\Delta}$ with row i and column j removed, and $Z(x) = \text{Tr}_d[...] \det \mathbf{\Delta}$ is the weight of partition function in the current configuration. This means that one constructs only the bubble (partition function) diagrams $Z(x)$, and as the order of diagram is typically large, one can perform many measurements of the Green's function at various τ's from each configuration x. If the importance sampling is performed with respect to $Z(x)$ (which we have already calculated by the time configuration x has been accepted) we have

$$G_\sigma(\tau) = \langle \frac{\det \mathbf{\Delta}^{(i,j)}}{\det \mathbf{\Delta}} \rangle_{MC} \tag{3.142}$$

where i and j are chosen in each measurement such that $\sigma_i = \sigma'_j = \sigma$ and $\tau'_j - \tau_i = \tau$. So, we only need to calculate the ratio between determinants, which we are able to do rather efficiently (see section 3.4.1.3 for a detailed discussion on the measurement of the Green's function).

However, for this calculation to work, we need to ensure that any configuration x will be visited at precisely the rate of $Z(x)$. This can be done by employing an algorithm of stochastic sampling of configurations such that two criteria are satisfied

- ergodicity - any configuration must be reachable from any other configuration in a finite number of steps

- stationarity (or global balance) - the probability to go from any configuration y to configuration x in one step is in total $Z(x)$

$$\int dy \, W_{yx} = Z(x) \tag{3.143}$$

The array of configurations visited is referred to as the Markov chain. For the Markov chain to satisfiy ergodicity, in our case it is enough to update the configuration in each step by

- adding pairs of operators ($d_\sigma^\dagger$ and d_σ) at random times

- removing random pairs of operators ($d_\sigma^\dagger$ and d_σ)

However, it is of practical value to sometimes also

- shift times of randomly chosen operators

- exchange all the $\uparrow$ and $\downarrow$ operators

as these updates reduce the auto-correlation time.

As for the global balance - it can be satisfied in various ways. Because of relative simplicity, in practice one satisfies the detailed balance criterion although it is a stronger requirement than actually needed (i.e. stronger than global balance). The detailed balance requires

$$\frac{W_{xy}}{W_{yx}} = \frac{p(y)}{p(x)} \tag{3.144}$$

where x and y are different configurations, W_{xy} is the probability to go from x to y, and $p(x)$ is the weight of a given configuration (in our case $p(x) = \text{Tr}_d[...]\det\mathbf{\Delta} = Z(x)$). Note also that

$$W_{xy} = W_{xy}^{prop} W_{xy}^{acc} \tag{3.145}$$

i.e. the probability to go from x to y is probability to propose y while at x, times the probability to accept y while at x (once y is proposed). The detailed balance is satisfied when the acceptance of a configuration to the Markov chain is always decided by the Metropolis algorithm. The proposed update is accepted if a random number $r \in [0, 1)$ is lower than the acceptance ratio

$$R_{xy} = \min\left[\frac{p(y)}{p(x)}\frac{W_{yx}^{prop}}{W_{xy}^{prop}}, 1\right] \tag{3.146}$$

Now we need to determine $\frac{W_{xy}^{prop}}{W_{yx}^{prop}}$ for all types of updates. For the time shift update, we first choose one of the $2k$ times (i) and then determine to operator of what spin this time corresponds. Then, the maximal shift to both earlier and later times is determined by the times of previous (τ_{min}) and next (τ_{max}) operators of the same spin. Therefore, we need to choose a random time τ between τ_{min} and τ_{max} and perform the shift $\tau_i \rightarrow \tau$ (while respecting the cyclic nature of the time coordinate). The probability to propose this new configuration is determined by the number of operators (times) k and the range of available times $\tau_{max} - \tau_{min}$, so we have

$$W_{xy}^{prop} = \frac{1}{2k(\tau_{max} - \tau_{min})}.$$

The probability to go from the new state back to the old state is just the same as it was to go from the old to the new one. So, the time-shift update is self-balancing,

i.e. $\frac{W_{yx}^{prop}}{W_{xy}^{prop}} = 1$, and the acceptance ratio for the shift update is given by

$$R_{xy}^{shift} = \min\left[\frac{p_{new}}{p_{old}}, 1\right].$$ (3.147)

The same holds for the global update of exchanging all ↑ and ↓ operators.

For the addition of two operators, the situation is more complicated. When we add two operators, we first choose the spin (probability 1/2), choose one random time ($1/\beta$) and then another in range ($\tau_{max} - \tau_{min}$) (which one of the two times will correspond to the creation operator is determined by whether the next of the old operators is creation or annihilation operator) in total $\frac{1}{2\beta(\tau_{max}-\tau_{min})}$. But to return to the original state, we need to remove two operators. This we do by choosing spin σ (probabaility 1/2), and then choosing one annihilation operator out of $k_\sigma/2$ operators, and then choosing the creation operator of the same spin that is either the first after or the first before the chosen annihilation operator (k_σ is one larger then k_σ of the original state, so the total probability is $\frac{1}{4(k_\sigma+1)}$). For the addition of two operators we have

$$R_{xy}^{add,\sigma} = \min\left[\frac{p_{new}}{p_{old}}\frac{\beta(\tau_{max}-\tau_{min})}{2(k_\sigma+1)}, 1\right]$$ (3.148)

Analogous consideration leads to the acceptance ratio for removal of two operators of spin σ

$$R_{xy}^{rmv,\sigma} = \min\left[\frac{p_{new}}{p_{old}}\frac{2k_\sigma}{\beta(\tau_{max}-\tau_{min})}, 1\right]$$ (3.149)

Now it is easy to see that as long as $k_\sigma \ll \beta$, addition of two σ operators will most likely be accepted. The same holds for the removal of two operators when $k_\sigma \gg \beta$. That means that the typical order k of the diagram visited in the simulation will be proportional to β - the larger the compactification radius of the imaginary time, the more creation/annihilation events will typically appear in the time evolution. This means that there is some preferred "density" of the d operators, or in other words, there is a time scale of order 1 which sets the average time distance between two operators. This scale, however, is determined by the amount of interaction on the impurity sites - the higher the order of the diagram, the more fermions appear in the time evolution thus experiencing more interaction. In practice, the histogram of k in the CTQMC is sharply peaked around $N_{flavors}\beta E_{kin}$ where E_{kin} is the total kinetic energy.

3.4.1.2 Evaluation of the trace

In the case of a single-site impurity (we can have more then one orbital as long as they are orthogonal, i.e. there are no hoppings between the orbitals (flavors)), and in the absence of off-diagonal interactions (such as Hund's coupling), the atomic Hamiltonian H_a commutes with the density operators, and is diagonal in the Fock basis. This allows for a silmple and direct estimation of the trace $\text{Tr}_d[...]$. For the sake of simplicity, we restrict here to the single-orbital case. We insert 2 unit decompositions around each d operator and obtain

$$
\begin{aligned}
& \text{Tr}_d \left[T_\tau \, e^{-\int_0^\beta d\tau \hat{H}_a} d^\dagger_{\sigma_1}(\tau_1)...d^\dagger_{\sigma_k}(\tau_k) d_{\sigma'_1}(\tau'_1)...d_{\sigma'_k}(\tau'_k) \right] \\
= \quad & s_P \sum_{n,n_1,n_2...n_{4k}} \langle n | e^{-(\beta-\tau_{2k})\hat{H}_a} | n_{4k} \rangle \\
& \times \langle n_{4k} | d^{(X_{2k})}_{\sigma_{2k}} | n_{4k-1} \rangle \langle n_{4k-1} | e^{-(\tau_{2k}-\tau_{2k-1})\hat{H}_a} | n_{4k-2} \rangle ... \\
& \times ... \langle n_2 | d^{(X_1)}_{\sigma_1} | n_1 \rangle \langle n_1 | e^{-\tau_1 \hat{H}_{loc}} | n \rangle
\end{aligned}
\tag{3.150}
$$

where we have applied the time order operator first, and then relabeled the times (and the σ indices) so that they appear in order. The sign s_P comes from the permutation of the operators needed to establish the time order. X_i is either $\dagger$ or 1, depending on the choice of original τ_i's and τ'_i's. The many-body states $|n\rangle$ run over the Fock basis. Since the Hamiltonian H_{loc} is diagonal in the Fock basis we have $\langle n | e^{-\Delta\tau \hat{H}_a} | m \rangle = \delta_{|n\rangle,|m\rangle} e^{-\Delta\tau E_n}$, where E_n is the energy of the many-body state $|n\rangle$. This reduces the number of sums so we have

$$
s_P \sum_{n,n_1,n_2...n_{2k-1}} e^{-(\beta-\tau_{2k})E_n} \langle n | d^{(X_{2k})}_{\sigma_{2k}} | n_{2k-1} \rangle e^{-(\tau_{2k}-\tau_{2k-1})E_{n_{2k}}} ... \langle n_1 | d^{(X_1)}_{\sigma_1} | n \rangle e^{-\tau_1 E_n}
$$

Also, we know that for each creation(annihilation) operator $\langle n | d^\dagger_\sigma | m \rangle = \delta_{|n\rangle, d^\dagger_\sigma | m \rangle}$ must hold, there can be only one sequence of states $|n_i\rangle$ that accomodates the given order of d operators, i.e. all the sums vanish. Since $H_a = -\mu \sum_\sigma n_\sigma + U n_\uparrow n_\downarrow$

$$
\text{Tr}_d[...] = s_P \, e^{\mu \sum_\sigma L_\sigma - U\mathcal{O}}
\tag{3.151}
$$

where L_σ is the total time the spin-state σ is occupied, and $\mathcal{O}$ is the total time both $\uparrow$ and $\downarrow$ are occupied. See Fig. 3.13. Note also that nothing must depend on the
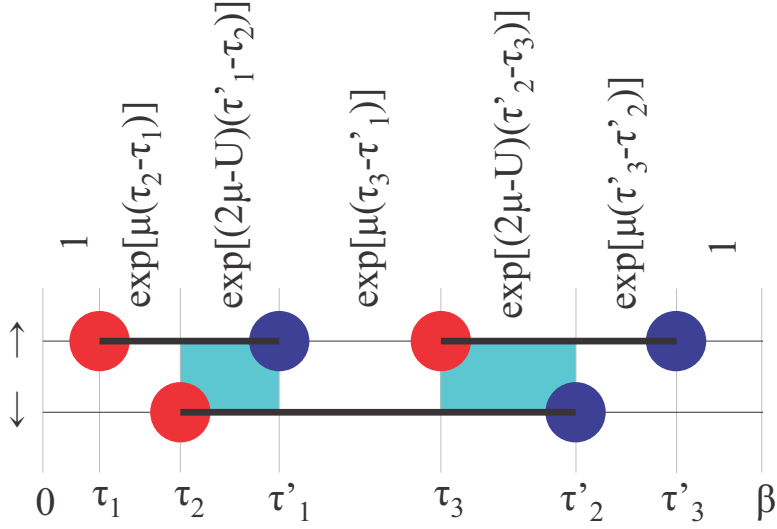
Figure 3.13: When the local Hamiltonian is diagonal in the Fock basis (as is the case in the single-site impurity problem), one can easily evaluate the contribution of a given configuration. The illustration shows an example of a $k = 3$ configuration, and the contribution of individual time segments. The larger the overlap (light blue), the smaller the contribution of the configuration.

particular times - the contribution of the diagram must remain unchanged if all the operators are shifted the same amount of time. Because of this, one may keep one operator at a fixed time (say, 0) and not keep track of the sign s_P at all. If we shift all the operators so that the first one becomes the last one, we have performed an odd number of permutations (because of the particle number conservation, the number of operators of the same spin is *always* even, and so is the total number of operators) and the overall trace changes sign. However, the same happens with all the hybridization lines connected to this operator, and therefore the change in sign is cancelled by the change in sign of $\det \Delta$.

3.4.1.3   Quick update of $\det \mathbf{\Delta}$

To evaluate the probability R for accepting an update of a configuration (which must be done in each MC step, and the total number of steps in each solution of the impurity problem is of the order of 10^9), one must calculate the determinant of a $k \times k$ matrix $\mathbf{\Delta}_k$. As k can be very large (of the order of 1000), and the calculation of determinant is a $O(k^3)$ operation, it is extremely important to optimize this procedure. Luckily, the matrix $\mathbf{\Delta}_k$ does not change much when an update is made, and one can make use of Shermann-Morisson formula to update the determinant in

$O(k)$ steps.

Note that in the case there is not mixing of spins $\Delta_{\sigma\sigma'} = \delta_{\sigma\sigma'}\Delta_\sigma$, the matrix $\mathbf{\Delta}$ can always be rearranged in the block diagonal form such that

$$\det\mathbf{\Delta} = \det\mathbf{\Delta}_\uparrow \det\mathbf{\Delta}_\downarrow \tag{3.152}$$

and one can deal with the two matrices separately. For the sake of completness, I present here the derivation for the general case.

First, it is much more convenient to store (and manipulate) the matrix inverse of $\mathbf{\Delta}$

$$\mathbf{M} = \mathbf{\Delta}^{-1} \tag{3.153}$$

When two operators are added, $\mathbf{\Delta}$ grows in size by one - i.e. one row and one column are added. The new elements are

$$\begin{aligned}
\Delta_{k+1,l} &= \Delta_{\sigma_{k+1}\sigma'_l}(\tau'_l - \tau_{k+1}) \\
\Delta_{l,k+1} &= \Delta_{\sigma_l\sigma'_{k+1}}(\tau'_{k+1} - \tau_l) \\
\Delta_{k+1,k+1} &= \Delta_{\sigma_{k+1},\sigma'_{k+1}}(\tau'_{k+1} - \tau_{k+1})
\end{aligned} \tag{3.154}$$

where l runs over the old internal degrees of freedom, and $k+1$ are the added σ's and τ's. $\Delta_{\sigma\sigma'}(\tau)$ is the hybridization function. We now define two vectors of size $k+1$ ($\vec{L}$ and $\vec{R}$) and two scalars (p and q) that depend on the old (stored) $\mathbf{M}$ matrix, and the added elements of $\mathbf{\Delta}$

$$\begin{aligned}
L_i &= \begin{cases} \sum_l M_{il}\Delta_{l,k+1}, & i < k+1 \\ -1, & i = k+1 \end{cases} \\
R_i &= \begin{cases} \sum_l \Delta_{k+1,l}M_{li}, & i < k+1 \\ -1, & i = k+1 \end{cases} \\
q &= \sum_{l<k+1} \Delta_{k+1,l}L_l \\
p &= \left(\Delta_{k+1,k+1} - q\right)^{-1}
\end{aligned} \tag{3.155}$$

Now, the new (enlarged) matrix $\mathbf{M}$ can be obtained by first expanding it with zeros

$$\tilde{M}_{ij} = \begin{cases} M_{ij}, & i < k+1 \wedge j < k+1 \\ 0, & \text{otherwise} \end{cases} \tag{3.156}$$

70

and then applying the Sherman-Morrison formula directly yields

$$\mathbf{M}^{new} = \tilde{\mathbf{M}} + p\,\vec{L} \otimes \vec{R} \tag{3.157}$$

Otherwise, one can update the matrix element-wise

$$M_{ij}^{new} = \tilde{M}_{ij} + \begin{cases} pL_i R_j, & i,j < k+1 \\ -pR_j, & i = k+1,\ j \le k+1 \\ -pL_i & i < k+1,\ j = k+1 \end{cases} \tag{3.158}$$

When two operators are removed, the update procedure is far simpler. We first rearange the matrix so that the row and column that need to be removed are last (at position k). Then

$$M_{ij}^{new} = M_{ij} - \frac{M_{ik}M_{kj}}{M_{kk}} \tag{3.159}$$

where the new matrix has dimension $k-1$.

However, for the trial step we just need the ratio between the new and old determinant, and the updates of $\mathbf{M}$ are performed only if the step is accepted. In the case of adding two operators, the ratio of determinants is given by

$$\frac{\det \boldsymbol{\Delta}^{new}}{\det \boldsymbol{\Delta}^{old}} = \frac{1}{p} \tag{3.160}$$

When two operators are removed, it is even simpler - if we want to remove the row n and column m

$$\frac{\det \boldsymbol{\Delta}^{new}}{\det \boldsymbol{\Delta}^{old}} = M_{nm}. \tag{3.161}$$

For the time shift update things are little different. We have two cases - one of the τ has changed or one of the τ' times has changed. That means that either a row or a column needs to be updated (respectively). Let's say a time τ_n has changed. We define two vectors of size k

$$\begin{aligned} U_i &= \delta_{ni} \\ V_i &= -\Delta_{\sigma_n,\sigma_i'}(\tau_n^{old} - \tau_i') + \Delta_{\sigma_n,\sigma'i}(\tau_n^{new} - \tau_i') \end{aligned} \tag{3.162}$$

where the second vector is the difference that needs to be applied to the row n of $\boldsymbol{\Delta}$, i.e. we subtract what is currently in the row, and add what now should be in

the row. In the case τ_n' has changed, it is the other way around

$$
\begin{aligned}
U_i &= -\Delta_{\sigma_i,\sigma_n'}(\tau_i - \tau_n'^{old}) + \Delta_{\sigma_i,\sigma_n'}(\tau_i - \tau_n'^{new}) \\
V_i &= \delta_{ni}
\end{aligned}
\tag{3.163}
$$

and the first vector is the change that needs to be applied to the column n. Now we define as previously

$$
\begin{aligned}
\vec{L} &= \mathbf{M}\vec{U} \\
\vec{R} &= \vec{V}\mathbf{M} \\
q &= \vec{V}\mathbf{M}\vec{U} = \vec{V} \cdot \vec{L} \\
p &= \frac{1}{1+q}
\end{aligned}
\tag{3.164}
$$

By the elements

$$
\begin{aligned}
L_i &= \sum_{j=1}^{k} M_{ij}U_j \\
R_i &= \sum_{j=1}^{k} V_j M_{ji} \\
q &= \sum_{i,j=1}^{k} V_i M_{ij} U_j = \sum_{j=1}^{k} V_j L_j = \sum_{i=1}^{k} R_i U_i
\end{aligned}
\tag{3.165}
$$

Now the updated M can be obtained as

$$
\mathbf{M}^{new} = \mathbf{M} - p\,\vec{L} \otimes \vec{R}
\tag{3.166}
$$

i.e.

$$
M_{ij}^{new} = M_{ij} - pL_i R_j
\tag{3.167}
$$

Same as before, in the trial step we only need the ratio of determinants, and

$$
\frac{\det \mathbf{\Delta}^{new}}{\det \mathbf{\Delta}^{old}} = \frac{1}{p}
\tag{3.168}
$$

which is also known as matrix determinant lemma. Note that either $\vec{U}$ or $\vec{V}$ will

have a single non-zero element, and it will be 1, so q is just the n-th element of $\vec{R}$ or $\vec{L}$ respectively. For the trial step, p can be obtained very cheaply, as we only have to calculate a single element of R or L.

The formula Eq. 3.161 can be used to efficiently perform the measurement of the Green's function in a given configuration x. We have

$$G_{\sigma_i \sigma'_j}(x; \ \tau'_j - \tau_i) = M_{ij} \tag{3.169}$$

We can go over all pairs ij and obtain an average, in each Monte Carlo step. Each combination of operators will yield a measurement at a different value of τ. We have

$$G_{\sigma\sigma'}(x; \ \tau) = \left\langle M_{ij}\delta_{\sigma'_j\sigma'}\delta_{\sigma_i\sigma} \left\{ \begin{array}{ll} \tilde{\delta}(\tau, \tau'_j - \tau_i), & \tau'_j - \tau_i > 0 \\ \tilde{\delta}(\tau, \beta + \tau'_j - \tau_i), & \tau'_j - \tau_i < 0 \end{array} \right. \right\rangle_{ij} \tag{3.170}$$

where the averaging is performed over all i and j, and $\tilde{\delta}$ is the "approximate" Kronecker delta - one must discretize time and store measurements into bins. A simpler way is to measure directly in imaginary frequency

$$G_{\sigma\sigma'}(x; \ i\omega_n) = \frac{1}{\beta}\left\langle e^{i\omega_n(\tau'_j - \tau_i)} M_{ij}\delta_{\sigma'_j\sigma'}\delta_{\sigma_i\sigma} \right\rangle_{ij} \tag{3.171}$$

The $\frac{1}{\beta}$ factor comes from the fact that we are integrating over one more variable than is needed. Note also that the averaging must be performed at each step, and then once more at the end of Monte Carlo procedure. If all the measurements were summed, then the diagrams with large k would be overrepresented, as the number of measurements available goes as k^2. Also, the measurement of the Green's function at high frequences can not be performed with high accuracy. In practice one patches the high-frequency "tail" by employing some analytic approximation. Namely the Hubbard-I approximation, or the atomic limit approximation which I state here

$$G_\sigma(i\omega \gg 1) = \frac{1 - \langle n_\sigma \rangle}{i\omega + \mu} + \frac{\langle n_\sigma \rangle}{i\omega + \mu - U} \tag{3.172}$$

Note that the Green's function is measured in each step, regardless of wheather the configuration has been updated. To be more precise, the measurements are best
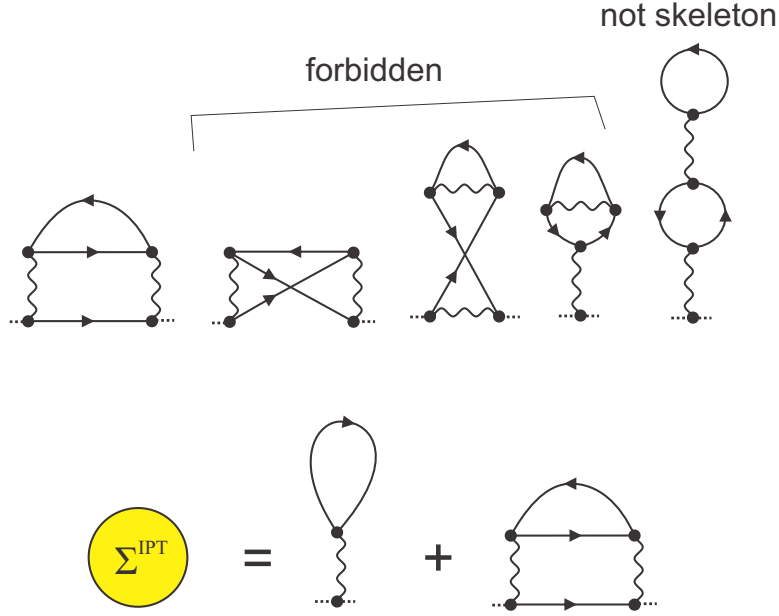
Figure 3.14: Upper row - irreducible, second order self-energy diagrams. Lower row - IPT approximation of self energy.

made each N_{ac} steps, to avoid autocorrelation. In the end we have

$$G_{\sigma\sigma'}(i\omega_n) = \langle G_{\sigma\sigma'}(x;\ i\omega_n)\rangle_{MC} = \frac{1}{N_{measurements}} \sum_i G_{\sigma\sigma'}(x_i;\ i\omega_n) \qquad (3.173)$$

3.4.2   Perturbative solution (IPT)

A very succesful approximate scheme for solving DMFT is known as the Iterative Perturbation Theory (IPT) [50, 51]. This approach carries on from Eq. 3.134 but keeps only the lowest two orders in the interaction expansion. Then, one can calculate self-energy directly, and restrict to only connected, proper self-energy diagrams. The first order diagram includes only one interaction vertex (Fig. 3.14) and corresponds to the mean-field contribution as it is not time (frequency) dependent. In second order, there are 5 possible diagrams of proper self-energy. However, three of them are immediately forbidden because in the Hubbard model, electrons of the same spin can not interact. The fifth diagram is not a skeleton diagram, and needs not be considered as its contribution will be included during DMFT iterations.

The second order contribution to self-energy then is just

$$\Sigma_\sigma^{(2)}(\tau) = U^2 \mathcal{G}_{0\,\bar\sigma}^2(\tau)\mathcal{G}_{0\,\bar\sigma}(-\tau) \qquad (3.174)$$

74

Note that all propagators in imaginary time are always purely real. $\mathcal{G}_{0\,\sigma}(0) = n_\sigma$ is the average occupancy of a given spin, but with respect to the non-interacting part of the Hamiltonian and in general does not correspond to the physical occupancy of the Hubbard model. If we restrict to paramagnetic solutions and particle-hole symmetry, this is, however, the case, and also

$$n_\uparrow = n_\downarrow = \frac{1}{2} = \mathcal{G}(0) = \mathcal{G}(\beta) \tag{3.175}$$
$$\mathcal{G}_0(\tau) = \mathcal{G}_0(\beta - \tau) = -\mathcal{G}_0(-\tau) \tag{3.176}$$

Furthermore, in imaginary frequency all the the propagators are purely imaginary.

$$\mathrm{Re}\mathcal{G}_0(i\omega) = 0 \tag{3.177}$$

The real part of self-energy is just a constant coming from the first-order diagram.

$$\mathrm{Re}\Sigma(i\omega) = \frac{U}{2} \tag{3.178}$$

The imaginary part of the self-energy can be obtained by Fourier transformation of $\Sigma^{(2)}(\tau)$. Note that the particle-hole symmetry is enforced by setting

$$\mu = U/2 \tag{3.179}$$

One of the biggest advantages of IPT, apart from its relative efficiency compared to CTQMC, is that it can be formulated in real frequency so as to avoid the need for doing the numerical continuation of the imaginary-axis data to the real axis. Similarly as in the case of optical conductivity, the second order self-energy diagram can be analytically continued to the real axis. Here, however, there is an additional simplification - in self-energy diagrams all the propagators can be exchanged for their local counterparts and there is no need for the summation over k. The resulting expression for the imaginary part of self-energy is

$$\mathrm{Im}\Sigma^{(2)}(\omega) = -U^2 \int d\omega' \left(A^-(\omega + \omega')P(\omega') + A^+(\omega + \omega')P(-\omega') \right) \tag{3.180}$$

where

$$A^\pm(\omega) \;=\; -\frac{1}{\pi}\mathrm{Im}\mathcal{G}_0(\omega)f(\pm\omega) \tag{3.181}$$

and

$$P(\omega) = \pi \int d\omega' \, A^+(\omega' + \omega)A^-(\omega') \tag{3.182}$$

The real part can be obtained from the imaginary part using the Kramars-Kronig relation

$$\mathrm{Re}\Sigma^{(2)}(\omega) = \frac{1}{\pi} \int d\omega' \, \frac{\mathrm{Im}\Sigma^{(2)}(\omega')}{\omega - \omega'} \tag{3.183}$$

and finally

$$\Sigma(\omega) = \frac{U}{2} + \Sigma^{(2)}(\omega) \tag{3.184}$$

Furthermore, at p-h symmetry, all the real frequency propagators satisfy

$$G(\omega) = G^*(-\omega) \tag{3.185}$$

including the second-order contribution of self-energy.

Note that away from particle-hole symmetry, additional considerations and a correction of the expression Eq. 3.184 must be made to ensure the correctness of the approximation in various limits. In this work, we used IPT only at half-filling.

The evaluation of the self-energy in this approximation boils down to calculating a 2D integral. However, a careful treatment of divergences in the integrands is essential for obtaining reliable results.

3.5 Maximum Entropy Method

The stochastic methods produce only the imaginary axis data. For example, the result of DMFT on the Bethe lattice is fully contained in the local Green's function $G(\tau)$ where τ goes from 0 to β, or $G(i\omega)$, where $i\omega$ are the Matsubara frequencies up to some cutoff frequency. However, to compute frequency dependent observables, in general one needs the real-axis spectral function. The relation between the Matsubara frequency and real frequency Green's functions is the following integral equation

$$G(i\omega) = \frac{1}{\pi} \int d\omega' \frac{\mathrm{Im}G(\omega')}{i\omega - \omega'} \tag{3.186}$$

or equivalently, applying the Fourier transformation

$$
\begin{aligned}
G(\tau) &= \frac{1}{\pi} \int d\omega' \operatorname{Im} G(\omega') \, T \sum_{i\omega} e^{i\omega\tau} \frac{1}{i\omega - \omega'} \\
&= \int d\omega' \, A(\omega') \, K(\omega', \tau)
\end{aligned}
\tag{3.187}
$$

where $A(\omega) = -\frac{1}{\pi} \operatorname{Im} G(\omega)$ and

$$
K(\omega, \tau) = \frac{e^{-\omega\tau}}{1 + e^{-\beta\omega}}
\tag{3.188}
$$

is the fermionic kernel function. Evaluating the integral on the right-hand side of this equation is trivial and the continuation of the real-axis data to the imaginary-axis is not problematic. However, it turns out that inverting this equation is an ill-posed task. Usually, the inversion of an integral equation is straightforwardly performed by switching to matrix notation. Suppose we have $G(\tau)$ in L time slices. Then we can consider the imaginary time data an L-dimensional vector $\vec{G}$. The same stands for $A(\omega)$, which is necessarily calculated in a finite number (say L) of discrete real frequencies. Then, the kernel function can be considered an $L \times L$ matrix. We have

$$
\vec{G} = \mathbf{K}\vec{A} \implies \vec{A} = \mathbf{K}^{-1}\vec{G}
\tag{3.189}
$$

However, the kernel function at high-frequencies and finite τ is exponentially small and so is the determinant of $\mathbf{K}$. Therefore, the inverse of $\mathbf{K}$ is ill-defined and this approach is useless. The information contained in $G(\tau)$ which is defined on a finite range of τ is spread out across $(-\infty, \infty)$ on the real axis. Furthermore, the higher the frequency ω, the less $G(\tau)$ is sensitive to the features in $A(\omega)$. This means that there are infinitely many different $A(\omega)$ which correspond to any given $G(\tau)$ within an infinitesimal error-bar.

The other straight-forward approach to the continuation would be the weighted least squares method. Here, one minimizes the disrepancy

$$
\chi^2[G, A] = \sum_{l=1}^{L} \frac{(G(\tau_l) - G_A(\tau_l))^2}{\sigma_l^2}
\tag{3.190}
$$

where $G_A(\tau_l) = \int d\omega \, A(\omega) \, K(\omega, \tau_l)$ is the imaginary time Green's function as obtained from the proposed real-frequency spectrum $A(\omega)$ and $\sigma_l^2 = \sum_{i=1}^{N} (G^i(\tau_l) - $

$G(\tau_l))^2/(N(N-1))$ is the standard deviation of the statistically averaged $G(\tau_l)$ (i goes over N measurements (MC steps) in the stochastic procedure, and $G^i(\tau_l)$ is the measure of the Green's function in the given step i). Unless one is looking for only the rough features of $A(\omega)$ and keeps the ω discretization very sparse, this method also fails and produces unphysical oscillations and noisy results.

When the DMFT result is well resolved and smooth, it is sometimes possible to continue data by fitting the Pade approximant (which is a ratio of two high order complex polynomials) to $G(i\omega)$ and then formally replacing $i\omega \to \omega$. This method boils down to solving a system of L linear equations. For example, the $G(i\omega)$ result obtained from the imaginary axis IPT can be of very high quality, but even then, the Pade method fails in some cases, producing unphysical features or appearantly noisy results. However, the method is of virtually no use when the original imaginary-axis data is degraded by numerical noise, as is usually the case with stochastic methods.

The cutting-edge method for the numerical continuation of the imaginary-axis data to the real-axis is the Maximum entropy method [59]. The main idea behind this method is to use Bayesian statistical reasoning to choose among many different $A(\omega)$ that reproduce $G(\tau)$ through Eq. 3.187 equally well. The working hypothesis of this approach is that the true $A(\omega)$ will have only the features necessary to reproduce $G(\tau)$, but will otherwise be featureless. The amount of structure, or correlation, in $A(\omega)$ can be quantified by a generalized Shannon-Jaynes entropy, which is a functional of both $A(\omega)$ and the default model $m(\omega)$

$$S[A,m] = \int d\omega \left(A(\omega) - m(\omega) - A(\omega) \ln \frac{A(\omega)}{m(\omega)} \right) \tag{3.191}$$

such that it goes to zero when $A(\omega) = m(\omega)$. Otherwise, the result of this integral is *always* negative, as the integrand can be only negative or zero. Say, $A(\omega)/m(\omega) = x$. Then the sign of the integrand is the sign of $x - 1 - x \ln x$ which can be only negative or zero (when $x = 1$). Note that both A and m are positive definite and normalized to 1. If $m(\omega)$ is just a constant, say a box distribution ($m(\omega) = \frac{1}{2\omega_{max}}$ where $|\omega| < \omega_{max}$, where ω_{max} defines the range of frequences in which A is calculated), then S will be a measure of deviation from a smooth featureless spectrum. Then, one can look for a spectrum $A(\omega)$ that not only minimizes the discrepancy χ^2, but also maximizes S. The quantity to maximize is then

$$P(A,G,m,\alpha) = e^{\alpha S[A,m] - \frac{1}{2}\chi^2[A,G]} \tag{3.192}$$

The relative importance of the two criteria is determined by the parameter α. Note, that in the absence of data ($\alpha \to \infty$) MEM yields the default model m. The choice of α and m constitutes the variant of MEM.

The *Classic* MEM maximizes P with respect to both A and α. This is done by nesting two optimization routines - the inner one searches for the optimal A given the value of α, and the outer one searches for the optimal α such that the P_{max} resulting from the inner routine is maximized. However, the distribution of $P_{max}(\alpha)$ can be very broad and skewed, such that mode (the most probable value) does not correspond to the mean (the average value).

The *Bryan* variant goes over a range of the values of α and averages the result for A

$$\langle A \rangle = \int d\alpha P_{max}(\alpha) A(\alpha) \tag{3.193}$$

Furthermore, the default model can be chosen to incorporate the a priori knowledge of A. In the annealing procedure, one starts by doing the continuation of the results obtained at some high temperature, where the spectrum is expected to be the smoothest and easiest to obtain. Then the result is used as the default model for the lower temperature, and so on.

In the work presented in this thesis, we used the classic MEM, both in the annealing scheme, and with a flat model. For further details of the procedure we used, see section 4.2.4.

4. Results: Quantum criticality of the Mott metal-insulator transition

The generic phase diagram of materials exhibiting the Mott transition and the resistivity in its vicinity are well reproduced by single-site DMFT. The main task in this chapter is to perform a detailed study of the DC resistivity throughout the DMFT phase diagram, identify different regimes, try to find evidence of quantum critical behavior at high temperatures, and compare the results to experiments.

The work is divided in two parts. In the first part we consider the interaction-driven phase transition at half-filling (section 4.1). On this example, we work out the generalization of the QC scaling formula necessary in the presence of a first order transition, by introducing the concept of quantum Widom lines (QWL, section 4.1.5). We then test the validity of this generalized scaling law in the case of DC resistivity, around the quantum Widom line. The results are then compared to the recent experiments on κ-organic systems.

In the second part we consider the doping-driven Mott transition at a large value of on-site interaction U. Here we complete the 3D (U, μ, T) phase diagram of the single-site DMFT and show that T_c for the first order transition reduces quickly as U is increased (sections 4.2.1 and 4.2.2). Then, we use the concepts introduced in the half-filled case to show that QC scaling is observed in this case as well, but down to much lower temperature, revealing a phenomenology much more similar to the pure QCP case. Furthermore, we find that the QC region matches the linear resistivity bad-metal region and find a surprising relation between the two phenomena (section 4.2.6). The results are compared with the experiment on superconducting cuprate films.

The work presented in this chapter is published in three papers [60, 61, 62].

4.1 Interaction-driven Mott MIT at half-filling

In single-site DMFT, at $T = 0$, a true Mott insulator is only observed at strictly half-filling. In the case of a Hubbard model on a particle-hole symmetric lattice, the filling factor of $n = 0.5$ is enforced by setting $\mu = U/2$, i.e. the Hubbard model reads

$$\hat{H} = -t \sum_{\langle i,j \rangle, \sigma} c_{i\sigma}^\dagger c_{j\sigma} + U \sum_i \left(\hat{n}_{i\uparrow} - \frac{1}{2} \right) \left(\hat{n}_{i\downarrow} - \frac{1}{2} \right) \tag{4.1}$$

Then, the phase diagram is examined by varying the value of on-site interaction U and temperature T. In this work we use the semi-circular non-interacting density of states, corresponding to the infinitely dimensional Bethe lattice or the fully-connected lattice with random hoppings such that their overall mean is zero (also known as the maximally frustrated Hubbard model). For the latter, only a fully paramagnetic solution is possible, and this is the one we focus on. The unit of energy is taken to be the half-bare-bandwidth $D = 2t = 1$ where t is the (unscaled, see section 3.2) hopping amplitude.
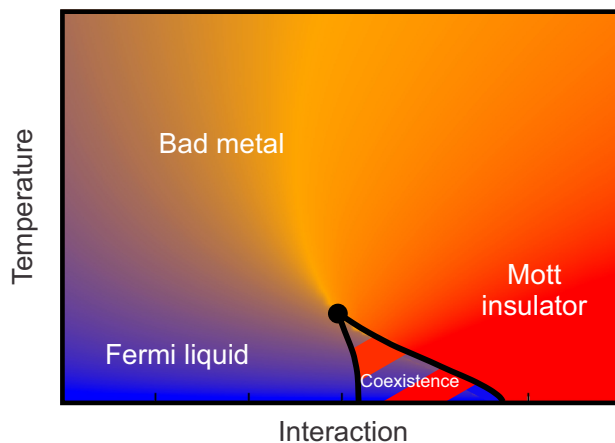
4.1.1 Phase diagram

Figure 4.1: Paramagnetic single-site DMFT phase diagram.

The phase diagram in the $U - T$ plane is shown in Fig. 4.1 . The DMFT solution reproduces the three regimes usually found close to a metal-insulator transition (MIT): Fermi liquid (FL), bad metal and Mott insulator, in qualitative agreement with experiments on various Mott systems.[24] We begin their characterization by first analyzing the behavior of the resistivity in the relevant range of parameters.
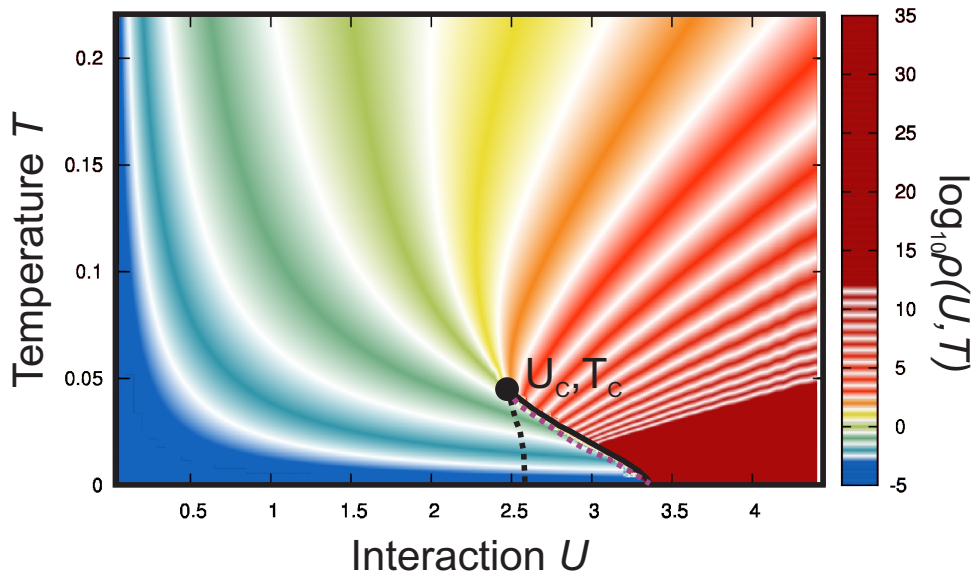
Figure 4.2: Resistivity (in units of ρ_{Mott}) calculated in the entire $U - T$ plane. The white stripes follow the lines of constant resistivity and separate the orders of magnitude in the resistivity. Spinodals are denoted with black lines, and the first order phase transition line is the (dashed) purple line.

Our IPT (see section 3.4.2) results are plotted in Fig. 4.2, where the value of resistivity is color-coded, with white stripes separating the orders of magnitude between 10^{-3} and 10^{13}. In this plot, the resistivity is given in the units of ρ_{Mott}, the maximal metallic resistivity in the semiclassical Boltzmann theory, defined as the resistivity of the system when the scattering length is equal to one lattice spacing.[63, 64] At zero temperature, the resistivity in the FL phase vanishes, while the Mott insulator has an infinite resistivity. With increasing temperature, the difference between the two states becomes less and less pronounced. Between the spinodals, both metallic and insulating solutions are possible, but in this plot only the metallic resistivity is shown. In the intermediate interaction $U < U_c$ and high temperature $T > T_c$ regime, the resistivity is comparable to or even larger than ρ_{Mott}, but it still (weakly) increasing with temperature, which is a characteristic of the "bad metal" regime observed in several Mott systems.[63]

It is remarkable how this way of presenting the data immediately creates the familiar "fan-shape" structure, generally expected for quantum criticality.[4] At high temperatures all the white constant-resistivity stripes seem to converge almost to the same point $U \sim U_c$. The perfect convergence, however, is interrupted by the

emergence of the coexistence done at $T < T_c$, but such behavior is exactly what one expects for "avoided quantum criticality" [65].
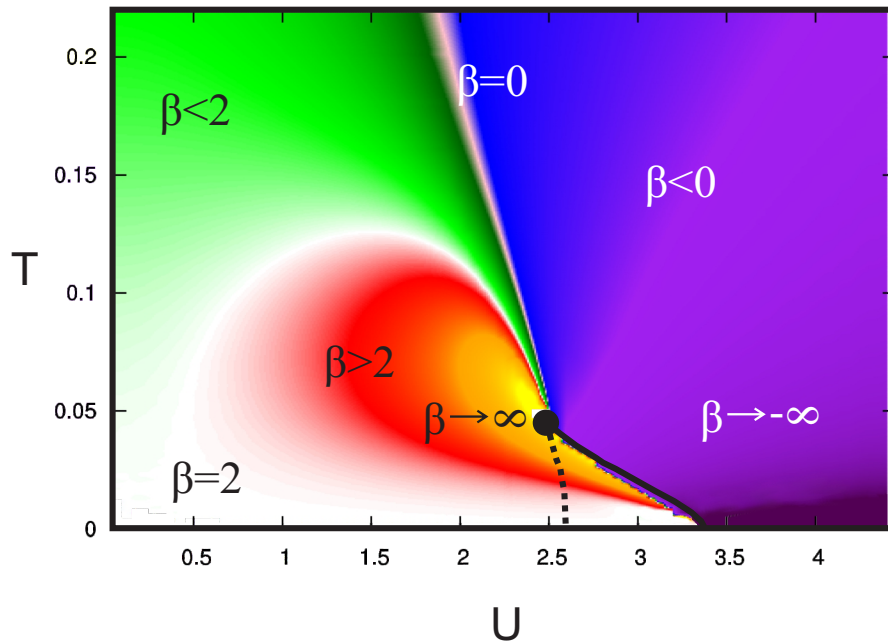

Figure 4.3: The effective exponent of the temperature dependence of resistivity ($\beta = d\log\rho/d\log T$) calculated in the entire $U - T$ plane illustrates the different transport regimes (see text).

Different regions of the phase diagram are also distinguished by the qualitatively different form for the temperature dependence of the resistivity. To make this behavior even more apparent, we follow a commonly-used procedure to displaying the data around QCP's - we compute the logarithmic derivative of resistivity with respect to the temperature, i.e. the "effective exponent"[66, 67]

$$\beta(T, U) = d\log\rho(U, T)/d\log T, \tag{4.2}$$

which is color-coded in Fig. 4.3. On the metallic side, at the lowest temperatures, one finds a typical metallic dependence of the form $\rho \sim T^2$ and here we have $\beta = 2$ (white). Far from the transition, this regime survives up to relatively high temperatures, but eventually the temperature dependence of the resistivity gradually slows down, displaying behavior sometimes described as "marginal Fermi-liquid" transport (green, $\beta \sim 1$). Closer to the transition, this is preceded by an increase in
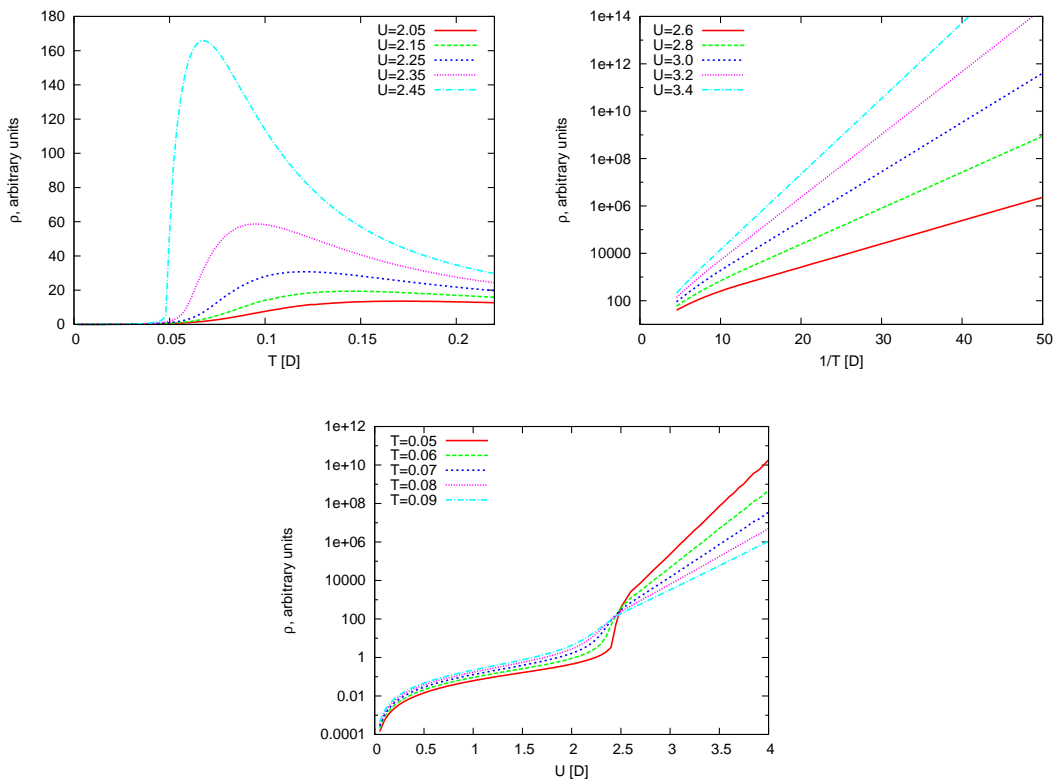
Figure 4.4: Upper left: on the metallic side, close to the transition, resistivity is non-monotonic. Upper right: on the insulating side, resistivity is exponentially decreasing with temperature. This trend is slightly modified close to the transition. Lower panel: above the critical end-point, there is a clear inflection point in $\log \rho(U)|_T$.

the effective exponent (red), which is a reflection of the existence of the critical end-point in which β diverges (yellow). Very close to the transition, a maximum of the resistivity is reached at some temperature (pink) (see also Fig. 4.4) and the trend of the resistivity increase is then reversed. On the other side of the phase diagram, deep in the Mott insulator, one finds typical activation curves (see also Fig. 4.4) which exhibit the exponential drop in the resistivity with increasing temperature, due to the gap in the excitation spectrum (black and purple). However, just above the coexistence dome, one finds an intermediate regime, where the behavior is generally insulating because the resistivity decreases with temperature, but the gap is not yet fully open, and the temperature dependence deviates from exponential (blue). This region is sometimes referred to as the "bad insulator."
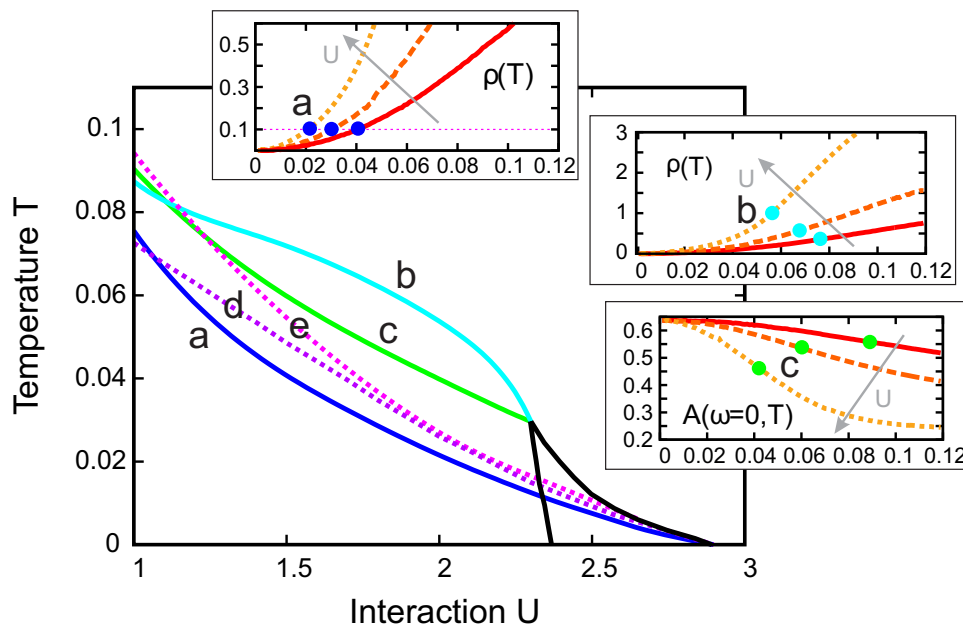
Figure 4.5: Various definitions for the crossover lines between the Fermi liquid and the bad metal. The meaning of each definition is illustrated on a smaller panel to the right. The results are obtained with the CTQMC.

4.1.2 Crossover lines

In the previous section we have characterized the different regimes in the vicinity of the Mott MIT: Fermi liquid, bad metal and Mott insulator. However, apart from the spinodals, the properties of the system change continuously in the entire phase diagram. The lines separating the different regimes are thus a matter of convention and many definitions can be found in literature.

In Fig. 4.5 we present the lines corresponding to various definitions of a crossover line between the Fermi liquid and the bad metal regimes. The definition of each line is illustrated on a smaller panel on the right, where the corresponding feature in the resistivity and other relevant quantities is marked with the dots of the same color. All the results are obtained with CTQMC impurity solver (see section 3.4.1). The dark blue line (a) is defined by $\rho = 0.1\rho_{Mott}$ and it roughly corresponds to the Fermi coherence temperature T_{FL} (the temperature above which the temperature-dependence of resistivity is no longer quadratic; this can also be seen in Fig. 4.3). The corresponding small panel (a) shows the resistivity as a function of temperature, plotted for three different values of U. The dotted horizontal line marks $\rho = 0.1\rho_{Mott}$. The arrow denotes the direction of increase of U. The light blue line (b) corresponds

to the inflection point of the resistivity, $d^2\rho(\omega = 0)/dT^2 = 0$ (see also Fig. 4.4), and the green line (c) is determined as the inflection point of the spectral density at the Fermi level with respect to the temperature, $d^2A(\omega = 0)/dT^2 = 0$. These are illustrated on smaller panels (b) and (c) where the DC resistivity and $A(\omega = 0)$ are plotted versus the temperature, for three different values of U. The inflection points are marked with the dots of color corresponding to the (b) and (c) lines on the main panel. The additional two dotted lines are: (d) the quasi-particle weight at zero temperature defined by

$$Z = \left[1 - d\mathrm{Im}\Sigma(i\omega_n)/d\omega_n|_{\omega_n \to 0}\right]^{-1}$$

and (e) the zero temperature local spin susceptibility $\chi(i\nu = 0) = \frac{1}{\beta}\int d\tau d\tau' \langle \vec{S}_i(\tau) \cdot \vec{S}_i(\tau')\rangle$. Both quantities are divided by 10 to fit in the temperature range of the plot and to be more easily compared to the crossover lines. It is evident that the coherence temperature is roughly proportional to the quasi-particle weight at zero temperature, but with the prefactor 0.1, $T_{\mathrm{FL}}(U) \sim 0.1\ Z(U)$. As compared with the doped Hubbard model,[45, 68] T_{FL} is higher, but still distinct from the temperature corresponding to ρ_{Mott}, in agreement with the experiments on organic materials.[64, 69, 70] The quasiparticle weight Z is weakly temperature dependent and the Drude peak in the optical conductivity is still pronounced for $\rho \lesssim \rho_{Mott}$.[71]

In contrast with these lines, one can also define the lines separating the bad metal from the (bad) Mott insulator. In Fig. 4.6, we present several criteria for their definition. In analogy to the line (a) of Fig. 4.5, one can use the resistivity to distinguish between the two regimes. The dark blue line (a) plotted here, connects the points where the resistivity is equal to the one found precisely at the critical endpoint, which we estimate to be roughly $10\rho_{Mott}$. The light-blue line (b) marks the inflection point of logarithmic resistivity as a function of U ($\partial^2 \log \rho(U, T)/\partial U^2 = 0$). It is well pronounced feature up to high temperatures, and it is a direct consequence of the discontinuity along the spinodals at $T < T_c$. These two are illustrated on the small panel to the right, where $\log \rho(U)$ is plotted at three different temperatures. The dark blue dots are the intersections of these lines with the dotted, $10\rho_{Mott}$ line. The inflection points are marked with the light blue dots, and are found at slightly lower values of U. Another natural definition for the crossover is the $\beta = 0$ line (c), as it marks the place where the trend of resistivity growth is reversed. At its right-hand side, the resistivity decreases with temperature, which is a sign of insulating
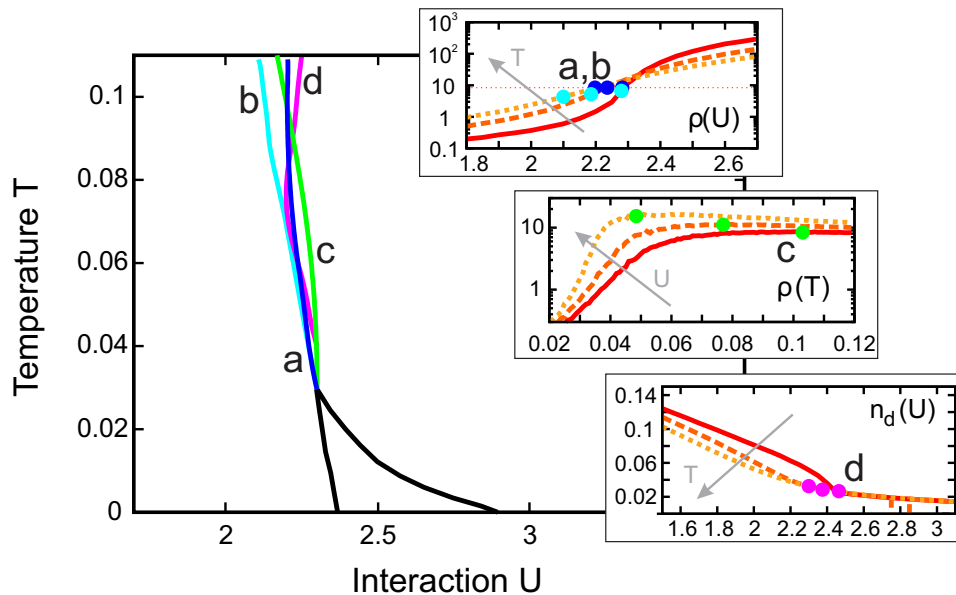
Figure 4.6: Various definitions for the crossover lines between the bad metal and the Mott insulator. The meaning of each definition is illustrated on a smaller panel to the right. The results are obtained with the CTQMC.

behavior. This is illustrated on the corresponding small panel, where $\log \rho(T)$ is plotted for 3 different values of U and the maxima are marked with the green dots. The double occupancy n_d has an obvious change in trend on crossing the line (d). Here, the second derivative $\partial^2 n_d / \partial U^2$ has a sharp maximum, and separates the two distinct regimes of $n_d(U)$, both almost linear but with different slopes. This is apparent on the small panel (d) where double occupancy is plotted as a function of U at various temperatures.

It is striking that these lines almost coincide, in sharp contrast to what is seen in Fig. 4.5. Although the opening of the gap is very gradual, it is possible to pin-point the boundary between the two regimes and actually divide the supercritical part of the phase diagram into metallic and insulating-like regions.

4.1.3 Generalization of the QC scaling formula

In the standard scenario for quantum criticality [4, 72], the system undergoes a zero-temperature phase transition at a critical value of some control parameter $g = g_c$, and within a "V-shaped" finite temperature region stemming from the QCP, physical

quantities display scaling behavior of the form

$$A(g, T) = A_c(T) \ F \left(\frac{g - g_c}{T^{1/z\nu}} \right) \tag{4.3}$$

where $A_c(T) \equiv A(g_c, T)$. Mott MIT is a first order phase transition [73], but the corresponding coexistence region is confined to extremely low temperatures, and at temperatures sufficiently above the classical critical end-point T_c, the quantum effects are expected to set in [4], and restore the QC behavior. However, to test the QC scaling hypothesis in the case of a first-order transition, one must first identify the appropriate g_c which enters the argument of the scaling function (Fig. 4.7). It is immediately clear that the critical value g_c of the control (transition-driving) parameter g must be replaced by a more general, temperature dependent quantity. Below T_c one may identify it with the line of the first order transition $g_c(T)$ along which the two coexisting phases are equally favorable (purple dashed line in Fig. 4.2). However, above T_c, no actual transition takes place, and the trajectory $g_c(T)$ can only be a crossover line - therefore it is not uniquely defined. In this work we choose to use the general concept of Widom lines and define $g_c(T > T_c)$ in a way that it is a well defined and logical continuation of $g_c(T < T_c)$. In the next section we discuss the concept of Widom lines and then devise a way to apply it in a completely general case.

However, there is an additional problem in treating the first-order Mott transition in terms of quantum critical behavior. The Eq. 4.3 assumes that there is no phase transition away from zero temperature, so all the quantities must be analytic
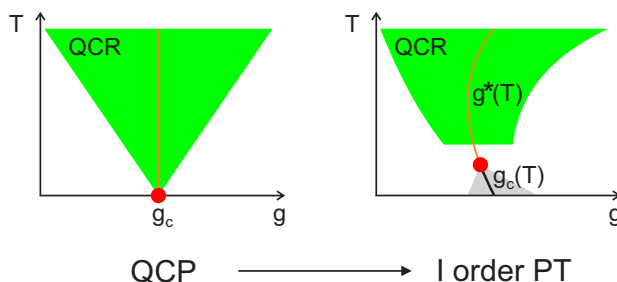

Figure 4.7: Standard QCP scenario is modified in the case of the Mott MIT. The critical transition-driving parameter g_c is replaced by a more general, temperature dependent quantity. Below T_c this is the line of first order transition $g_c(T)$ where the two states are equally favorable. Above T_c it is the line of "maximal instability" of the ground state (see section 4.1.5), or the quantum Widom line $g^*(T)$.

functions of g and T. Only at precisely the QCP ($g = g_c, T = 0$), the argument of the scaling function F changes from $-\infty$ to ∞ thus allowing for a non-analytic behavior of A. Then if we apply the Eq. 4.3 to the case of resistivity in single-site DMFT, we have

$$\rho(U, T) = \rho_c(T) \, F \left(\frac{U - U_c(T)}{T^{1/z\nu}} \right) \tag{4.4}$$

and we run into a problem immediately, even if $U_c(T > T_c)$ is known - the first derivative of resistivity is divergent at the critical point (U_c, T_c) (Fig. 4.3)

$$\left. \frac{\partial \rho}{\partial U} \right|_{U_c, T_c} \to \infty \tag{4.5}$$

which certainly can not be described by Eq. 4.4. Furthermore, the vicinity of the critical point has been described by a classical scaling theory in the work of Kotliar and Rozenberg Ref. [36] with a great level of success, and revealed that the second order transition here is of the classical Ising type with $\nu = 1$. Therefore, the quantum critical behavior is necessarily spoiled by the presence of the finite temperature critical point, but at temperatures sufficiently higher than T_c, it is still justified to pursue an understanding of the system behavior in terms of quantum criticality.

4.1.4 Widom crossover lines

The notion of a crossover line is very general and different physical motivations can be used for its precise definition. The concept of the Widom crossover line is, however, more strict and relies on one fundamental principle - non-analytic features at the critical point become smoothed out at super-critical temperatures, but remain well defined.

The Widom line was originally defined in the context of liquid-gas phase transition,[74] as the line connecting the maxima of the isobaric specific heat as a function of pressure ($\partial C_p / \partial p = 0$), above T_c (Fig. 4.8). It was conceived as a logical continuation of the first order phase transition line to supercritical temperatures. C_p is divergent at the critical end-point, which directly causes the maxima in C_p present above the critical temperature. This concept is easily generalized to include all the lines that mark features directly caused by non-analyticities due to a phase transition.[75] As such, a Widom line can be defined by any quantity that exhibits either a divergence or a discontinuity because of a phase transition, and thus a maximum or an inflection

point above T_c.

Very recently,[76] in the super-critical region of argon liquid-gas phase diagram, an unexpected non-analyticity has been found in sound velocity dispersion curves, precisely at the Widom line. The authors give a new depth and physical meaning to the concept, by observing that there is no single super-critical fluid phase, and that the Widom line actually separates two regimes of fluid-like and gas-like dynamical behavior. This finding makes it clear that the Widom lines should not be exclusively connected with thermodynamics of the system. The changes in transport that follow certain features in thermodynamic quantities can also be used for making meaningful and possibly even equivalent definition of the Widom line. The significance of this concept was recognized once more[77, 78] in the context of hole-doped high-T_c superconductors, where the characteristic temperature T^* of the pseudogap phase is shown to correspond to the Widom line arising above a first-order transition at critical doping.

In the above sense, we emphasize that the the concept of Widom lines can also be easily connected with our model, possibly giving it new physical importance in the context of quantum phase transitions. One can immediately recognize that the $\log \rho(U)|_T$ inflection-point line (Fig. 4.6) qualifies as a generalized Widom line - it emanates from the the critical end-point, separates regions of metallic and insulating
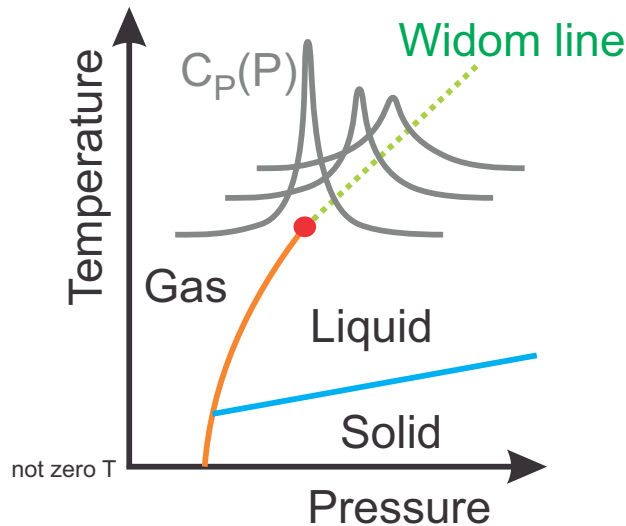

Figure 4.8: Widom line is defined in the context of classical liquid-gas transitions. The isobaric specific heat diverges at the critical point, and has clear maxima at supercritical temperatures.

behavior, and marks a feature that is directly caused by a non-analyticity (divergence of $\frac{\partial \rho}{\partial U}\big|_{U_c, T_c}$) due to the phase transition. However, we also want to base the definition of the Widom line in a purely thermodynamic quantity such that it is possible to define it in an arbitrary model, and then compare it to the inflection point line and other crossover lines separating the metallic-like and insulating-like behavior shown in Fig. 4.6. Furthermore, we want our Widom line to be well defined even when T_c for the first order transition goes to zero - if the Widom line is defined in a quantity that diverges (goes to zero) at the critical point, then the existence or non-existence of the first order transition below the critical point is irrelevant for the supercritical behavior, and the Widom line should be possible to define even in the case of a purely zero-temperature (quantum) phase transition, i.e. when the critical point has been brought down to zero temperature. In the following, we find a thermodynamic quantity that goes to zero at precisely the critical point, has a clear minimum above T_c, and should be possible to calculate in any method based in the Legendre formalism, as described in section 3.1.1.

4.1.5 Instability line as the quantum Widom line

One possible intuitive interpretation of the scale invariance of a critical point is that, at this point, system is completely indecisive of its behavior - since the transition is of the second order, thermodynamic quantities do not exhibit discontinuity, which means that the two phases on different sides of the CP become the same at the CP. At precisely the CP, there are excitations available at virtually no cost, and the fluctuations are present at all time and length scales. Therefore, at a supercritical temperature, the point analogous to the CP is the one at which low lying collective excitations available are the least costly. This point of indecisiveness, or instability, may be interpreted as the point at which the system is in equal proximity to the two competing phases. In the usual Ginzburg-Landau field theory, the spectrum of low-lying collective excitations is in principle given by the landscape of an appropriate Free energy functional, in the vicinity of its global minimum. As has been shown in section 3.1.1, DMFT procedure can be identified with minimizing one such Free energy functional of the hybridization function. The curvature (we denote it λ) of this Free energy functional in its global minimum (or local, which is the case in the phase coexistence region) is actually a very general quantity that describes the response of the system to an infinitesimal external perturbation, which may

be a time-dependent field of an arbitrary form. As such, λ is very important in describing a thermodynamic state close to the Mott MIT, since it has a fundamentally dynamic nature. Indeed, λ vanishes precisely at the critical end-point, as the free-energy functional becomes flat around G_{DMFT}. This is directly connected to the critical slowing down of dynamics, which manifests as the vanishing of a characteristic frequency scale. Above T_c, λ is related to the local stability of a given thermodynamic state and has a minimum precisely where the system is the least stable. Therefore, we define the instability line as the line connecting the minima of λ vs. U. It emanates from the critical point where $\lambda = 0$ and can therefore be considered a generalized Widom line. Since it does not require the presence of a finite T transition and can be defined even if $T_c = 0$, we dub it *quantum Widom line*.

A few more comments are in order - $\Delta(i\omega_n)$ is an infinitely dimensional vector in the corresponding Hilbert space, and the curvature of the Free energy at the self-consistent $\Delta_{DMFT}(i\omega_n)$ may be different in different directions. However, it is the curvature along the direction along which the curvature is the least, that matters. Luckily, this is the one that can be measured straight-forwardly in the DMFT procedure.

Here we present in detail the considerations that connect the convergence rate of the DMFT loop to the curvature of the Free energy functional, precisely at the stationary point corresponding to a self-consistent DMFT solution. The discussion presented here builds on the Taylor expansion presented in Eq. 3.19-Eq. 3.23 and is a concrete example how these general considerations become useful.

4.1.5.1   Connecting the Free energy curvature with the convergence rate

Immediately from Eq. 3.26, the free energy functional $\Omega[\Delta, G, \alpha = 0]$ is given by [24, 79, 36]

$$\Omega[\Delta, G, \alpha = 0] \;\; = \;\; -\mathrm{Tr}\,\Delta\,G + F_{imp}[\Delta], \tag{4.6}$$

where the first term may be interpreted as the energy cost of forming the generalized Weiss field Δ around the singled-out Hubbard site at which the local Green's function is given by G, while the second term is the free energy of an electron at this site in the presence of the Weiss field Δ. The first term comes from the non-local processes and corresponds to the kinetic energy, while the second term corresponds to the

potential energy, gained from the local, on-site interaction of electrons.

Close to a stationary point $\Delta = \Delta[G, \alpha = 0]$, we can Taylor expand $\Omega[\Delta, G, \alpha = 0]$ in terms of deviation from this point $\delta\Delta = \Delta - \Delta[G, \alpha = 0]$:

$$\Omega\Big[\Delta \approx \Delta[G, \alpha = 0], G, \alpha = 0\Big] \;=\; \Omega\Big[\Delta = \Delta[G, \alpha = 0], G, \alpha = 0\Big]$$
$$+ \sum_{mn} \delta\Delta(i\omega_m) M_{mn} \delta\Delta(i\omega_n) + \dots$$

where

$$M_{mn} = \frac{\partial^2 \Omega\Big[\Delta, G, \alpha = 0\Big]}{\partial\Delta(i\omega_n)\partial\Delta(i\omega_m)}\Bigg|_{\Delta = \Delta[G, \alpha = 0]} \tag{4.7}$$

is the fluctuation matrix. Note that $\mathbf{M}$ is not an implicit functional of G because taking the second derivative with respect do Δ washes out the G dependence, and F_{imp} is not a functional of G from the start. In matrix notation we write

$$\Omega\Big[\Delta \approx \Delta[G, \alpha = 0], G, \alpha = 0\Big] = \Omega\Big[\Delta = \Delta[G, \alpha = 0], G, \alpha = 0\Big] + \delta\vec{\Delta}\mathbf{M}\delta\vec{\Delta} \tag{4.8}$$

Taking the derivative of the above expression and taking into account Eq. 4.6, we have immediately that in the vicinity of the stationary point

$$\frac{\partial\Omega[\Delta, G, \alpha = 0]}{\partial\Delta(i\omega_n)} = G_n - G_n[\Delta] \approx \Big(\mathbf{M}\delta\vec{\Delta}\Big)_n \tag{4.9}$$

Up until now the considerations closely followed Eq. 3.19-Eq. 3.23. Now we consider our particular case - the DMFT solution in the case of the Bethe lattice corresponds to the stationary point of Ω such that $\Delta(i\omega_n) = t^2 G(i\omega_n)$. This solution can be obtained by following the forward recursion procedure, as described in section 3.3.2.1. In each new iteration $i + 1$, we take the result G of the impurity problem in the previous iteration i, and construct the hybridization function for the next iteration as $\Delta_n^{(i)} = t^2 G_n^{(i)}$. Therefore, $G_n^{(i+1)} = G_n[\Delta^{(i)}]$. Taking this into account and subtracting the DMFT self-consistent solution from both sides of the Eq. 4.9 we obtain

$$\delta\vec{G}^{(i+1)} = \delta\vec{G}^{(i)} - \mathbf{M}\delta\vec{G}^{(i)} \tag{4.10}$$

where we have absorbed the t^2 factor into the fluctuation matrix. The above equation can be understood in the following way: *the gradient of the functional Ω with respect to Δ in the point $[\{\Delta_n = t^2 G_n\}, G, \alpha = 0]$ is given by the difference between G*

and $G[\{\Delta_n = t^2 G_n\}, \alpha = 0]$, *i.e. the Green's function obtained as the result of the impurity problem and the one used to construct the hybridization bath for the impurity problem. The DMFT self-consistent solution G^* corresponds to the gradient $(\mathbf{M}\delta\vec{G}^*)$ being zero (because $\delta\vec{G}^* \overset{def}{=} 0$ by definition), which is observed when the impurity problem yields the same Green's function that has been used in constructing the hybridization bath.*

When we are sufficiently close to the self-consistent solution, equation Eq. 4.10 connects the Green's functions in two consecutive iterations of the forward recursion procedure. Then, we can use the recursive form of this equation to connect the Green's function in any iteration, with the initial guess

$$
\begin{aligned}
\delta\vec{G}^{(i+1)} &= \delta\vec{G}^{(i-1)} - \mathbf{M}\left(\delta\vec{G}^{(i-1)} - \mathbf{M}\delta\vec{G}^{(i-1)}\right) \\
&= \delta\vec{G}^{(i-2)} - \mathbf{M}\left(\delta\vec{G}^{(i-2)} - \mathbf{M}\left(\delta\vec{G}^{(i-2)} - \mathbf{M}\delta\vec{G}^{(i-2)}\right)\right) \\
&= (1 - \mathbf{M})^{i+1}\delta\vec{G}^{(i=0)}
\end{aligned}
\tag{4.11}
$$

Furthermore, the eigenbasis $\{\vec{G}_m\}$ and eigenvalues λ_m of matrix $\hat{M}$ are defined by

$$
\mathbf{M}\vec{G}_m = \lambda_m \vec{G}_m.
\tag{4.12}
$$

We can write $\delta\vec{G}^{(i)}$ as

$$
\delta\vec{G}^{(i)} = \sum_m a_m^{(i)} \vec{G}_m
\tag{4.13}
$$

where $a_\alpha^{(i)}$ are the coefficients of $\delta\vec{G}^{(i)}$ in the eigenvalue basis. Substituting into Eq. 4.11, one obtains

$$
\delta\vec{G}^{(i)} = \sum_\alpha e^{-iB_m} a_m^{(0)} \vec{G}_m,
\tag{4.14}
$$

where

$$
B_m = -\ln(1 - \lambda_m)
\tag{4.15}
$$

For large iteration index i the term with lowest $B_m = B_{m_0}$, which corresponds to the lowest eigenvalue $\lambda_{m_0} \equiv \lambda$, is dominant

$$
\delta\vec{G}^{(i)} = e^{-iB_{m_0}} a_{m_0}^{(0)} \vec{G}_{m_0}, \quad i \gg 1.
\tag{4.16}
$$

Here a_{m_0} is the coefficient corresponding to the eigenvector $\vec{G}_m$ with the lowest eigenvalue λ_m. Now it is obvious that through iterations, the solution $\vec{G}$ approaches
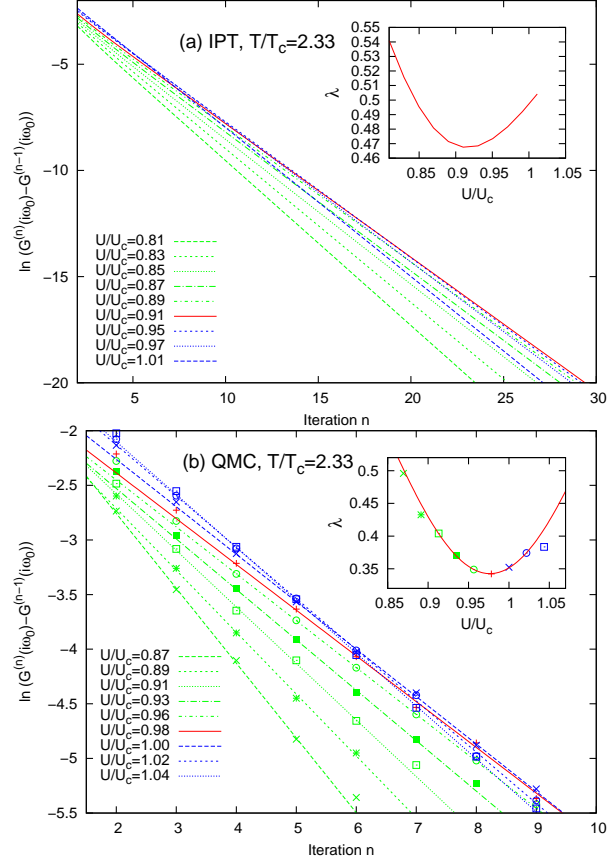
Figure 4.9: Convergence rate in the iterative solution of DMFT equations at $T/T_c = 2.33$ using IPT impurity solver, panel (a), and CTQMC impurity solver, panel (b). The dashed lines in panel (b) are linear fits to the data. The insets are the corresponding eigenvalues determined from the slopes shown in the main panels.

to the self consistent solution $\vec{G}_{DMFT}$ exponentially, along a direction defined by the eigenvector of $\hat{M}$ corresponding to its minimal eigenvalue λ. The coefficient B_{m_0} and the corresponding eigenvalue λ are then obtained from the slope in the iterative relation

$$\ln\left[G(i\omega_n)^{(i+1)} - G(i\omega_n)^{(i)}\right] = const - iB_{m_0}, \tag{4.17}$$

which follows from Eq. (4.16).

4.1.5.2 Determining the instability line

In practice, to obtain λ (and thus the curvature of free energy), we monitor DMFT loop convergence rate, $G(i\omega_o)^{(i+1)} - G(i\omega_o)^{(i)}$, in as many iterations as possible and then linearly fit $\ln\left(G(i\omega_o)^{(i+1)} - G(i\omega_o)^{(i)}\right)$ versus iteration index i. Here $\omega_o = \pi T$
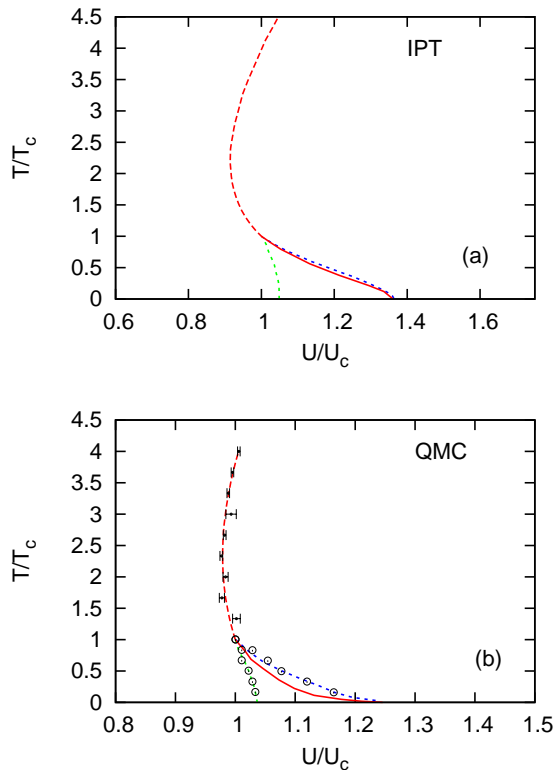
Figure 4.10: Phase diagram obtained with IPT, panel (a), and CTQMC, panel (b). Temperature and interaction are scaled by their values at the critical endpoint ($T_c^{IPT} = 0.046$, $T_c^{QMC} = 0.03$ and $U_c^{IPT} = 2.472$, $U_c^{QMC} = 2.3$). Red dashed line is the instability line $U^*(T)$, full red line is the line of the first order MIT, and green and blue dotted lines are left and right spinodals.

is the lowest Matsubara frequency. For small λ, $B_{m_0} \approx \lambda$. It takes few iterations of the DMFT loop to enter into the linear regime given by Eq. (4.17). We then repeat this procedure for different values of U at the same temperature T to determine $U^*(T)$ in which $\lambda(U)|_T$ is minimal.

An example of our calculations is shown in Fig. 4.9, where the eigenvalues λ at several temperatures are plotted as a function of interaction U. The minima of these curves define the instability trajectory $U^\star(T)$, which terminates at the critical end-point (U_c, T_c), as shown on Fig. 4.10.

With IPT impurity solver, we can use data from several tens of iterations to determine the slope B_{m_0}, Fig. 4.9a. The solution with CTQMC impurity solver has a statistical error and the number of iterations we can use is limited. When the difference $|G(i\omega_o)^{(i+1)} - G(i\omega_o)^{(i)}|$ becomes comparable to the level of numerical
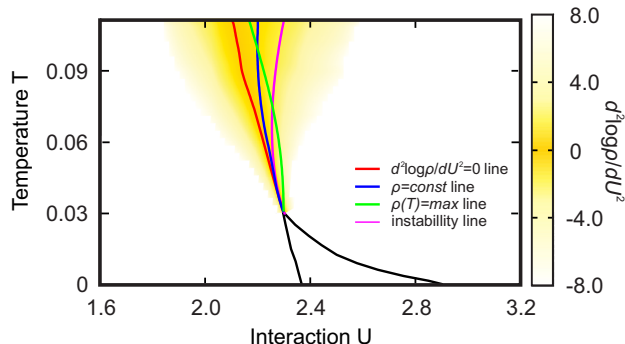
Figure 4.11: Instability line lies among the other crossover lines. $\log \rho(U)$ is linear in this crossover region, which is a manifestation of the mirror-symmetry of the scaling function (see section 4.1.6.1).

noise in CTQMC, the impurity Green's function just fluctuates around the self-consistent solution and no further convergence is observed. Nevertheless, we were able to determine rather precisely the eigenvalue λ_{m_0} and the interaction $U^*(T)$ for which it becomes minimal, Fig. 4.9b. The "instability line" corresponding to the minimum curvature of the free energy is shown in Fig. 4.10a (IPT phase diagram), and Fig. 4.10b (CTQMC phase diagram). Error bars in Fig. 4.10b are estimates of the uncertainty in the position of the instability line.

In Fig. 4.11 we compare the instability line with other possible crossover lines and find that it clearly lies among them. The instability line truly represents a boundary between a metallic and insulating transport and it lies in the region where

$$\frac{\partial^2 \log \rho(U, T)}{\partial U^2} \approx 0. \tag{4.18}$$

This derivative is color-coded in the (U, T) plane in Fig. 4.11.

The properties of the system in the crossover region are best illustrated in Fig. 4.12 The middle column shows the DOS along the instability line for three different temperatures. While the DOS at the Fermi level is strongly suppressed, the gap is not yet fully open. Left column shows the density of states in the metallic phase following a trajectory parallel to the instability line: there is a clear quasiparticle peak at low temperatures, which gradually disappears as the bad metal region is reached by increasing the temperature. At larger U (right column) the system is in the insulating phase with fully open Mott gap, featuring activated transport.
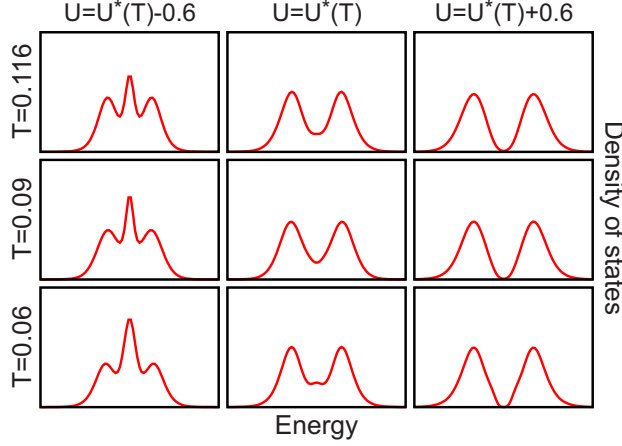
Figure 4.12: Density of states (QMC results) along the instability line $U^*(T)$ (middle column), and along the parallel trajectory for smaller (left column) and larger U (right column).

4.1.5.3   Visualizing the Free energy landscape

We can visualize the shape of the infinitely dimensional free energy surface by calculating $\mathcal{F}[G] = \Omega[\Delta = t^2 G, G, \alpha = 0]$ along a single direction going through the self-consistent $\vec{G}_{DMFT}$. Below T_c, we do this along the direction connecting the two solutions, constituting a parametric trajectory

$$\vec{G}(l) = (1 - l)\vec{G}_M - l\vec{G}_I. \tag{4.19}$$

Above T_c, where there is only one solution, we follow the eigenvector $\vec{G}_\lambda$ with

$$\vec{G}(l) = \vec{G}_{DMFT} + l\vec{G}_\lambda \tag{4.20}$$

The relative change of the free energy is calculated[37] as an integral

$$\Delta\mathcal{F}(l) = \mathcal{F}\Big[\vec{G}(l)\Big] - \mathcal{F}\Big[\vec{G}_{M/DMFT}\Big] = t^2 T \int_0^l dl' \, \vec{e} \cdot \vec{g}\Big[\vec{G}(l')\Big] \tag{4.21}$$

where $\vec{e}$ is the unit vector of the followed direction ($\vec{e} = (\vec{G}_M - \vec{G}_I)/|\vec{G}_M - \vec{G}_I|$ below T_c and $\vec{e} = \vec{G}_\lambda/|\vec{G}_\lambda|$ above T_c). The gradient vector takes the form

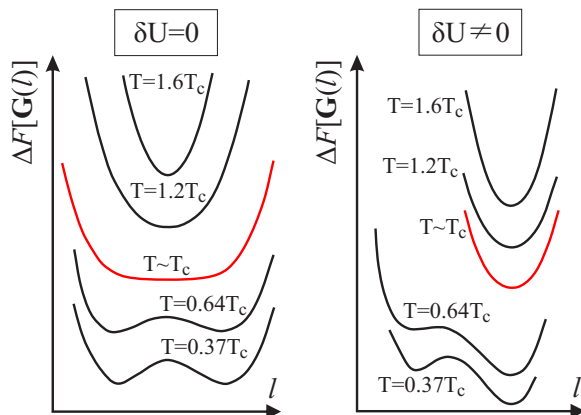$$\vec{g}\Big[\vec{G}\Big] = \vec{G}\Big[\vec{\Delta} = t^2 \vec{G}\Big] - \vec{G} \tag{4.22}$$

Figure 4.13: Free energy landscape (IPT results): (a) Along the instability/first order transition line ($\delta U = 0$). At $T > T_c$, the curvature of the free energy increases with temperature, and it is zero at $T = T_c$. Below T_c, at the first order transition line metallic and insulating solutions have the same free energy. (b) Along a line parallel to the instability/first order transition line ($\delta U = -0.05$). At $T > T_c$, the curvature of the free energy is greater than at the instability line. In the coexistence region one of the minima is energetically favored. Note that the spacing between $\Delta \mathcal{F}$ curves for different temperatures is arbitrary.

where $\vec{G}\left[\vec{\Delta} = t^2 \vec{G}\right]$ is the output of the impurity solver.

Panel (a) in Fig.4.13 shows the free energy landscape around $\mathbf{G}_{DMFT}$, precisely at the instability line. The curvature of the global minimum vanishes as one approaches T_c, which is consistent with eigenvalue λ being zero at this point. Below T_c there are two minima and the instability line is no longer well defined, but it is logically continued to the line of the first order phase transition, where two possible solutions are of the same energy. On Fig.4.13b, we move along a parallel trajectory, defined by $\delta U \neq 0$. It is immediately obvious that λ never reaches zero and that in the coexistence region one of the solutions is energetically favoured. This physical picture is common to various models. For example, it is seen in the Ising model in an external field, where the analogy is between the strength of the magnetic field and δU in our case.

4.1.6 QC scaling tests

To reveal quantum critical scaling, we calculate the temperature dependence of resistivity along a set of trajectories parallel to our instability trajectory (fixed $\delta U = U - U^{\star}(T)$). The resistivity results are shown in Fig. 4.14 , where on panel (a)
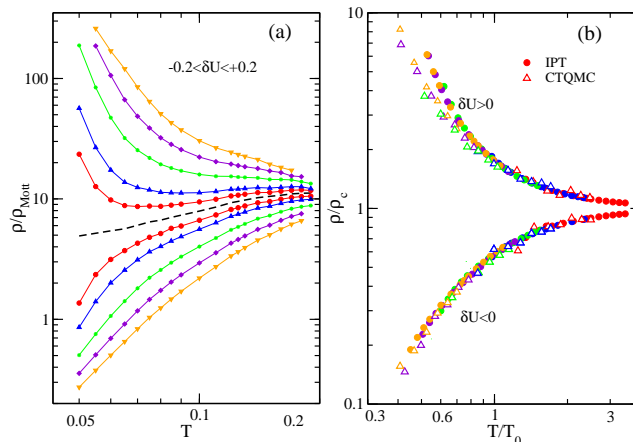
Figure 4.14: (Color online) (a) DMFT resistivity curves as function of temperature along different trajectories $-0.2 \leq \delta U \leq +0.2$ with respect to the instability line $\delta U = 0$ (black dashed line, see the text). Data are obtained using IPT impurity solver. (b) Resistivity scaling; essentially identical scaling functions are found from CTQMC (open symbols) and from IPT (closed symbols)

IPT resistivity data for $\delta U = 0, \pm 0.025, \pm 0.05, \pm 0.1, \pm 0.15, \pm 0.2$ in the temperature range of $T \approx 0.07 - 0.2$ are presented (CTQMC data are not shown for the sake of clarity of the figure). The resistivity is given in units of ρ_{Mott}, maximal resistivity according to the Boltzmann quasi-classical theory of transport [63]. The family of resistivity curves above ($\delta U > 0$) the "separatrix" $\rho_c(T)$ (dashed line, corresponding to $\delta U = 0$) has an insulating-like behavior, while metallic dependence is obtained for $\delta U < 0$.

According to the quantum critical scaling hypothesis (see section 2.2), our family of curves should satisfy the following scaling relation:

$$\rho(T, \delta U) = \rho_c(T) f(T/T_o(\delta U)). \tag{4.23}$$

We thus first divide each resistivity curve by the "separatrix" $\rho_c(T) = \rho(T, \delta U = 0)$ and then rescale the temperature, for each curve, with an appropriately chosen parameter $T_0(\delta U)$ to collapse our data onto two branches, Fig. 4.14b. Note that this unbiased analysis *does not assume* any specific form of $T_o(\delta U)$: it is determined for each curve simply to obtain optimum collapse of the data [80]. This puts us in a position to perform a stringent test of our scaling hypothesis: true quantum criticality corresponds to $T_o(\delta U)$ which vanishes at $\delta U = 0$ and displays power law scaling with the same exponents for both scaling branches. As seen in Fig. 4.15a T_0
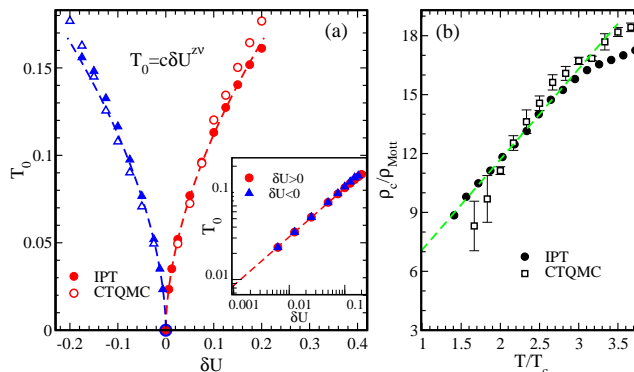
Figure 4.15: (Color online) (a) Scaling parameter $T_0(\delta U)$ as a function of control parameter $\delta U = U - U^\star$; the inset illustrates power-law dependence of scaling parameter $T_0 = c|\delta U|^{z\nu}$; (b) Resistivity $\rho_c(T)$ of the "separatrix". Excellent agreement is found between IPT (closed symbols) and CTQMC (open symbols) results.

falls sharply as $U = U^\star$ is approached, consistent with the QC scenario, but opposite to what is expected in a "classical" phase transition. The inset of Fig. 4.15a with log-log scale shows clearly a power-law behavior of $T_0 = c|\delta U|^{z\nu}$, with the estimated power $(z\nu)_{\delta U < 0}^{IPT} = 0.56 \pm 0.01$ for "metallic " side, and $(z\nu)_{\delta U > 0}^{IPT} = 0.57 \pm 0.01$ for an insulating branch.

We also find (Fig. 4.15b) a very unusual form of our critical resistivity $\rho_c(T)$, corresponding to the instability trajectory. Its values largely exceeds the Mott limit, yet it displays metallic-like but non-Fermi liquid-like temperature dependence $\rho_c(T) \sim T$. Such puzzling behavior, while inconsistent with any conventional transport mechanism, has been observed in several strongly correlated materials close to the Mott transition [63, 81]. Our results thus suggest that it represents a generic feature of Mott quantum criticality.

To specify the scaling behavior even more precisely, we compute the corresponding β-function [22] $\beta(g) = \frac{d \ln g}{d \ln T}$, with $g = \rho_c/\rho$ being the inverse resistivity scaling function. Remarkably (Fig. 4.16), it displays a nearly linear dependence on $\ln g$, and is continuous through $\delta U = 0$ indicating precisely the same form of the scaling function on both sides of the transition - another feature exactly of the form expected for genuine quantum criticality. This functional form is very natural for the insulating transport, as it is obtained even for simple activated behavior $\rho(T) \sim e^{-E_g/T}$. The fact that the same functional form *persists* well into the metallic side is a surprise, especially since it covers almost an order of magnitude for the resistivity ratio. Such a behavior has been interpreted [22] to reflect the "strong coupling" nature of the
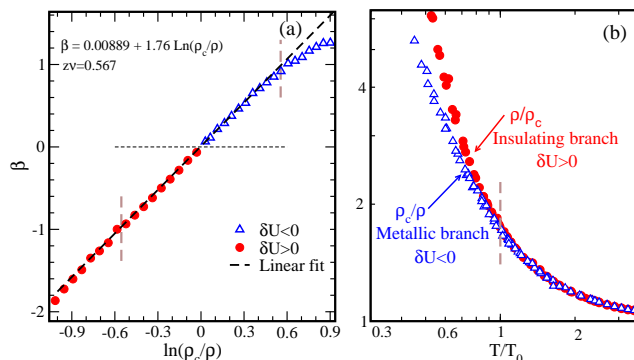
Figure 4.16: (Color online) (a) $\beta-$function shows linear in $\ln(\rho_c/\rho)$ behavior close to the transition. Open symbols are for metallic branch ($\delta U < 0$) and closed ones are for the insulating side ($\delta U > 0$) ; vertical dashed lines indicate the region where mirror symmetry of curves is found. (b) Reflection symmetry of scaled curves close to the transition.

critical point, which presumably is governed by the same physical processes that dominate the insulator. This points to the fact that our QC behavior has a strong coupling, i.e. non-perturbative character.
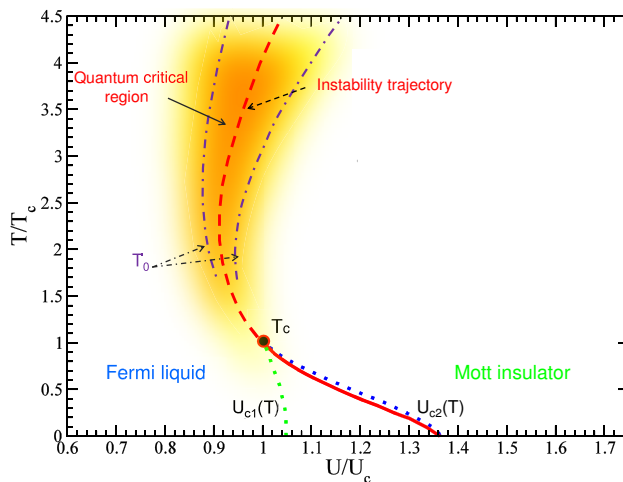

Figure 4.17: DMFT phase diagram of the fully frustrated half-filled Hubbard model. The thick dashed line, which extends at $T > T_c$ shows the "instability trajectory" $U^*(T)$, and the crossover temperature T_o delimits the QC region (dash-dotted lines).

The fact that the $\beta-$function assumes this logarithmic form on both sides of the transition is mathematically equivalent [22] to stating that the two branches of the corresponding scaling functions display "mirror symmetry" over the same resistivity range. Indeed, we find that transport in this QC region exhibits a surprisingly de-

veloped reflection symmetry (dashed vertical lines of Fig.4.17 mark its boundaries). Such a symmetry is clearly seen in Fig. 4.16b, where the resistivity ρ/ρ_c (for $\delta U > 0$) and conductivity $\sigma/\sigma_c = \rho_c/\rho$ ($\delta U < 0$) can be mapped onto each other by reflection with $\frac{\rho(\delta U)}{\rho_c} = \frac{\sigma(-\delta U)}{\sigma_c}$ [23]. Note that $T/T_o = 1$ sets the boundary of the quantum critical region, over which the reflection symmetry of scaled curves is observed. It is depicted by dash-dotted crossover lines T_0 on phase diagram of Fig. 4.17.

These remarkable features of the $\beta-$function, and the associated reflection-symmetry, have been observed earlier in experimental [82, 23] and theoretical [22] studies, which tentatively associated this with disorder-dominated MIT's. Speculation that $\beta \sim \ln g$ reveals disorder as the fundamental driving force for MIT, presumably reflects the fact that, historically, it has first been recognized for Anderson transitions [83]. Our work, however, shows that such behavior can be found even in absence of disorder - in interaction-driven MIT's. This finding calls for re-thinking of basic physical processes that can drive the MIT.

4.1.6.1 Scaling around the inflection points line

As stated in the previous section, the curvature λ must be directly related to an appropriate relaxation rate of a system perturbed away from the equilibrium, a quantity that in principle should be possible to measure on any system. However, it is currently very hard to make such measurements on the Mott systems and precisely determine the instability line. Our calculations, however, show that it lies just among the crossover lines that separate the bad metal and the Mott insulator, so it might not be necessary to know its exact position to observe quantum criticality. In the following, we present a scaling analysis that can be performed around the resistivity inflection points line (or any of the other crossover lines) to test the scaling hypothesis. As it turns out, the scaling is a robust feature, not particularly sensitive to the choice of $U_c(T)$.

We first observe that the resistivity curves display almost a perfect mirror symmetry when plotted on the log-scale (Fig. 4.14). This puts a strong constraint on the functional form of the scaling function f (as we show below) and also indicates that the resistivity curve along the inflection points line, $\partial \log \rho(U)/\partial U = 0$, could also serve as the separatrix. The mirror symmetry requires that

$$f(y) = 1/f(-y). \tag{4.24}$$

For the above to be satisfied, the function f must be of the form

$$f(y) = e^{h(y)}, \tag{4.25}$$

where h is an antisymmetric function of y. It is clear that $f(0) = 1$ and therefore $h(0) = 0$. h must also be smooth, so it can be represented as a Taylor series with only odd terms

$$h(y) = ay + by^3 + ... \tag{4.26}$$

In our calculations, it turns out that only the linear term is significant, and here we show how this can be tested. First we make a substitution of variables $T/\delta U^{z\nu} \rightarrow \delta U T^{-1/z\nu}$ and then take the logarithm of both sides of the scaling formula to obtain

$$\log\left(\frac{\rho(U_c(T) + \delta U, T)}{\rho(U_c(T), T)}\right) = \log(f(\delta U T^{-1/z\nu})). \tag{4.27}$$

If the mirror symmetry is satisfied, than

$$\log\left(\frac{\rho(U_c(T) + \delta U, T)}{\rho(U_c(T), T)}\right) = h(\delta U T^{-1/z\nu}), \tag{4.28}$$

which means that the precise form of $h(y)$ can be deduced by plotting the left-hand side of the above equation as a function of $y = \delta U T^{-1/z\nu}$ and than making a fit of a polynomial curve to the data. This is possible because in the region where the scaling formula is valid, all the data points should collapse onto a single curve. To test whether $h(y)$ is truly antisymmetric, it is convenient to first split it into symmetric and antisymmetric parts, $h(y) = h_s(y) + h_a(y)$, where $h_s(y) = \frac{1}{2}\left(h(y) + h(-y)\right)$ and $h_a(y) = \frac{1}{2}\left(h(y) - h(-y)\right)$. If the resistivity is mirror symmetric, h_s should be 0 and h_a should be equal to h. In Fig. 4.18 we plot these functions around the inflection point line and find h_s to be negligible. Also, it is easily seen that $h(y)$ is purely linear in the region where the data points perfectly collapse on a single curve.

Now it is clear that there are two conditions that $U_c(T)$ has to satisfy for the scaling with mirror symmetry to be possible. First, if we take the partial derivative over U at both sides of the equation, we get

$$\frac{\partial \log \rho(U, T)}{\partial U} = aT^{-\frac{1}{z\nu}} + b\delta U^2 T^{-\frac{3}{z\nu}} + ... \tag{4.29}$$

If $h(y)$ is a linear function, then only the first term in the above equation remains,
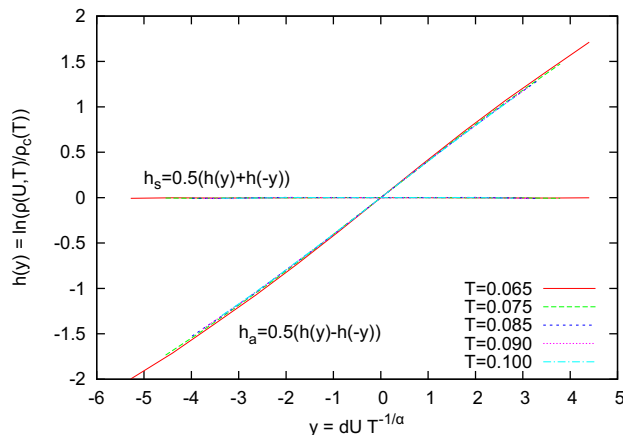
Figure 4.18: The symmetric and asymmetric part of scaling function, h_s and h_a at various temperatures. The small value of $h_s(y)$ shows that the mirror symmetry of resistivity curves is present. The $h_a(y)$ curves collapse around the inflection-point line which shows that the exponent, $z\nu = 0.953$, is well evaluated. Fitting a third order polynomial to $h_a(y)$ in the range where these curves collapse can reveal the exact form of the scaling formula. In our calculations only the linear term is significant.

which means that the logarithm of resistivity is a linear function of U in the entire region in which the scaling formula holds. Even if there are higher terms in $h(y)$, the above has to be true at least close to U_c (small δU), where the linear term is dominant in any case. This imposes a constraint on $U_c(T)$, such that it has to be in a region where the second derivative of logarithmic resistivity is zero, or at least small,

$$\frac{\partial^2 \log \rho(U, T)}{\partial U^2} \approx 0. \tag{4.30}$$

This derivative is color-coded in the (U, T) plane in Fig. 4.11 so that yellow color corresponds to a small absolute value. As it is readily verified, the above condition is not fulfilled anywhere exactly (except precisely at the $\log \rho(U)$ inflection point line by its definition), but all of the crossover lines lie in the region where this condition is approximately satisfied.

There is an additional requirement for $U_c(T)$ which is not in any way implied by definition of any of the crossover lines. Namely, the first derivative of the logarithmic resistivity has to be decreasing along $U_c(T)$ as a power law of temperature. This
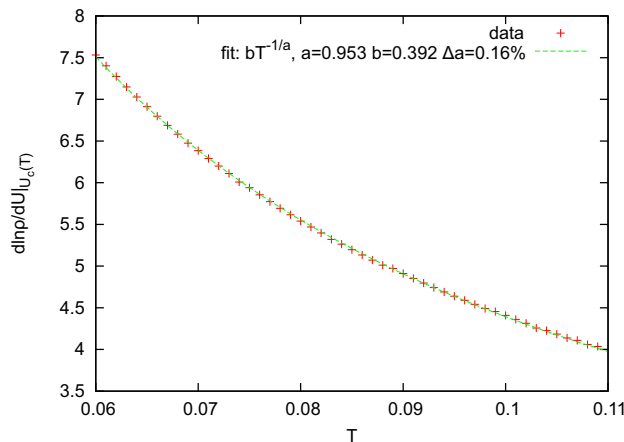
Figure 4.19: The derivative of resistivity with respect to U $(\partial\rho(U,T)/\partial U|_{U_{\text{infl}}})$ along the inflection-point line. Above roughly $2T_c$, it fits well to a power law curve of exponent -0.95. This can be used to evaluate the value of scaling formula exponent. At lower temperatures the decrease in resistivity is faster and the behavior deviates from the power-law and the scaling formula fails at temperatures below $2T_c$.

can be shown by taking the limit $\delta U \to 0$ in Eq. (4.29),

$$\left.\frac{\partial \log \rho(U,T)}{\partial U}\right|_{U_c} \propto T^{-\frac{1}{z\nu}}. \tag{4.31}$$

The above holds regardless of the value of the cubic (or any higher) term coefficient. One can even use this to give a good assessment of the exponent $z\nu$, by fitting such experimental (or theoretical) curve to a power law as shown in Fig. 4.19. As it is seen here, the derivative Eq. 4.31 calculated along the inflection point line fits well to a power law curve of exponent 0.95, but only above roughly $2T_c$. The same analysis of the IPT results yields a somewhat lower value $z\nu = 0.63$.

Finally, an estimate of how well the scaling works can be made by comparing the value of resistivity obtained by the scaling formula and the one measured in experiment or, as it is in our case, calculated from the DMFT solution. In Fig. 4.20 it is shown how the scaling formula works within the 5% error bar in a large region, for the inflection point line. This result is qualitatively the same for the other crossover lines. It is important to note that in the case of instability line (and all the other crossover lines other than the inflection point line), one is able to improve the quality of scaling by using different exponents $z\nu$ depending on sign(δU), and that way compensate for the lack of exact mirror symmetry. Also, when only the linear term in $h(y)$ is used, slightly lowering the value of $z\nu$ obtained from the
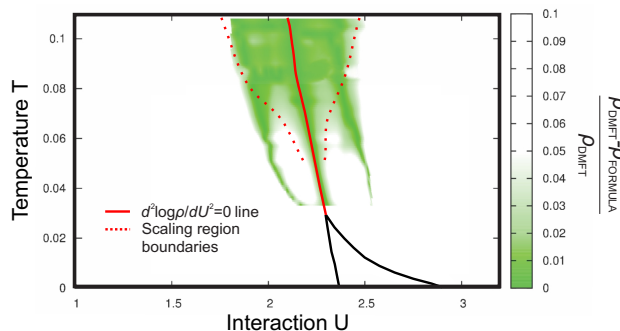
106

Figure 4.20: Relative error of the scaling formula color-coded in the $U - T$ plane. The dotted lines are the boundary of the scaling region. Two green filaments below $2T_c$ are where the scaling formula intersects with the actual DMFT result.

power-law fitting procedure typically broadens the region of validity of such scaling formula.

In conclusion, the $\log \rho(U)$ inflection points line is easily observable in experiment and our calculations show that it lies very close to the instability line. The analysis presented here, indicates that the quantum critical scaling previously found to hold around the instability line, should also be observable around the inflection point line. We show that the scaling formula valid around this line displays almost a perfect mirror symmetry of resistivity curves. In general, mirror symmetry, or "duality", should not be considered a necessary ingredient for a quantum critical scaling. In fact, we find that the scaling is of better quality around the instability line, although it is slightly less symmetric.

It is also very important to examine how the resistivity changes along the separatrix and our results are presented in Fig. 4.21. In this crossover region, the resistivity far exceeds the Mott limit and is only weakly dependent on temperature. We find that along the instability line, the resistivity is roughly a linear, increasing function of T. Along the inflection points line and $\rho(T) = max$ lines, the resistivity is slowly decreasing. We note that these results, however, must be model specific. Above the critical end-point, the resistivity is strongly dependent on U, and a small change in the shape or position of these lines can cause a significant change in the temperature dependences of resistivity presented in Fig. 4.21.
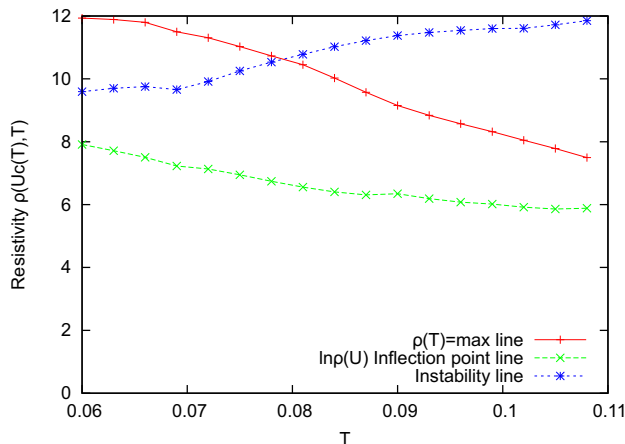
Figure 4.21: Resistivity (in units of ρ_{Mott}) along the crossover lines is weakly dependent on temperature and much larger than the Mott limit.

4.1.7 Comparison with experiments

Very recently, an extensive experimental investigation has been performed on several κ-organic systems, corroborating our results and illustrating the usefulness of our approach. In this section we present the most important results of this work Ref.[84] and compare it to our theoretical result.
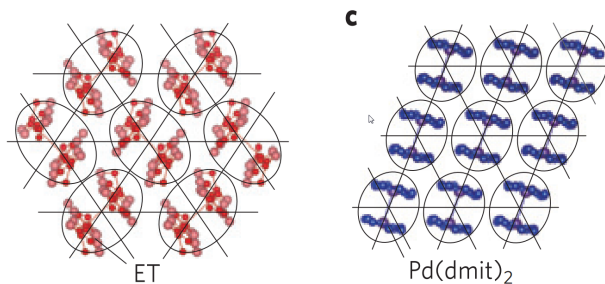
Figure 4.22: Illustration of the lattice structure of κ-organics. Two large molecules form a dimer and share a single electron with the valence band, thus making it effectively half-filled.

The samples used in this experiment are three types of quasi-two-dimensional organic Mott insulators with anisotropic triangular lattices, $\kappa - (ET)_2 Cu_2 (CN)_3$, $\kappa - (ET)_2 Cu[N(CN)_2]Cl$ and $EtMe_3 Sb[Pd(dmit)_2]_2$ (hereafter abbreviated to $\kappa - Cu_2(CN)_3$, $\kappa - Cl$ and $EtMe_3 Sb - dmit$, respectively), where ET and dmit represent bis(ethylenedithio)tetrathiafulvalene and 1,3-dithiole-2-thione-4,5-dithiolate, respectively (see Fig. 4.22 for a sketch of the lattice structure). In the Mott insulat-

ing phases, $\kappa - \mathrm{Cu_2(CN)_3}$ and $\mathrm{EtMe_3Sb - dmit}$ host quantum spin liquids (QSL's), whereas $\kappa - \mathrm{Cl}$ is an antiferromagnet (AFM). In the metallic phases, $\kappa - \mathrm{Cu_2(CN)_3}$ and $\kappa - \mathrm{Cl}$ are superconducting (SC) at low temperatures, whereas $\mathrm{EtMe_3Sb - dmit}$ remains a paramagnetic metal (PM). Then, the three systems have different types of Mott transition at $T = 0$ - QSL-SC, AFM-SC and QSL-PM transitions respectively. Clear first-order Mott transitions are observed in $\kappa - \mathrm{Cu_2(CN)_3}$ and $\kappa - \mathrm{Cl}$ up to Tc values of 20K and 38K, respectively, whereas there is no clear first-order nature in the Mott transition in $\mathrm{EtMe_3Sb - dmit}$; its critical temperature, if any, is well below 30 K. The critical temperatures of the three compounds are two or three orders of magnitude lower than the values of W (bandwidth) and the estimate for on-site interaction energy U, which are several thousand Kelvin or more.
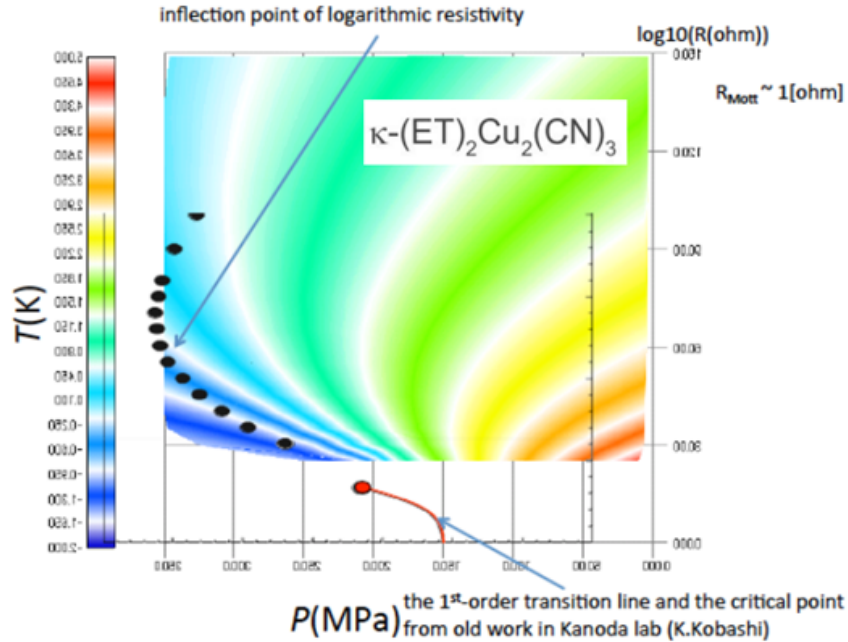
Figure 4.23: The shape of iso-resistive curves is strikingly similar to the theoretical result (see Fig. 4.2) [85].

The resistivity was measured throughout the phase diagram by varying pressure and temperature (Fig. 4.23). In practice, temperature was held fixed, while the controlled He-gas pressure P was varied continuously. The inflection point in $\log \rho$ is clearly observed in all samples (Fig. 4.25) and a wide range of temperature, so the authors performed the analysis analogous to the one presented in section 4.1.6.1. In Fig. 4.24 (taken from Ref.[84]), an example of normalized resistivity $\tilde{\rho} = \rho / \rho_c(T)$
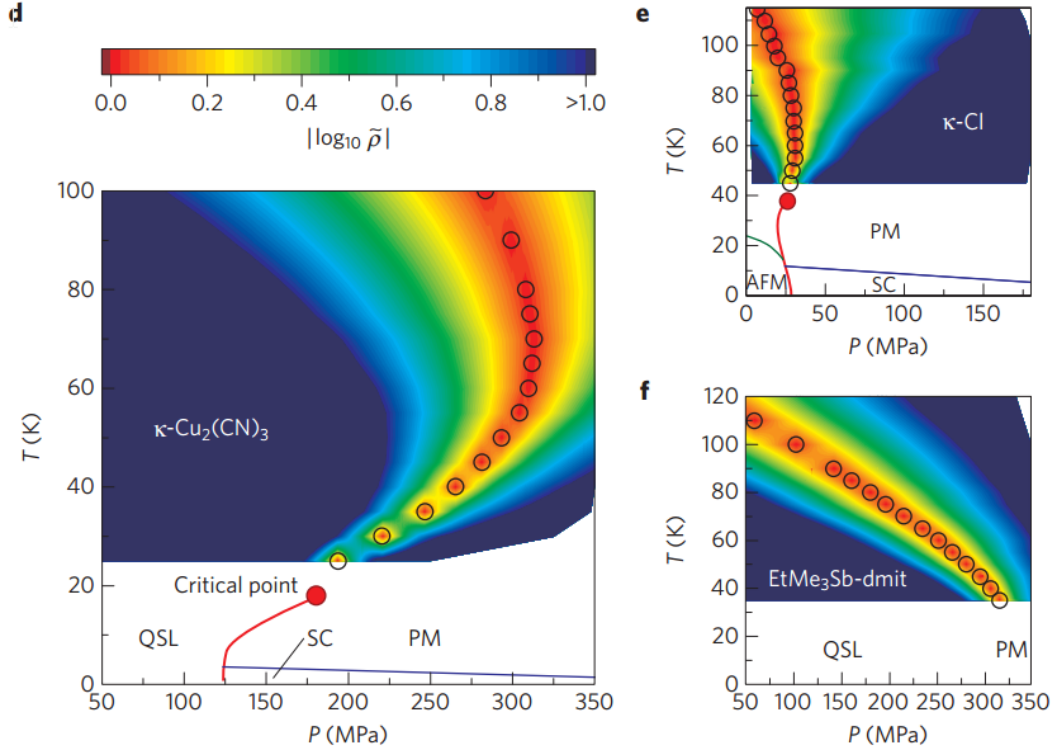
Figure 4.24: Curves of constant $\tilde{\rho}(P,T) = \rho(P,T)/\rho_c(T)$ spread out in an obviously power-law fashion, which is immediately suggestive of quantum-critical behavior [84].
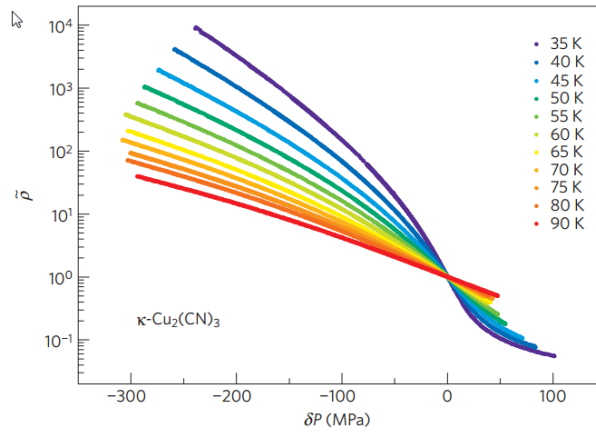
Figure 4.25: Inflection point in logarithmic resistivity is always observed in a wide range of temperature and is used as the quantum Widom line in the scaling analysis [84].

is shown as a function of pressure at various temperatures. The collapsed data points are shown in Fig. 4.26. The quality of the scaling and prominence of mirror symmetry in all three materials suggests there is a universal high-temperature behavior in connection with the Mott transition which stems from the essentially quantum nature of the transition, i.e. these materials obviously feature two distinct ground states depending on the pressure, and these must be ultimately separated by a purely quantum phase transition.
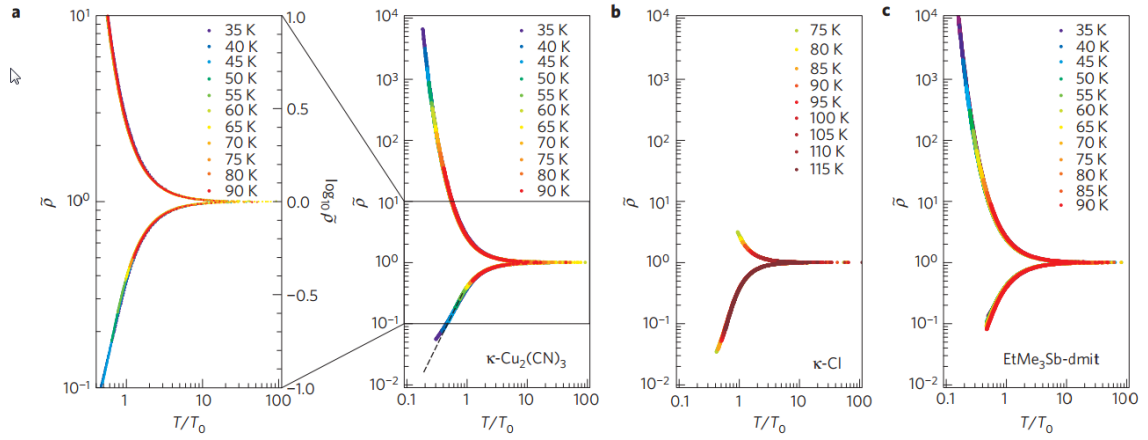
Figure 4.26: In all three materials, resistivity data points collapse on two branches, in agreement with the scaling hypothesis [84].

4.2 Doping-driven Mott MIT

At half-filling, strong enough on-site interaction U opens a spectral gap at the Fermi level and produces the Mott insulating state [24]. However, the Mott insulator can be destroyed by adding electrons to the system, i.e raising the chemical potential μ. When μ reaches the upper Hubbard band, the system is once again conducting [86]. Similarly to the interaction-driven MIT, here the transition is of the first order up to some T_c, and is a smooth crossover at $T > T_c$.

In this section we consider a single-band Hubbard model defined by the Hamiltonian

$$H = -t \sum_{\langle i,j \rangle, \sigma} \left(c_{i\sigma}^\dagger c_{j\sigma} + \text{h.c.} \right) + U \sum_i n_{i\uparrow} n_{i\downarrow} - \mu \sum_{i,\sigma} c_{i\sigma}^\dagger c_{i\sigma},$$

and μ denotes the chemical potential. We solve the DMFT equations using the hybridization-expansion continuous time quantum Monte Carlo (CTQMC) algorithm for the impurity solver [57, 58, 49] (see section 3.4.1). We fix U at some large value $U = 3.2, 4.0$, such that at half-filling system is a Mott insulator, and then vary the chemical potential and temperature to scan the phase diagram. Note that the Hubbard model on a particle-hole symmetric lattice (as is the Bethe lattice or the fully connected lattice) is invariant under $t \longrightarrow -t$ and $\tilde{\mu} \equiv \mu - U/2 \longrightarrow -\tilde{\mu}$. Therefore, we only need consider the electron doped case, and all the conclusions hold for the hole doped case as well. For the Green's function this means $\text{Im} G_{\tilde{\mu}}(\omega) = \text{Im} G_{-\tilde{\mu}}(-\omega)$, or more precisely $G_{\tilde{\mu}}(\omega) = -G_{-\tilde{\mu}}^*(-\omega)$, $G_{\tilde{\mu}}(i\omega_n) = -G_{-\tilde{\mu}}^*(i\omega_n)$, while the optical conductivity $\sigma(\omega)$ remains the same regardless of the sign of $\tilde{\mu}$.

4.2.1 Phase Diagram

At low-temperature the Mott transition is observed as the first order transition, and features a pronounced jump in the value of resistivity and other quantities [87]. Around the first order transition line, a small coexistence region is present, where both metallic and insulating phases are locally stable. Our calculations show that the critical end-point temperature $T_c(U)$ for the doping-driven transition rapidly drops with increasing interaction, and at $U = 4$ it already is less than 10% of that at half-filling. This is illustrated in Fig. 4.27a. At the critical end-point (red dots) the two solutions merge, and above it no true distinction between the phases exists; only a rapid crossover is observed upon variation of U or μ. For a more detailed
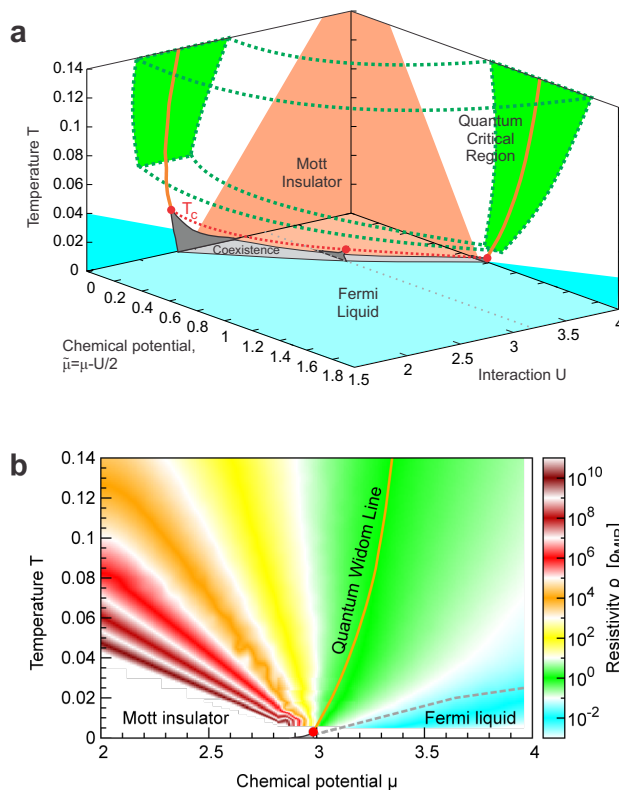
Figure 4.27: (a) Phase diagram of the maximally frustrated Hubbard model. The quantum critical scaling is observed in the green region which extends to lower temperatures as T_c (red dots) is reduced. (b) Color plot of the resistivity in the $\mu - T$ plane for $U = 4$. The quantum Widom line (see text) passes through the crossover region where the resistivity is around the MIR limit. The coexistence region (gray) is barely visible on the scale of this plot.

discussion of the coexistence region and $T_c(U)$ dependence see the next section.

In Fig. 4.27b, we color-code the resistivity in the (μ, T) plane, calculated for $U = 4$. The resistivity is given in units of the Mott-Ioffe-Regel limit ρ_{MIR} which is defined as the highest possible resistivity in a Boltzmann semi-classical metal, corresponding to the scattering length of one lattice spacing. Numerical value for ρ_{MIR} is taken consistently with Ref. [45]. At $\mu = U/2$ the system is half-filled. At approximately $\mu = U - D = 3$, the Fermi level enters the upper Hubbard band, and a first-order doping-driven MIT is observed at temperatures below $T_c = 0.003D$. While the chemical potential is within the gap, a clear activation behavior, $\rho \sim e^{E_g/T}$, is found at low temperatures. On the metallic side of the MIT, due to the strong electron-electron scattering, the resistivity grows rapidly with temperature, and typical Fermi-liquid behavior is observed only below rather low coherence temperature

T_{FL} (denoted with the gray dashed line).

4.2.2 T_c and the coexistence region

The first order phase transition is most easily observed by looking at the occupation number. At very low temperature, while the chemical potential is within the spectral gap, filling is roughly a constant, i.e. $n(\mu) \approx 0.5$. When the chemical potential reaches the upper Hubbard band, a quasi particle peak forms abruptly at its lower edge causing an immediate transfer of spectral weight from the lower Hubbard band to the vicinity of the Fermi level [24, 88]. This is observed as a jump in the occupancy from nearly half-filling to around 2-3% doping. An insulating solution is not possible when μ is in the upper Hubbard band, hence its bottom edge determines the insulating (right) spinodal. However, a metallic solution is possible even when μ is in the gap. This type of state features an in-gap quasi-particle peak [89] and is observed in the coexistence region. The lowest value of the chemical potential at which the quasi particle peak can survive constitutes the metallic (left) spinodal, and this one is strongly temperature dependent. The disappearance of the QP peak at the metallic spinodal is also abrupt, and occurs at finite doping. Therefore, there is a range of doping that is not achievable locally at any value of the chemical potential, but only globally through phase separation. With increasing temperature, the forbidden doping range shrinks and disappear together with the hysteresis loop, precisely at T_c [87, 90]. Note also, that the range of forbidden doping vanishes at $T = 0$ as well, where a metallic solution is possible even at infinitesimal doping [24], although in this case particle-hole symmetry is broken and $\mu \neq U/2$. In Fig. 4.28a,b we show the hysteresis curves of the occupancy for two values of interaction U. The position of spinodals and the width of the coexistence region are easily determined from the jumps in $n(\mu)$. We considered the lowest temperature at which no coexistence is observed to be the critical temperature. Note also that due to the numerical error of the CTQMC, some unphysical doping is observed in the insulating state at the lowest temperatures. We were not able to obtain physically meaningful results below $T \approx 0.0015$ and this is the lowest temperature at which we have found the method to be reliable. The numerical error from the CTQMC becomes significant at low temperature and a precise assessment of T_c's lower than ≈ 0.002 proves very difficult. The coexistence regions at the two values of U are shown in Fig.4.28c and d. The $T = 0$ position of the left spinodal is taken from the DMFT+ED (exact

114
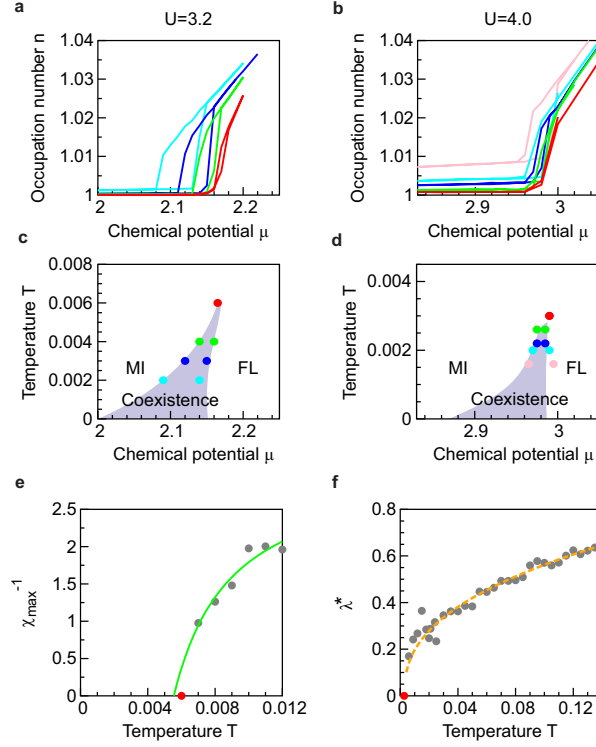
Figure 4.28: Coexistence region of the first-order doping-driven Mott metal-insulator transition can be determined in different ways. (a),(b),(c),(d) The position of spinodals can be determined from the jumps in the occupation number. In the co-existence region, two types of solution are possible, depending on the initial guess in the DMFT procedure. This is observed as a hysteresis loop in the occupation number and other quantities. (e),(f) Precisely at the critical point, physical quantities often have extremal values (zero or infinity). By extrapolating such quantities from higher temperatures, one can estimate the critical temperature. (e) The maxima of the inverse charge compressibility with respect to the chemical potential can be extrapolated to obtain a good estimate for T_c. (f) The values of λ along the instability line $\mu^*(T)$ become scattered and overestimated close to the critical point, due to numerical error from the CTQMC. This makes it unpractical to to use extrapolation of λ^* for estimation of T_c.

Figure 4.29: Critical temperature must go to zero as U is increased because there is no coexistence in the atomic limit.

diagonalization) calculation found in [89] and seems to fit our finite temperature results well.

A better understanding of why T_c is decreasing with U can be obtained by plotting the $T = 0$ phase diagram in a fashion more commonly utilized in the context of the bosonic Hubbard mod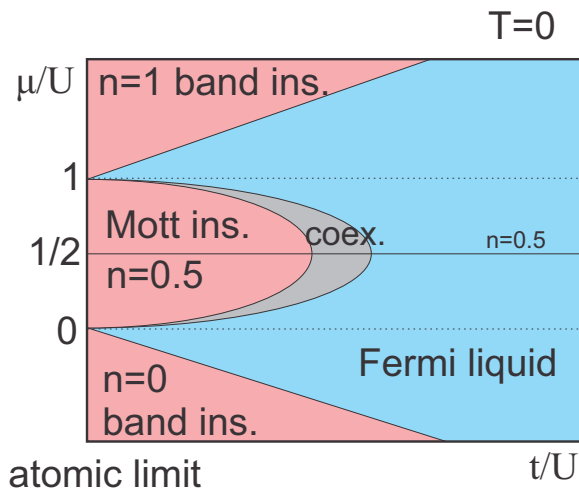el. On Fig. 4.29 we illustrate the phase diagram with t/U and μ/U on the axes. Here, $\mu/U = 1/2$ corresponds to half-filling, and $t/U = 0$ corresponds to the atomic limit. It is clear that there can be no coexistence in the atomic limit where the transition is trivial and corresponds to the band transition between the half-filled Mott and full (empty) band insulators (chemical potential is either below or above $|\uparrow\downarrow\rangle$ state).

4.2.2.1 T_c from the charge compressibility

The alternative way of determining T_c is by looking at the uniform charge susceptibility $\chi = \frac{\partial n}{\partial \mu}$. Precisely at the critical point, χ is divergent and above T_c, there is a line of maxima in $\chi(\mu)|_T$. Furthermore, it can be shown [91] that close to the critical point $\chi^{-1} \sim \frac{T-T_c}{a+b(T-T_c)}$. This is useful as one can extrapolate the values of $\chi_{\max}^{-1}(T)$ to lower temperatures and see where it goes to zero. However, such method is of inferior accuracy compared to the direct observation of the coexistence, and we use it only for cross-checking of our results. In Fig. 4.28e we show such calculation in the case of $U = 3.2$.

4.2.2.2 T_c from the λ analysis

In Figure 4.28f we plot the values of λ along the instability line (see the next Section). Close to the the critical point, it is very difficult to make a precise estimate of the DMFT convergence rate, as high convergence is not achievable at all. The low temperature values are therefore much more scattered and systematically overestimated. Although in principle one could estimate T_c from higher temperatures by extrapolating $\lambda^*(T) \equiv \lambda(\mu^*(T), T)$, the numerical noise makes such a method very impractical. Further difficulty lies in the possibility of $\lambda^*(T)$ changing trend before going to zero, which introduces additional systematic error to the estimate of T_c.

4.2.3 λ-analysis and the instability line

In section 4.1.5, we have discussed a possible generalization of the Widom line (originally defined in the context of classical liquid-gas transitions [76]), to strictly zero-temperature (quantum) phase transitions. The most natural way of defining such a quantum Widom line is by looking at the free-energy landscape around the ground state of the system, as it is well defined in all physical models. Regardless of the specifics of the phase transition, precisely at the critical point, the free energy minimum is flat, i.e. its curvature λ is zero. At higher temperatures, this leads to a line of minima in λ with respect to the parameter that is driving the transition (at half-filling we had $\frac{\partial \lambda}{\partial U}\big|_T = 0$). It is at those minima that the fluctuations are most pronounced - the system is "equally close" to the two competing phases and thus the least stable. Now we utilize this concept in the case of doping-driven Mott transition, and at each temperature search for the minimum value of λ with respect to the chemical potential.

In practice, we calculate λ by monitoring the convergence rate of the iterative DMFT procedure. Given the model parameters, the free energy functional $\mathcal{F}_{U,T,\mu}[G(i\omega_n)]$ yields a smooth manifold in the Hilbert space of the Green's functions. Being Taylor expandable, the local environment of any free-energy minimum has to be parabolic. Thus, in the advanced stage of the DMFT procedure, i.e. close to the self-consistent solution, a steady, exponential convergence should be observed. The curvature λ is then directly related to the exponent of the functional dependence of the difference between the consecutive solutions versus the iteration index. When determining the convergence rate, however, it is not always sufficient to look at the Green's function in only the lowest Matsubara frequency, and one must use

the generalized Raileigh-Ritz (RR) formula [92]

$$\lambda_i = 1 - \sum_n \frac{|G_n^{i+1} - G_n^i||G_n^i - G_n^{i-1}|}{|G_n^{i+1} - G_n^i|^2}, \qquad (4.32)$$

where i stands for the iteration index, and ideally, $\lambda = \lim_{i \to \infty} \lambda_i$. However, the highest achievable level of convergence is determined by the amount of statistical noise in the CTQMC result, and when it is reached, $G(i\omega_n)$ just fluctuates around the self-consistent solution, and no further convergence is observed. Especially near the critical point, CTQMC error becomes substantial and a high convergence can not be reached at all. Here, typically only a few iterations are available for the estimation of λ as most of the parabolic region is below the level of numerical noise, and one must look carefully for the range of iterations in which a steady exponential convergence is observed.

The result presented with gray dots in Fig. 4.30a is obtained by employing the RR formula from equation (4.32) at each iteration i, and then taking the average over the set of 5 consecutive iterations that shows the least variance, i.e. the one corresponding to the period of the steadiest exponential convergence.

Away from half-filling, however, there are additional difficulties. Namely, $G(i\omega_n)$ is complex, which means that it has additional degrees of freedom as compared to its purely imaginary analogue at particle-hole symmetry. Thus, the fluctuations encountered in the convergence rate of $G(i\omega_n)$ are more severe, and the λ-analysis is harder to perform compared to the half-filled case. This is why the data points presented with gray dots in Fig. 4.30 exhibit considerable scattering, but the overall trend is still rather obvious. In all of the calculations regarding the quantum critical (QC) scaling analysis, we use the smooth fit (orange dashed line) as the instability line and denote it with $\mu^*(T)$. Note that no other smoothing has been performed on the data, and all the minima are estimated automatically from the raw λ results. Although there are considerable error bars on each $\mu^*(T)$ value, the high resolution in temperature increases the certainty of the result.

It is interesting that $\mu^*(T)$ is very close to the line of maxima of the second derivative of the occupation number versus the chemical potential, $\frac{\partial^2 n}{\partial \mu^2}\big|_T = \max$. This is the place where $n(\mu)$ changes trend, and as expected, the instability line separates the metallic-like and insulating-like behavior on the phase diagram. Also note that $\mu^*(T)$ roughly follows an iso-resistive curve and so the resistivity does

not change considerably along the instability line. At $T > 0.08$ ρ^* is found to be constant and equal to the Mott-Ioffe-Regel (MIR) limit. Above $T = 0.14$, λ-analysis can not give reliable results as the minimum in $\lambda(\mu)|_T$ becomes very shallow, i.e. of depth comparable to the level of numerical noise. Throughout the following sections we extrapolate the instability line to high temperatures $T > 0.14$ by imposing the criterion $\rho^* = \rho_{\mathrm{MIR}}$. Also note that at very low temperature, the actual form of $\rho(\mu^*(T), T)$ depends strongly on the precise values of $\mu^*(T)$ because, in this region, the resistivity changes rapidly with the chemical potential.

4.2.4 Analytical continuation and calculation of resistivity

The straightforward application of the maximum entropy method (MEM) [59, 93] for analytical continuation of the Green's function can in some cases lead to unphysical results. In the metallic phase, this method tends to overestimate the height of the quasi-particle (QP) peak in the single-particle energy spectrum given by $-\frac{1}{\pi}\mathrm{Im}G(\omega + i0^+)$. Sometimes in those cases, the imaginary part of the self-energy falsely goes to zero at several frequencies (usually two or four), yielding an unphysical vanishing DC resistivity. Given the analytically continued Green's function on the real axis, the self-energy is obtained from the DMFT self-consistency condition

$$\Sigma(\omega) = \omega + \mu - G^{-1}(\omega) - t^2 G(\omega), \qquad (4.33)$$

and the imaginary part of the above equation reads

$$\mathrm{Im}\Sigma(\omega) = \mathrm{Im}G(\omega)(|G(\omega)|^{-2} - t^2). \qquad (4.34)$$

It is immediately obvious that $|G(\omega)| = 1/t$ yields $\mathrm{Im}\Sigma(\omega) = 0$, at any frequency. When there is an unphysical excess of QP weight, precisely this is seen, usually at the edges of the QP peak. This makes the conductivity integral divergent and the DC resistivity exactly zero.

We find that much better results are obtained by performing MEM on the spectral function

$$A(\varepsilon, i\omega_n) = \frac{1}{i\omega_n + \mu - \varepsilon - \Sigma(i\omega_n)}. \qquad (4.35)$$
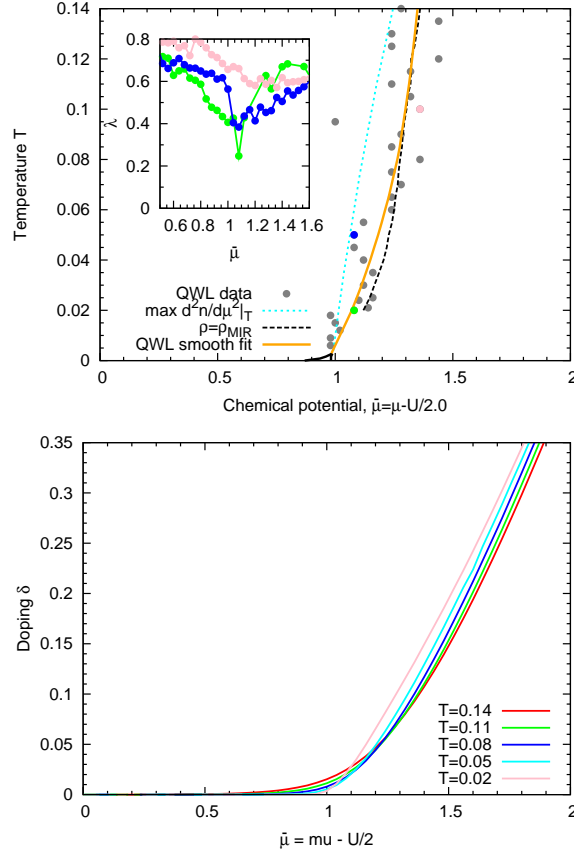
Figure 4.30: The instability line $\mu^*(T)$ (orange dashed) corresponds to the minima in $\lambda(\mu)|_T$, which is related to the convergence rate of the DMFT loop. (a) The precision of λ results is limited by the statistical noise in CTQMC. However, the minima in $\lambda(\mu)|_T$ are still clearly present, and $\mu^*(T)$ can be determined with satisfactory accuracy. At high temperature, QWL is found to coincide with the iso-resistive curve of the MIR limit (black dashed), which is then used to extrapolate the QWL to temperatures above $T = 0.14$, where λ-analysis is no longer reliable. (b) The QWL is also very close to the point where occupancy $n(\mu)|_T$ changes trend, i.e. has a maximum of the second derivative. The line of maxima in $d^2n/d\mu^2|_T$ can also be considered a crossover line between metallic and insulating behavior (light blue dotted line on panel (a)).

Figure 4.31: Evolution of the density of states with increasing temperature. At low temperature there is a clear quasiparticle peak in the density of states. The quasiparticle peak gradually disappears in the bad metal regime which is centered around the QWL. The orange line is the density of states at the QWL. The data are shown for the fixed chemical potential $\mu = 3.5$ and $U = 4$, which corresponds to roughly 15 % doping.
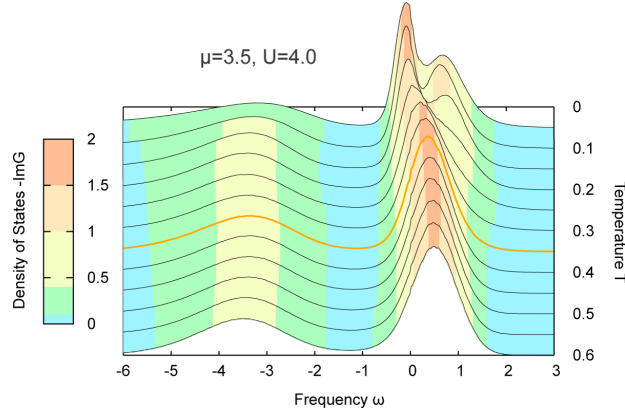
The self-energy is then easily extracted from the real-axis result

$$\Sigma(\varepsilon; \omega) = \omega + \mu - \varepsilon - A^{-1}(\varepsilon, \omega). \tag{4.36}$$

This procedure should in principle yield the same self-energy for any value of ε, but in practice this is not found to be the case. However, a good estimate of $\Sigma(\omega)$ is obtained by averaging the results of each continuation, i.e.

$$\Sigma(\omega) = \frac{1}{N} \sum_{i=1}^{N} \Sigma(\varepsilon_i; \omega). \tag{4.37}$$

Similarly, one could first calculate the Green's function

$$G(\omega) = \int d\varepsilon \rho_0(\varepsilon) A(\varepsilon, \omega) \tag{4.38}$$

and then get the self-energy from the DMFT self-consistency. In practice, we have used 40 values of ε, equally spaced within the energy range of the non-interacting band, and found that the systematic and numerical error of MEM gets canceled by the averaging. We have found that in this approach, physically meaningful solutions are always obtained, results are more consistent and have less numerical noise, but at the expense of performing a much larger number of analytical continuations.
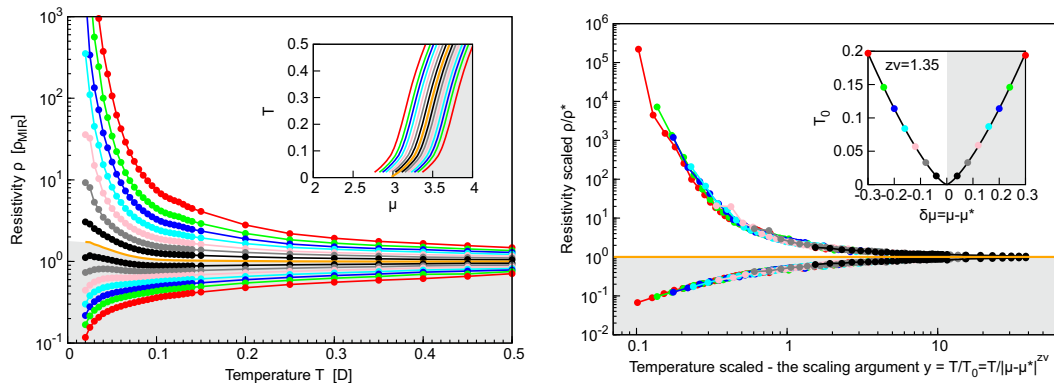
Figure 4.32: (a) Family of resistivity curves calculated along lines parallel to the QWL (orange). (b) Upon rescaling the temperature with adequately chosen parameter T_0, the resistivity curves collapse and reveal mirror symmetry of metallic-like and insulating-like behavior around the QWL. T_0 depends on the distance from the QWL as $T_o(d\mu) \sim d\mu^{z\nu}$, with $z\nu \approx 1.35$.

Where available, we cross-checked our results with the findings in Ref. [45] where the analytical continuation is performed via Pade approximant on the high-precision CTQMC data, and found very good agreement.

4.2.5 QC scaling tests

We carried out a careful *λ-analysis* for the doped Mott insulator (see section 4.1.5.2), and we display the resulting QWL trajectory $\mu^*(T)$ as an orange line in all plots (throughout the following, an asterisk in the superscript indicates physical quantities evaluated along the QWL; e.g. $\rho^*(T)$ is resistivity calculated at temperature T at $\mu = \mu^*(T)$). The QWL, separating the metallic-like and the insulating-like behavior, marks the center of the corresponding QC region, where the resistivity curves are expected to display the scaling behavior of the form

$$\rho(\mu, T) = \rho^*(T)F(T/T_0(d\mu)). \tag{4.39}$$

Here the parameter T_0 should assume power law dependence on the deviation from the QWL: $T_o(d\mu) \sim d\mu^{z\nu}$, with $d\mu = \mu - \mu^*(T)$.

   To check validity of the scaling hypothesis Eq. (4.39), we calculate the resistivity along the lines parallel to the QWL, as shown in Fig. 4.32a. We find that the resistivity shows very weak temperature dependence along the QWL. In particular, above $T = 0.08$ it follows the line of constant resistivity *which coincides* with the

MIR limit, $\rho^*(T > 0.08) = \rho_{\mathrm{MIR}}$ (in contrast to the behavior previously established at half-filling where $\rho \gg \rho_{\mathrm{MIR}}$ along the QWL). In fact, all curves converge *precisely* to the MIR limit at high temperatures, suggesting its fundamental role in characterizing the metal-insulator crossover for doped Mott insulators. The curves also display the characteristic "bifurcation" upon reducing temperature, and a clear change in trend upon crossing the QWL. The scaling analysis confirms that all the curves indeed display fundamentally the same functional dependence on temperature, and that they all can be collapsed onto two distinct branches of the corresponding scaling function (Fig. 4.32b). The scaling exponent has been estimated to be $z\nu \approx 1.35 \pm 0.1$ for both branches of the scaling function, which display mirror-symmetry [22] over almost two decades in T/T_0, and the scaling covers more than three orders of magnitude in resistivity. The QC region (green in Fig. 4.27a) spreads above the critical end-point (red points and dotted line) and extends to lower temperatures as T_c is reduced.

4.2.5.1   Boundaries of the QC scaling region

The explicit form of the scaling function can be obtained by considering the following (equivalent) form of the scaling equation

$$\rho(\mu, T) = \rho^*(T)\tilde{F}\left(\frac{d\mu}{T^{1/z\nu}}\right). \tag{4.40}$$

with the advantage of $\tilde{F}(x)$ being a smooth analytical function in x. Then, the scaling function $\tilde{F}(x)$ can be obtained by plotting the DMFT resistivity data versus the argument $x = \frac{d\mu}{T^{1/z\nu}}$ and performing a numerical fit. This is shown in Figure 4.33a. $\tilde{F}(x)$ is approximately linear on the logarithmic scale which implies that $\tilde{F}(x) \approx 10^{Bx}$, where $B \approx -0.33$. This analytical form is consistent with the mirror symmetry of the scaling formula near the QWL, $\tilde{F}(x) = 1/\tilde{F}(-x)$. We can see that the scaling region goes beyond the mirror symmetry of the scaled resistivity curves, especially on the metallic side of the QC region.

   The scaling region can be estimated from the color plot of the relative error $r = |\rho_{DMFT} - 10^{Bx}|/\rho_{DMFT}$, which is shown in Figure 4.33b, analogously to the Fig. 4.20. The boundaries of the QC scaling region defined by $r < 10\%$ are shown with gray dashed lines and correspond to the values $x_{\min} = -1.0$ and $x_{\max} = 1.5$. Note that they coincide with the $\mu = 3.0$ line (red dashed; it corresponds to chemical
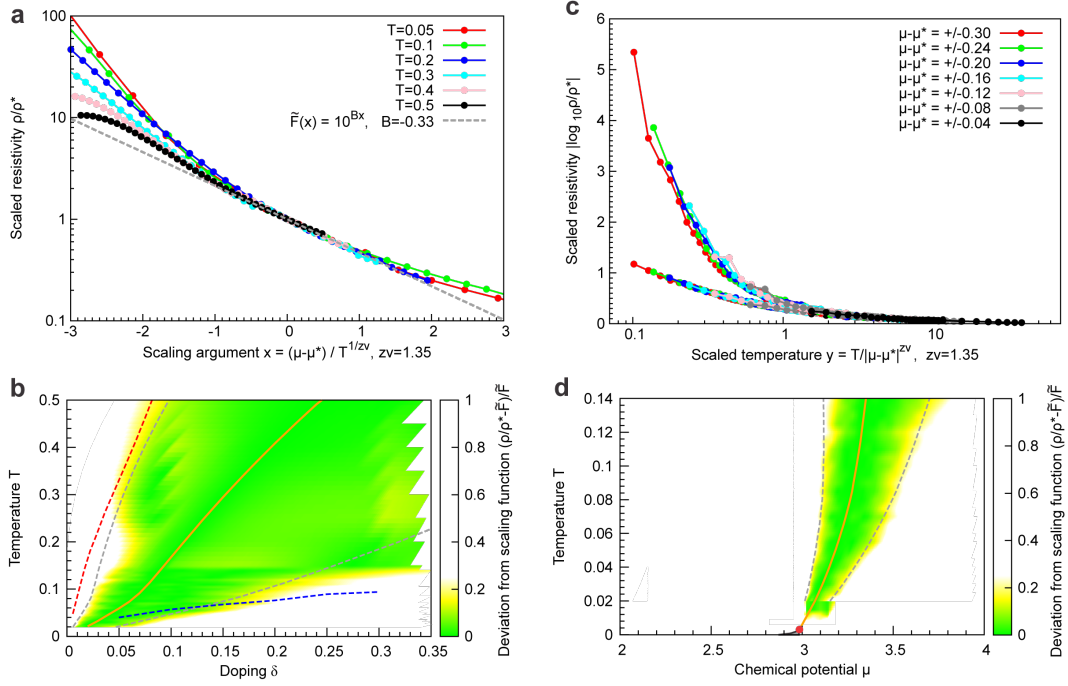
Figure 4.33: The extent of the scaling region.(a) The DMFT data are plotted as a function of the scaling argument x to obtain a fit for the scaling function. The range of x where DMFT data points fall on a single, well defined curve can be used as an estimate of the scaling region. (b) Between $x = -1.0$ and $x = 1.5$ (gray dashed lines), the relative error of the scaling formula is below 10%. The boundaries of the scaling region coincide with the $\mu = 3.0$ line (dashed red) and the knee-like feature in resistivity $\rho(T)|_\delta$ which marks the boundary of the linear resistivity bad metal region (blue line). (c) The mirror symmetry is found where the two branches of $|\log F(y)|$ coincide. (d) The scaling region in the $\mu - T$ plane; the scaling is valid for $T \gtrsim 4T_c$.

potential being at the lower edge of the upper Hubbard band), and the knee-like feature in $\rho(T)|_\delta$ curves (blue dashed; it corresponds to the boundary of the linear resistivity bad metal region). It is obvious from this plot that the QC scaling region completely matches the region of typically bad metallic temperature dependence of the resistivity (see next section).

The boundaries of the QC scaling region can alternatively be estimated simply by looking at Fig. 4.33a and observing the maximum and minimum values of x for which the DMFT results fall on a single well defined curve. This yields $x_{\min} = -1.0$ and $x_{\max} = 1.5$. These lines are also shown in Fig. 4.33b (gray dashed) and are in good agreement with the independent estimate based on relative error r.

Finally, the region of mirror-symmetry can be estimated by plotting the DMFT resistivity data $|\log \frac{\rho}{\rho^*}|$ as a function of $y = T/d\mu^{z\nu}$ (shown in Fig. 4.33c) and observing the lowest y at which the two branches of data are found to coincide. This analysis yields $y_{\min} = 1 = |x_{\min/\max}|^{-1}$, in agreement with other approaches.

4.2.6 Connection with bad metal behavior

We demonstrated the emergence of clearly defined quantum critical behavior through an analysis of the (μ, T) phase diagram, with $d\mu = \mu - \mu^*$ as the scaling parameter. From the experimental point of view it is, however, crucial to identify the corresponding QC region in the (δ, T) plane and understand its implications for the form of the resistivity curves for fixed level of doping $\rho(T)|_\delta$. By performing a careful calculation of the $\delta(\mu, T)$ dependence (see Fig. 4.34), it is straightforward to re-plot our phase diagram and resistivity curves in the (δ, T) plane. Remarkably, we find that the quantum critical scaling region covers a broad range of temperatures and dopings, and almost perfectly matches the region of the well-known bad metal transport [94, 45], characterized by the absence of long-lived quasiparticles and linear $\rho(T)|_\delta$ curves. We first analyze the (δ, T) phase diagram in detail, and then establish a connection between the slope of $\rho(T)|_\delta$ curves in the bad metal regime and the QC scaling exponent νz.

In Fig. 4.35a we show the phase diagram of the doped Mott insulator. At $T = 0$, the Mott insulator phase is found exclusively at zero doping. At low enough temperature and finite doping, characteristic Fermi liquid behavior is always observed. Here, the resistivity is quadratic in temperature, while a clear Drude peak is observed at low frequencies in optical conductivity and density of states (see Fig. 4.31).
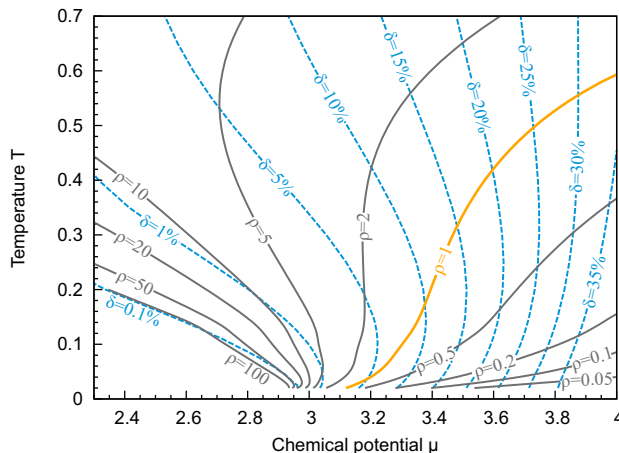
Figure 4.34: Lines of constant doping intersect with the QWL (orange), along which the resistivity is equal to the MIR limit ρ_{MIR}. As temperature is increased at a fixed level of doping, one moves from the metallic to the insulating side of the transition.

The coherence temperature T_{FL} is found to be proportional to the amount of doping δ, however with a small prefactor of about 0.1, in agreement with Refs. [86, 45]. In a certain temperature range above T_{FL}, a Drude peak is still present as well as the quasiparticle resonance in the single-particle density of states, but the resistivity no longer follows the FL T^2 dependence. This corresponds to the "Resilient Quasiparticle" (RQP) transport regime, which was carefully examined in Ref. [45]. At even higher temperatures, the temperature-dependent resistivity at fixed doping $\rho(T)|_\delta$ enters a prolonged linear regime (see Fig. 4.35b) [95], which is accompanied by the eventual disappearance of the Drude peak around the MIR limit. This behavior is usually referred to as the Bad Metal regime [45]. The resistivity is comparable to the MIR limit throughout the BM region, and the QWL (as determined from our thermodynamic analysis) passes through its middle.

The region of linear $\rho(T)|_\delta$ dependence is found to be completely encompassed by the QC scaling region between the dashed lines on Fig. 4.35a (see previous section). We therefore expect that the emergence of the linear-T dependence of the resistivity, as well as the doping dependence of its slope, should be directly related to the precise form of the corresponding scaling function. Indeed, at high temperature and close to the QWL, the argument of the scaling function $x = d\mu/T^{1/z\nu}$ is always small (due to the $T^{1/z\nu}$ factor in the denominator), and the scaling function can be linearized, viz.

$$\tilde{F}(x) \approx 1 + Ax + \cdots \tag{4.41}$$
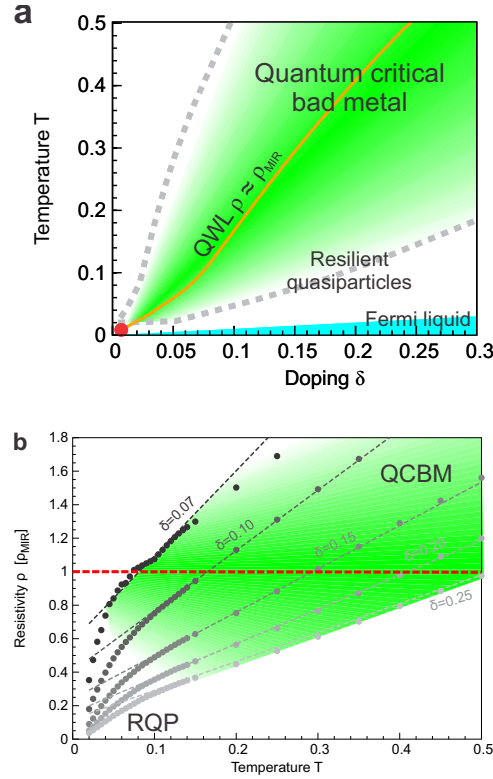
Figure 4.35: (a) DMFT phase diagram of the doped Mott insulator on a frustrated lattice. The bad metal (green) region matches perfectly the region of quantum critical scaling. (b) The bad metal regime features linear temperature dependence of resistivity with the slope roughly proportional to an inverse power law of doping which we find to be a consequence of underlying quantum criticality.

We find that the coefficient A has the numerical value $A \approx -0.74$. The functional form for $\rho(T)|_\delta$ close to the QWL is then directly determined by the behavior of the scaling parameter $x(T)|_\delta$

$$\rho(T)|_\delta \approx \rho^*(\delta)(1 + Ax(T)|_\delta) \tag{4.42}$$

On Fig. 4.38 we show the dependence $x(T - T^*(\delta))|_\delta$ for various dopings. When $10\% < \delta < 25\%$, $x(T)$ is found to be linear in a wide range of temperature around $T^*(\delta)$. Therefore,

$$\rho(T)|_\delta \approx \rho^*(\delta)\left(1 + A \left.\frac{\partial x}{\partial T}\right|_{\delta, T=T^*(\delta)} (T - T^*(\delta))\right). \tag{4.43}$$

The slope of $x(T)|_\delta$ at $T = T^*(\delta)$ can be estimated numerically, but in the following

127

we perform a semi-analytical derivation $\frac{\partial x}{\partial T}\big|_{\delta, T=T^*(\delta)}$, as it provides additional insight to the phenomenology of our model.

First we can rewrite $x(T)|_\delta$ as

$$x(T)|_\delta = c(\delta, T)(T - T^*(\delta))$$

so that the quantity $c(\delta, T)$ corresponds to the slope of $x(T)|_\delta$ precisely at the QWL, i.e.

$$c(\delta, T^*(\delta)) = \frac{\partial x}{\partial T}\bigg|_{\delta, T=T^*(\delta)}.$$

On the other hand we know

$$x = \frac{\delta\mu}{T^{1/z\nu}}$$

and we can use this to calculate $c(\delta, T)$. We have

$$c(\delta, T) = \frac{\mu(\delta, T) - \mu^*(T)}{(T - T^*(\delta))T^{1/z\nu}}$$

Setting here $T = T^*(\delta)$ immediately would yield a 0/0 expression on the right-hand side of the equation so we make one additional step. We first multiply the right-hand side of the equation by $\frac{\delta - \delta^*(T)}{\delta - \delta^*(T)}$ to obtain

$$c(\delta, T) = \frac{\mu(\delta, T) - \mu^*(T)}{\delta - \delta^*(T)} \frac{\delta - \delta^*(T)}{T - T^*(\delta)} T^{-1/z\nu}.$$

Now we are ready to take the limit $T \to T^*(\delta)$ of the two fractions that appear in this expression. Both numerator and denominator go to zero as T approaches $T^*(\delta)$, which is by definition the (partial) derivative of the quantity in the numerator with respect to the quantity in the denominator. For the second fraction we have

$$\lim_{T \to T^*(\delta)} \frac{\delta - \delta^*(T)}{T - T^*(\delta)} = -\left(\frac{dT^*}{d\delta}\right)^{-1} = -1/K(\delta) \tag{4.44}$$

where $K(\delta)$ is the slope of the QWL $T^*(\delta)$, at a given value of doping. The minus sign comes from the fact that when $T > T^*(\delta)$, $\delta < \delta^*(T)$ and vice versa. For the
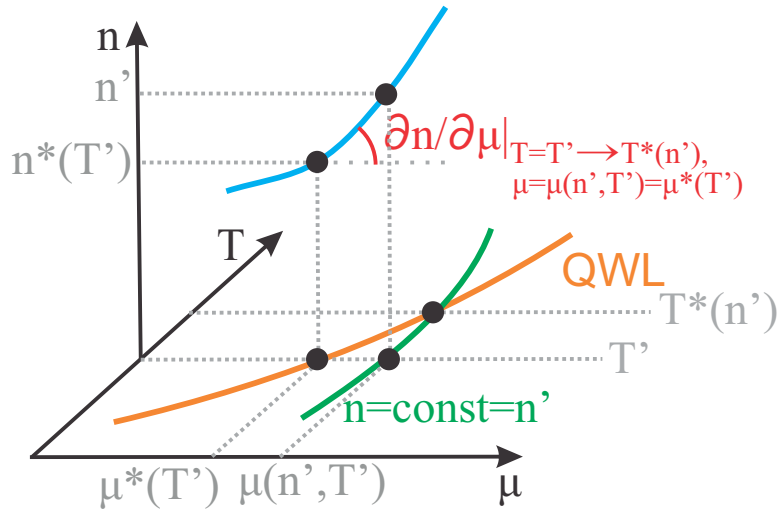
Figure 4.36: The information needed to switch between μ and δ dependence of quantities is contained in the charge compressibility.

first fraction we have

$$
\begin{aligned}
\lim_{T \to T^*(\delta)} \frac{\mu(\delta, T) - \mu^*(T)}{\delta - \delta^*(T)} &= \left.\left(\frac{\partial n}{\partial \mu}\right)^{-1}\right|_{\mu = \mu(\delta, T^*(\delta)), \, T = T^*(\delta)} \\
&= \frac{1}{\chi^*(\delta)}
\end{aligned}
\tag{4.45}
$$

which is the reciprocal value of charge compressibility precisely at the QWL, i.e. $\chi^*(\delta) = \chi(\delta, T^*(\delta))$. The above equation is illustrated in Fig. 4.36 Now we can
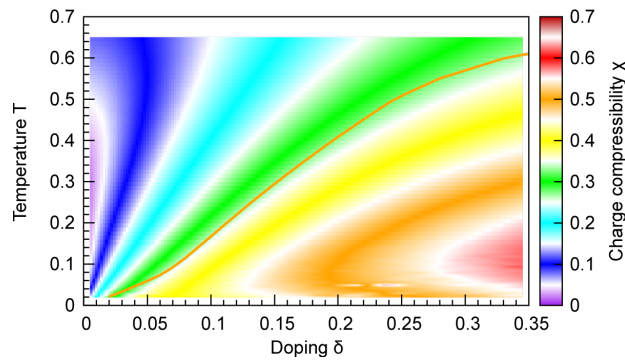
Figure 4.37: Color plot of the charge compressibility has the "fan-like" form, as generally expected for quantum criticality. The compressibility is approximately constant along the QWL.

estimate the limit of the entire expression for $c(\delta, T)$

$$c(\delta, T^*(\delta)) = -\frac{1}{\chi^*(\delta) \ K(\delta) \ T^*(\delta)^{\frac{1}{z\nu}}} \qquad (4.46)$$

Now we notice that in the doping range $10\% < \delta < 25\%$, $T^*(\delta)$ is basically linear, which means $K(\delta) \approx K$. Performing a linear fit to $T^*(\delta)$ we obtain $T^*(\delta) \approx K_0 + K\delta$, with $K \approx 2$ and K_0 small. Furthermore, we note that the charge compressibility is constant along the QWL, as shown in Fig. 4.37. This may be interpreted as another manifestation of the quantum critical behavior we identified. We have $\chi^*(\delta) \approx \chi^* = 0.33$. Finally we obtain

$$c(\delta, T^*(\delta)) \approx -\frac{1}{\chi^* \ K \ (K_0 + K\delta)^{\frac{1}{z\nu}}} \qquad (4.47)$$

Neglecting K_0 and noting that for $\delta > 5\%$, $\rho^*(\delta) = \rho_{\mathrm{MIR}}$, we have that in close vicinity of the QWL, resistivity is approximated by a linear function of the form

$$\rho_{\mathrm{QCBM}}(T)|_\delta \approx \rho_{\mathrm{MIR}} \left(1 + C \, \delta^{-1/z\nu}(T - K\delta)\right). \qquad (4.48)$$

which is the central result of this section.

In the quantum critical bad metal regime, the resistivity has a linear temperature dependence with the slope decreasing as a power $-1/z\nu$ of doping. This demonstrates a direct connection of the universal high temperature behavior in the Bad Metal regime with the (zero-temperature) quantum phase transition. The MIR limit of the resistivity is reached at temperature roughly proportional to the amount of doping, $T^*(\delta) \propto \delta$, since the doping level sets the main energy scale in the problem. The result of this simplified scaling formula is color-plotted in Fig. 4.40a (with $C = 0.69$, $K = 1.97$ and $z\nu = 1.35$) and shown to capture the features of the full DMFT solution at high temperatures.

On Fig. 4.38b we plot the relative error of this approximation $r(\delta, T) = |\rho_{\mathrm{DMFT}}(\delta, T) - \rho_{QCBM}(\delta, T)|/\rho_{\mathrm{DMFT}}(\delta, T)$. At low doping, the linear regime around $T^*(\delta)$ is short because here the linear approximation for $x(T)|_\delta$ is not justified in a wide range of temperature around the QWL. At dopings between 8 and 20%, $x(T)|_\delta$ is linear in a much wider range of temperature, producing a longer linear regime in $\rho(T)|_\delta$. At $\delta > 20\%$, the curvature of $x(T)|_\delta$ cancels the curvature of $\tilde{F}(x)$, and $\rho(T)|_\delta$ is found to be linear even at large x, where linear approximation of $\tilde{F}(x)$ is no longer

justified.
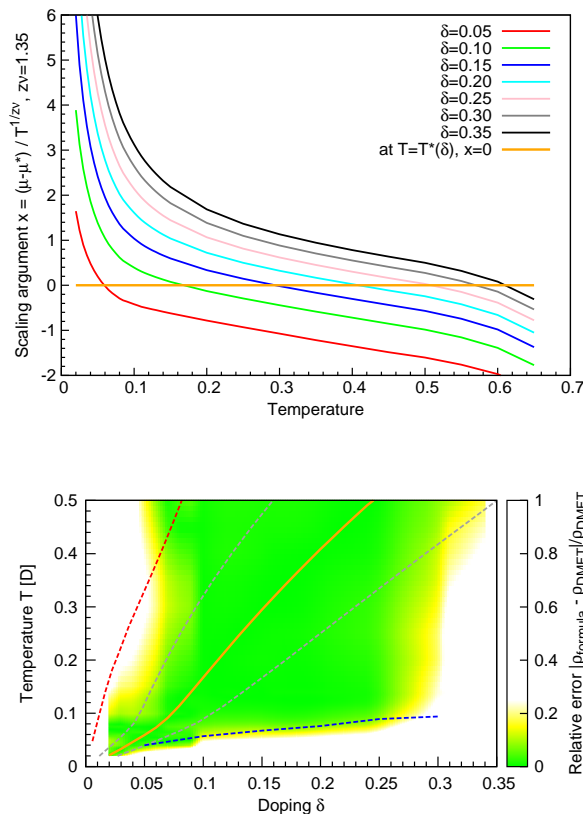
Figure 4.38: The linear approximation for $\rho(T)|_\delta$ works well in a large portion of the phase diagram. (a) The scaling argument temperature dependence $x(T)|_\delta$ can be approximated with a linear function in a wide range of temperature around the QWL $T^*(\delta)$, but only for mid-range dopings. (b) The linear approximation for $\rho(T)|_\delta$ works well even where $\tilde{F}(x)$ can no longer be approximated by a linear function (gray dashed lines denote $|x| = 0.5$). This is due to cancellation of the curvatures of $\tilde{F}(x)$ and $x(T)|_\delta$.

4.2.7 Comparison with experiments

Sufficiently systematic experimental studies of doped Mott insulators, covering an appreciable range of doping and temperature, remain relatively scarce. Still, approximately linear temperature dependence of the resistivity at high temperatures with the slope that decreases with doping has been observed, most notably in the seminal work of Takagi *et al.* [97] on $La_{2-x}Sr_xCuO_4$. To compare with our theory,
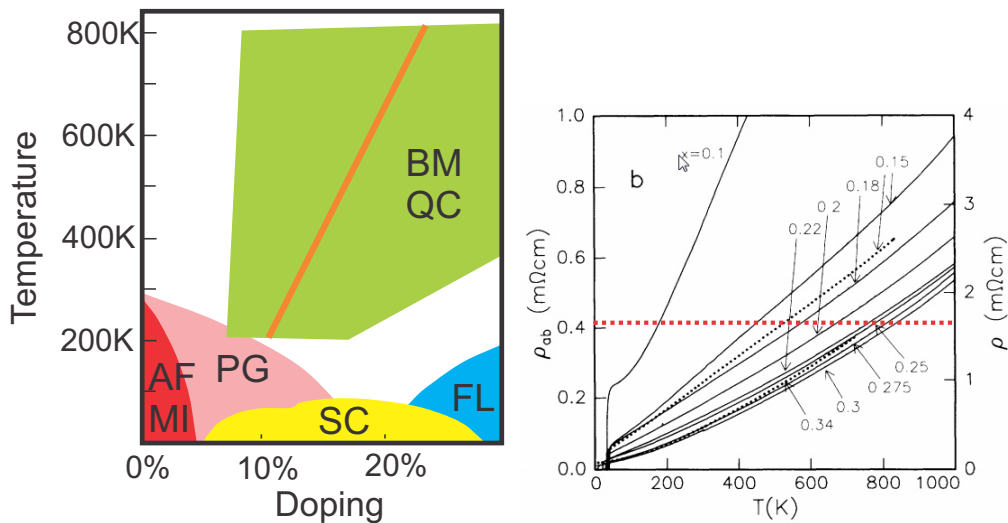
Figure 4.39: Left panel: The DMFT result resembles the high-temperature regime of the cuprates. The fully quantitative explanation of the low temperature part of the phase diagram is still elusive, but it is tempting to make three statements: 1) The Mott transition happens in stages - first stage is the sector selective transition between the full antiferromagnetic insulator and the pseudo-gap phase with Fermi pockets; the second stage reconstructs the Fermi surface completely leading to a doped Fermi liquid phase [96, 2, 26]; 2) In the vicinity of the second, PG-FL QCP, the quantum fluctuations boost the pairing mechanism producing the maximal T_c [1, 3]; 3) The hidden local Mott transition produces the QCBM regime observed at high temperatures, in the same way in single-site DMFT the QCP hidden by the first order transition produces the QC region at $T \gg T_c$. Right panel: linear resistivity regime in cuprates from Ref. [97]. The red line (added) is the estimate for the MIR limit in this material.

in Fig. 4.40 we color code the reported experimental data; here the temperature is shown in the units of T_{MIR} at 20% doping (note that the highest temperature shown in experiment is around only 0.1 of the estimated Fermi energy, while the estimated interaction strength is comparable to $U = 4$), and the resistivity is given in units of ρ_{MIR}, which in this material is estimated as 1.7 mΩcm. The experimental results presented in Fig. 4.40c cover the temperature range of $150 - 1000$ K at $5 - 30\%$ doping. Here one observes a striking similarity between DMFT theory and the experiment, as already noted in early studies [95, 94, 98]. We established this result by focusing on an exactly solvable model, where all ordering tendencies are suppressed, and single-site DMFT becomes exact. Real materials, of course, exist in finite (low) dimensions where systematic corrections to DMFT need to be included [99, 44, 78, 100]. In many cases [25, 101, 102], these nonlocal corrections prove
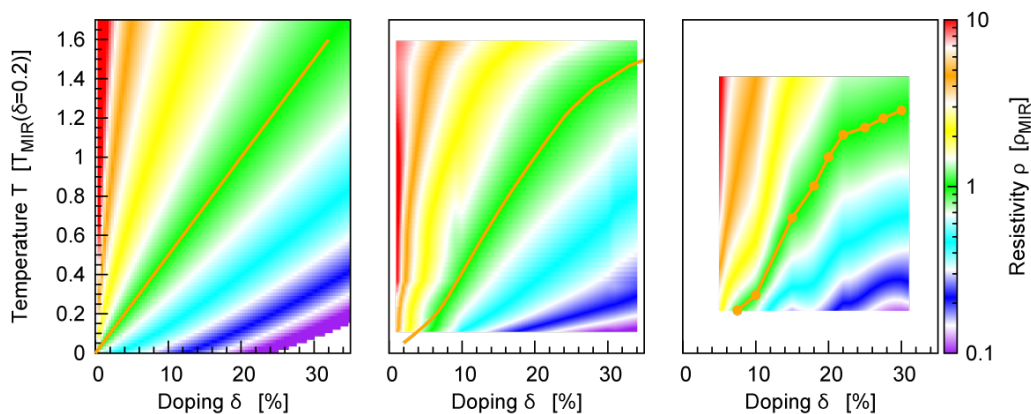
Figure 4.40: Resistivity given by (a) the semi-analytical formula obtained from the scaling hypothesis, (b) DMFT result, and (c) the experimental result on cuprate $La_{2-x}Sr_xCuO_4$ samples from Ref. [97].

significant only at sufficiently low temperatures. This indicates that our conclusion should remain valid and accurate in the high-temperature incoherent regime, establishing a conceptual link of the universal aspects of Bad Metal behavior and the quantum criticality associated with the Mott metal-insulator transition.

5.   Conclusions and prospects

We have successfully established, on theoretical and experimental grounds, that the high-temperature signatures of the Mott transition coincide with those of a quantum critical point, despite the presence of the finite temperature critical end-point and the associated coexistence region. In a large portion of the phase diagram, the DC resistivity has been found to follow a generalized quantum critical scaling law (generalized only in the sense that the role of the critical value of the control parameter is taken by a temperature-dependent quantity). Furthermore, we associated the linear resistivity around and beyond the Mott-Ioffe-Regel limit with the validity of this quantum critical (QC) scaling law, which provides new insight in the long standing problem of bad metal behavior.

To show the above we have performed large scale numerical computation, in excess of 500000 CPU hours, spanning 2 years in total. The bottleneck of the calculation was the solution of the impurity problem arising in single-site DMFT, and we used codes which are currently cutting edge in the field, both optimization-wise and method-wise [58]. We also developed a full implementation of the approximate, but far more efficient second order perturbative impurity solver (IPT) in both Matsubara and real frequency, and confirmed its applicability in the half-filled case by benchmarking it against the CTQMC result. Single-site DMFT was already known to qualitatively describe the phenomena associated with the Mott transition in many materials, but we were able to obtain the results with unprecedented level of detail, as necessary for the scaling analyses we subsequently performed.

Apart from the numerical simulation, we introduced, discussed and tested in practice the notion of the instability line, and connected it to the previously developed concept of the Widom lines. The use of a temperature dependent crossover line in the QC scaling formula is an original contribution to the sum of known QC phenomena and provides a novel approach to finite T_c first-order transitions in general. While previous efforts usually focused on the near vicinity of the finite temperature

critical-end point of the Mott transition, we showed that scaling behavior can be observed in a much bigger portion of the phase diagram, at $T > T_c$. The usefulness of our theory has been verified in an extensive experimental effort by Tetsuya et. al. [84] who documented the proposed universality in high-temperature behavior in 3 different organic materials. On the other hand, our theory of the origin of linear resistivity in the bad metal regime is far from being the only one ([14, 13]), and there are even other scaling scenarios proposed as the description of this regime [103]. However, our theory of quantum critical scaling brings further evidence to the intuition that the strange properties of the normal state in cuprates have much to do with the vicinity of a quantum critical point. Moreover, our approach, unlike any other, provides a unified framework for dealing with the two largest classes of unconventional superconductors (κ-organics and cuprates) in a similar way a recent study connected the phase diagram of pnictide superconductors with that of the cuprates [104].

There are however a number of standing issues with our theory and several immediate generalizations which should be tested in future work. Firstly, we have observed that the critical exponents depend on the method used (IPT vs. CTQMC), and also on the parameter used in the scaling formula (U vs. μ). The open question now is to what extent is the critical exponent universal, and whether one can truly observe different universality classes of Mott insulators, in experiment. Also in theory, one needs to address various models and investigate the dependence of critical exponents on the choice of scaling parameter and specifics of the model in more detail.

One model of particular interest is the Anderson lattice model which features two Mott transitions - between the integer filled Mott insulator and the hole-doped or electron-doped metal [38]. The hole-doped transition does not seem to feature a coexistence region and here $T_c = 0$. Testing the scaling hypothesis in this case and comparing the extent of the scaling region between the zero T_c and finite T_c cases should be an important line of future work.

Another important model that should be revisited in the view of our results is the double-Bethe lattice in which the T_c has been shown to go to exactly zero by tuning the inter-lattice hopping amplitude [37]. This provides an excellent opportunity to track the evolution of the QC phenomena as the first-order transition continuously transforms into a pure QCP. Furthermore, in the intermediate regime when both the inter-lattice hopping and T_c are different from zero, the transition remains of

the first order even at $T = 0$, unlike what is the case in single-site DMFT. It would be important to see whether the presence of the actual second order critical point at $T = 0$ in our model has any importance for the observed high-temperature behavior.

Also, an important question is whether our conclusions are restricted to models with only the local correlations. Especially concerning the cuprates which are low-dimensional and at low temperature exhibit a phenomenology drastically different from what is seen in single-site DMFT - one should test whether our results hold in the presence of non-local correlations. These become essential at low temperature, but may have non-trivial effects even in the bad metal regime. The effect of non-locality can be systematically included in DMFT by considering a site cluster instead of a single-site impurity, and such calculation should provide an important test of our approach. Furthermore, the effects of particle-hole asymmetry can also be tested, although the comparison with κ-organic systems which are triangular lattices is already very favorable.

Most importantly, given the excellent agreement of DMFT with the κ-organic materials, one should be able to predict their pressure-temperature phase diagram even away from half-filling. In a recent measurement on doped κ-organics, linear resistivity was reported, in agreement with our theory [105]. Furthermore, the Mott insulating state is not present in the doped systems (in agreement with DMFT), but only a crossover between the weakly and strongly-correlated metallic states is observed as pressure is varied. An important aspect for the characterization of these regimes is the average double occupancy, which can be calculated in DMFT with high accuracy. A study of double occupancy and dynamic (local) two particle-correlations, at a fixed level of doping and varied on-site interaction energy U, could be of high importance in the view of future experiments.

Having this in mind, we believe the results presented in this thesis put the fundamentally important phenomenon of the Mott transition in a wider perspective, and open a clear direction for future studies possibly leading to a deeper understanding of the many-body correlation in condensed matter systems.

Bibliography

[1] J.-H. She and J. Zaanen, BCS superconductivity in quantum critical metals, *Phys. Rev. B* **80**, 184518 (2009). 2, 132

[2] B. Keimer, S. A. Kivelson, M. R. Norman, S. Uchida, and J. Zaanen, From quantum matter to high-temperature superconductivity in copper oxides, *Nature* **518**, 179 (2015). 2, 3, 132

[3] S.-X. Yang, H. Fotso, S.-Q. Su, D. Galanakis, E. Khatami, J.-H. She, J. Moreno, J. Zaanen, and M. Jarrell, Proximity of the superconducting dome and the quantum critical point in the two-dimensional Hubbard model, *Phys. Rev. Lett.* **106**, 047004 (2011). 2, 132

[4] S. Sachdev, *Quantum Phase Transitions*, Cambridge University Press (1999). 2, 5, 8, 82, 87, 88

[5] H. v. Löhneysen, A. Rosch, M. Vojta, and P. Wölfle, Fermi-liquid instabilities at magnetic quantum phase transitions, *Rev. Mod. Phys.* **79**, 1015 (2007). 2, 5, 8

[6] D. E. Sheehy and Jörg Schmalian, Quantum critical scaling in graphene, *Phys. Rev. Lett.* **99**, 226803 (2007). 2, 11

[7] R. Yu, C. F. Miclea, F. Weickert, R. Movshovich, A. Paduan-Filho, V. S. Zapf, and T. Roscilde, Quantum critical scaling at a bose-glass/superfluid transition: Theory and experiment for a model quantum magnet, *Phys. Rev. B* **86**, 134421 (2012). 2, 11

[8] D. Shahar, D. C. Tsui, M. Shayegan, R. N. Bhatt, and J. E. Cunningham, Universal conductivity at the quantum Hall liquid to insulator transition, *Phys. Rev. Lett.* **74**, 4511 (1995). 2, 11

[9] A. Yazdani and A. Kapitulnik, Superconducting-insulating transition in two-dimensional α-MoGe thin films, *Phys. Rev. Lett.* **74**, 3037 (1995). 2, 11, 13, 14

[10] H. P. Wei, D. C. Tsui, M. A. Paalanen, and A. M. M. Pruisken, Experiments on delocalization and university in the integral quantum Hall effect, *Phys. Rev. Lett.* **61**, 1294 (1988). 2, 11, 12

[11] S. V. Kravchenko, W. E. Mason, G. E. Bowker, J. E. Furneaux, V. M. Pudalov, and M. D'Iorio, Scaling of an anomalous metal-insulator transition in a two-dimensional system in silicon at $B = 0$, *Phys. Rev. B* **51**, 7038 (1995). 2, 14, 15, 16, 17

[12] M. Čubrović, J. Zaanen, and K. Schalm, String theory, quantum phase transitions, and the emergent Fermi liquid, *Science* **325**, 439 (2009). 2

[13] A. Donos and S. A. Hartnoll, Interaction-driven localization in holography, *Nat. Phys.* **9**, 649 (2013). 2, 135

[14] R. A. Davison, K. Schalm, and J. Zaanen, Holographic duality and the resistivity of strange metals, *Phys. Rev. B* **89**, 245116 (2014). 2, 135

[15] S. Sachdev, Holographic metals and the fractionalized Fermi liquid, *Phys. Rev. Lett.* **105**, 151602 (2010). 2

[16] S. Sondhi, S. Girvin, J. Carini, and D. Shahar, Continuous quantum phase transitions, *Rev. Mod. Phys.* **69**, 315 (1997). 5, 8, 9, 12

[17] Mats Wallin, E. S. Sørensen, S. M. Girvin, and A. P. Young, Superconductor-insulator transition in two-dimensional dirty boson systems, *Phys. Rev. B* **49**, 12115 (1994). 6

[18] N. Goldenfeld, *Lectures on Phase Transitions and the Renormalization Group*, Addison-Wesley, Reading, MA (1992). 6

[19] P.M. Chaikin and T.C. Lubensky, *Principles of Condensed Matter Physics*, Cambridge University, New York (1995). 6

[20] M. P. A. Fisher, Quantum phase transitions in disordered two-dimensional superconductors, *Phys. Rev. Lett.* **65**, 923 (1990). 13

[21] S. V. Kravchenko, D. Simonian, M. P. Sarachik, W. Mason, and J. E. Furneaux, Electric field scaling at a $B = 0$ metal-insulator transition in two dimensions, *Phys. Rev. Lett.* **77**, 4938 (1996). 17

[22] V. Dobrosavljević, E. Abrahams, E. Miranda, and S. Chakravarty, Scaling theory of two-dimensional metal-insulator transitions, *Phys. Rev. Lett.* **79**, 455 (1997). 18, 101, 102, 103, 123

[23] D. Simonian, S. V. Kravchenko, and M. P. Sarachik, Reflection symmetry at a $B = 0$ metal-insulator transition in two dimensions, *Phys. Rev. B* **55**, 13421 (1997). 18, 103

[24] A. Georges, G. Kotliar, W. Krauth, and M. J. Rozenberg, Dynamical mean-field theory of strongly correlated fermion systems and the limit of infinite dimensions, *Rev. Mod. Phys.* **68**, 13 (1996). 18, 28, 37, 81, 92, 112, 114, 144

[25] A. Georges, Thinking locally: reflections on dynamical mean-field theory from a high-temperature/high energy perspective, *Annalen der Physik* **523**, 672 (2011). 18, 132

[26] A. Georges, Strongly correlated electron materials: Dynamical mean-field theory and electronic structure, *arXiv:cond-mat/0403123* (2004). 18, 26, 27, 28, 132

[27] N. F. Mott, The basis of the electron theory of metals, with special reference to the transition metals, *Proceedings of the Physical Society. Section A* **62**, 416 (1949). 19

[28] C. Castellani, C. D. Castro, D. Feinberg, and J. Ranninger, New model Hamiltonian for the metal-insulator transition, *Phys. Rev. Lett.* **43**, 1957 (1979). 20

[29] D. B. McWhan, A. Menth, J. P. Remeika, W. F. Brinkman, and T. M. Rice, Metal-insulator transitions in pure and doped V_2O_3, *Phys. Rev. B* **7**, 1920 (1973). 20, 21

[30] P. Limelette, A. Georges, D. Jérome, P. Wzietek, P. Metcalf, and J. M. Honig, Universality and critical behavior at the Mott transition, *Science* **302**, 89 (2003). 20, 22, 23

[31] F. Kagawa, K. Miyagawa, and K. Kanoda, Unconventional critical behaviour in a quasi-two-dimensional organic conductor, *Nature* **436**, 534 (2005). 20, 24

[32] S. Lefebvre, P. Wzietek, S. Brown, C. Bourbonnais, D. Jérome, C. Mézière, M. Fourmigué, and P. Batail, Mott transition, antiferromagnetism, and unconventional superconductivity in layered organic superconductors, *Phys. Rev. Lett.* **85**, 5420 (2000). 20

[33] F. Kagawa, T. Itou, K. Miyagawa, and K. Kanoda, Transport criticality of the first-order Mott transition in the quasi-two-dimensional organic conductor κ-(BEDT-TTF)$_2$Cu[N(CN)$_2$]Cl, *Phys. Rev. B* **69**, 064511 (2004). 20

[34] M. J. Rozenberg, G. Kotliar, and X. Y. Zhang, Mott-Hubbard transition in infinite dimensions. II, *Phys. Rev. B* **49**, 10181 (1994). 21, 22

[35] B. J. Powell and R. H. McKenzie, Quantum frustration in organic Mott insulators: from spin liquids to unconventional superconductors, *Reports on Progress in Physics* **74**, 056501 (2011). 23

[36] G. Kotliar, E. Lange, and M. J. Rozenberg, Landau theory of the finite temperature Mott transition, *Phys. Rev. Lett.* **48**, 5180 (2000). 24, 89, 92

[37] G. Moeller, V. Dobrosavljević, and A. E. Ruckenstein, RKKY interactions and the Mott transition, *Phys. Rev. B* **59**, 6846 (1999). 24, 25, 98, 135

[38] G. Sordi, A. Amaricci, and M. J. Rozenberg, Asymmetry between the electron- and hole-doped Mott transition in the periodic Anderson model, *Phys. Rev. B* **80**, 035129 (2009). 24, 25, 135

[39] R. Jordens, N. Strohmaier, K. Gunter, H. Moritz, and T. Esslinger, A Mott insulator of fermionic atoms in an optical lattice, *Nature* **455**, 204 (2008). 28

[40] M. Greiner, O. Mandel, T. Esslinger, T. W. Hansch, and I. Bloch, Quantum phase transition from a superfluid to a Mott insulator in a gas of ultracold atoms, *Nature* **415**, 39 (2002). 28

[41] D. Jaksch, C. Bruder, J. I. Cirac, C. W. Gardiner, and P. Zoller, Cold bosonic atoms in optical lattices, *Phys. Rev. Lett.* **81**, 3108 (1998). 28

[42] E. Kozik, K. v. Houcke, E. Gull, L. Pollet, N. Prokof'ev, B. Svistunov, and M. Troyer, Diagrammatic Monte Carlo for correlated fermions, *Europhys. Lett.* **90**, 10004 (2010). 28

[43] J. Merino, M. Dumm, N. Drichko, M. Dressel, and R. H. McKenzie, Quasi-particles at the verge of localization near the Mott metal-insulator transition in a two-dimensional material, *Phys. Rev. Lett.* **100**, 086404 (2008). 28

[44] G. Kotliar, S. Y. Savrasov, K. Haule, V. S. Oudovenko, O. Parcollet, and C. A. Marianetti, Electronic structure calculations with dynamical mean-field theory, *Rev. Mod. Phys.* **78**, 865 (2006). 28, 29, 132

[45] X. Deng, J. Mravlje, R. Žitko, M. Ferrero, G. Kotliar, and A. Georges, How bad metals turn good: Spectroscopic signatures of resilient quasiparticles, *Phys. Rev. Lett.* **110**, 086401 (2013). 28, 86, 113, 122, 125, 126, 146

[46] W. Metzner and D. Vollhardt, Correlated lattice fermions in $d = \infty$ dimensions, *Phys. Rev. Lett.* **62**, 324 (1989). 37

[47] A. Khurana, Electrical conductivity in the infinite-dimensional Hubbard model, *Phys. Rev. Lett.* **64**, 1990 (1990). 39

[48] L.-F. Arsenault and A.-M. S. Tremblay, Transport functions for hypercubic and Bethe lattices, *Phys. Rev. B* **88**, 205109 (2013). 39

[49] E. Gull, A. J. Millis, A. I. Lichtenstein, A. N. Rubtsov, M. Troyer, and P. Werner, Continuous-time Monte Carlo methods for quantum impurity models, *Rev. Mod. Phys.* **83**, 349 (2011). 43, 63, 112

[50] H. Kajueter and G. Kotliar, New iterative perturbation scheme for lattice models with arbitrary filling, *Phys. Rev. Lett.* **77**, 131 (1996). 62, 74

[51] X. Y. Zhang, M. J. Rozenberg, and G. Kotliar, Mott transition in the $d = \infty$ Hubbard model at zero temperature, *Phys. Rev. Lett.* **70**, 1666 (1993). 62, 74

[52] K. Haule, S. Kirchner, J. Kroha, and P. Wölfle, Anderson impurity model at finite Coulomb interaction U : Generalized noncrossing approximation, *Phys. Rev. B* **64**, 155111 (2001). 62

[53] M. Capone, L. de' Medici, and A. Georges, Solving the dynamical mean-field theory at very low temperatures using the Lanczos exact diagonalization, *Phys. Rev. B* **76**, 245116 (2007). 62

[54] R. Bulla, T. A. Costi, and T. Pruschke, Numerical renormalization group method for quantum impurity systems, *Rev. Mod. Phys.* **80**, 395 (2008). 62

[55] D. J. Garcia, K. Hallberg, and M. J. Rozenberg, Dynamical mean field theory with the density matrix renormalization group, *Phys. Rev. Lett.* **93**, 246403 (2004). 62

[56] J. E. Hirsch and R. M. Fye, Monte Carlo method for magnetic impurities in metals, *Phys. Rev. Lett.* **56**, 2521 (1986). 62

[57] P. Werner, A. Comanac, L. de Medici, M. Troyer, and A. J. Millis, Continuous-time solver for quantum impurity models, *Phys. Rev. Lett.* **97**, 076405 (2006). 63, 112

[58] K. Haule, Quantum Monte Carlo impurity solver for cluster dynamical mean-field theory and electronic structure calculations with adjustable cluster base, *Phys. Rev. B* **75**, 155113 (2007). 63, 112, 134

[59] M. Jarrell and J. E. Gubernatis, Bayesian inference and the analytic continuation of imaginary-time quantum Monte Carlo data, *Physics Reports* **269**, 133 (1996). 78, 119

[60] H. Terletska, J. Vučičević, D. Tanasković, and V. Dobrosavljević, Quantum critical transport near the Mott transition, *Phys. Rev. Lett.* **107**, 026401 (2011). 80

[61] J. Vučičević, H. Terletska, D. Tanasković, and V. Dobrosavljević, Finite-temperature crossover and the quantum Widom line near the Mott transition, *Phys. Rev. B* **88**, 075143 (2013). 80

[62] J. Vučičević, D. Tanasković, M. J. Rozenberg, and V. Dobrosavljević, Bad-metal behavior reveals Mott quantum criticality in doped Hubbard models, *Phys. Rev. Lett.* **114**, 246402 (2015). 80

[63] N. E. Hussey, K. Takenaka, and H. Takagi, Universality of the Mott-Ioffe-Regel limit in metals, *Philos. Mag.* **84**, 2847 (2004). 82, 100, 101

[64] J. Merino and R. H. McKenzie, Transport properties of strongly correlated metals: A dynamical mean-field approach, *Phys. Rev. B* **61**, 7996 (2000). 82, 86

[65] K. Haule and G. Kotliar, Avoided criticality in near-optimally doped high-temperature superconductors, *Phys. Rev. B* **76**, 092503 (2007). 83

[66] R. A. Cooper, Y. Wang, B. Vignolle, O. J. Lipscombe, S. M. Hayden, Y. Tanabe, T. Adachi, Y. Koike, M. Nohara, H. Takagi, Cyril Proust, and N. E. Hussey, Anomalous criticality in the electrical resistivity of $La_{2-x}Sr_xCuO_4$, *Science* **323**, 603 (2009). 83

[67] P. Gegenwart, Q. Si, and F. Steglich, Quantum criticality in heavy-fermion metals, *Nature Physics* **4**, 186 (2008). 83

[68] W. Xu, K. Haule, and G. Kotliar, Hidden Fermi liquid, scattering rate saturation and Nernst effect: a DMFT perspective, *arXiv: 1304.7486* (2013). 86

[69] P. Limelette, P. Wzietek, S. Florens, A. Georges, T. A. Costi, C. Pasquier, D. Jérome, C. Mézière, and P. Batail, Mott transition and transport crossovers in the organic compound κ-(BEDT-TTF)$_2$Cu[N(CN)$_2$]Cl, *Phys. Rev. Lett.* **91**, 016401 (2003). 86

[70] J. Merino, M. Dumm, N. Drichko, M. Dressel, and R. H. McKenzie, Quasiparticles at the verge of localization near the Mott metal-insulator transition in a two-dimensional material, *Phys. Rev. Lett.* **100**, 086404 (2008). 86

[71] M. M. Radonjić, D. Tanasković, V. Dobrosavljević, and K. Haule, Influence of disorder on incoherent transport near the Mott transition, *Phys. Rev. B* **81**, 075118 (2010). 86

[72] V. Dobrosavljević, N. Trivedi, and J. M. Valles, Jr., *Conductor-Insulator Quantum Phase Transitions*, Oxford University Press (2012). 87

[73] P. Nozières, Some comments on Kondo lattices and the Mott transition, *Eur. Phys. J. B* **6**, 447 (1998). 88

[74] B. Widom, *On Phase Transitions and Critical Phenomena, Vol2 (eds C. Domb, and M. S. Green)*, Academic (1972). 89

[75] L. Xu, P. Kumar, S. V. Buldyrev, S.-H. Chen, P. H. Poole, F. Sciortino, and H. E. Stanley, Relation between the Widom line and the dynamic crossover in systems with a liquid–liquid phase transition, *Proc. Nat. Acad. Sci.* **102**, 16558 (2005). 89

[76] G. G. Simeoni, T. Bryk, F. A. Gorelli, M. Krisch, G. Ruocco, M. Santoro, and T. Scopigno, The Widom line as the crossover between liquid-like and gas-like behaviour in supercritical fluids, *Nature Physics* **6**, 503 (2010). 90, 117

[77] G. Sordi, P. Sémon, and A.-M.S. Tremblay, Pseudogap temperature as a Widom line in doped Mott insulators, *Scientific Reports* **2**, 547 (2012). 90

[78] G. Sordi, P. Sémon, K. Haule, and A.-M. S. Tremblay, c-axis resistivity, pseudogap, superconductivity, and Widom line in doped Mott insulators, *Phys. Rev. B* **87**, 041101 (2013). 90, 132

[79] G. Moeller, V. Dobrosavljević, and A. E. Ruckenstein, RKKY interactions and the Mott transition, *Phys. Rev. B* **59**, 6846 (1999). 92

[80] We note that other criteria have also been emplyed to identify a MIT crossover line. [106] used the flatness of the lowest Matsubara points of the self-energy, [24, 107] used the inflection point of the resistivity curves. We have not revealed any apparent scaling behavior following these trajectories. 100

[81] B. J. Powell and R. H. McKenzie, Strong electronic correlations in superconducting organic charge transfer salts, *J. Phys.: Condens. Matter* **18**, 827 (2006). 101

[82] E. Abrahams, S. V. Kravchenko, and M. P. Sarachik, Metallic behavior and related phenomena in two dimensions, *Rev. Mod. Phys.* **73**, 251 (2001). 103

[83] E. Abrahams, P. W. Anderson, D. C. Licciardello, and T. V. Ramakrishnan, Scaling theory of localization: Absence of quantum diffusion in two dimensions, *Phys. Rev. Lett.* **42**, 673 (1979). 103

[84] T. Furukawa, K. Miyagawa, H. Taniguchi, R. Kato, and K. Kanoda, Quantum criticality of Mott transition in organic materials, *Nat. Phys.* **11**, 221 (2015). 108, 109, 110, 111, 135

[85] K. Kanoda, Private communication. 109

[86] A. Camjayi, R. Chitra, and M. J. Rozenberg, Electronic state of a doped Mott-Hubbard insulator at finite temperatures studied using the dynamical mean-field theory, *Phys. Rev. B* **73**, 041103 (2006). 112, 126

[87] G. Kotliar, S. Murthy, and M. J. Rozenberg, Compressibility divergence and the finite temperature Mott transition, *Phys. Rev. Lett.* **89**, 046401 (2002). 112, 114

[88] R. Žitko, D. Hansen, E. Perepelitsky, J. Mravlje, A. Georges, and B. S. Shastry, Extremely correlated Fermi liquid theory meets dynamical mean-field theory: Analytical insights into the doping-driven Mott transition, *Phys. Rev. B* **88**, 235132 (2013). 114

[89] D. S. Fisher, G. Kotliar, and G. Moeller, Midgap states in doped Mott insulators in infinite dimensions, *Phys. Rev. B* **52**, 17112 (1995). 114, 116

[90] P. Werner and A. J. Millis, Doping-driven Mott transition in the one-band Hubbard model, *Phys. Rev. B* **75**, 085108 (2007). 114

[91] M. J. Rozenberg, R. Chitra, and Gabriel Kotliar, Finite temperature Mott transition in the Hubbard model in infinite dimensions, *Phys. Rev. Lett.* **83**, 3498 (1999). 116

[92] M. J. Case and V. Dobrosavljević, Quantum critical behavior of the cluster glass phase, *Phys. Rev. Lett.* **99**, 147204 (2007). 118

[93] A. W. Sandvik, Stochastic method for analytic continuation of quantum Monte Carlo data, *Phys. Rev. B* **57**, 10287 (1998). 119

[94] Th. Pruschke, D.L. Cox, and M. Jarrell, Hubbard model at infinite dimensions: Thermodynamic and transport properties, *Phys. Rev. B* **47**, 3553 (1993). 125, 132

[95] M. Jarrell and Th. Pruschke, Anomalous properties of the Hubbard model in infinite dimensions, *Phys. Rev. B* **49**, 1458 (1994). 126, 132, 146

[96] J. Zaanen and B. J. Overbosch, Mottness collapse and statistical quantum criticality, *Philosophical Transactions of the Royal Society of London A: Mathematical, Physical and Engineering Sciences* **369**, 1599 (2011). 132

[97] H. Takagi, B. Batlogg, H. L. Kao, J. Kwo, R. J. Cava, J. J. Krajewski, and W. F. Peck, Systematic evolution of temperature-dependent resistivity in $La_{2-x}Sr_xCuO_4$, *Phys. Rev. Lett.* **69**, 2975 (1992). 131, 132, 133

[98] The high-temperature slope of the resistivity curves is estimated to be proportional to δ^{-1} in Ref. [95]. However, only four doping levels were considered and having in mind the uncertainty of the analytical continuation, it is difficult to distinguish this value from our slope $\delta^{-1/z\nu} = \delta^{-1/1.35}$. Our numerical data are in agreement with high precision CTQMC data from Ref. [45]. 132

[99] T. Maier, M. Jarrell, T. Pruschke, and M. H. Hettler, Quantum cluster theories, *Rev. Mod. Phys.* **77**, 1027 (2005). 132

[100] E. Gull, O. Parcollet, and A. J. Millis, Superconductivity and the pseudogap in the two-dimensional Hubbard model, *Phys. Rev. Lett.* **110**, 216405 (2013). 132

[101] D. Tanasković, K. Haule, G. Kotliar, and V. Dobrosavljević, Phase diagram, energy scales, and nonlocal correlations in the Anderson lattice model, *Phys. Rev. B* **84**, 115105 (2011). 132

[102] J. Kokalj and R. H. McKenzie, Thermodynamics of a bad metal-Mott insulator transition in the presence of frustration, *Phys. Rev. Lett.* **110**, 206402 (2013). 132

[103] A. Karch S. A. Hartnoll, Scaling theory of the cuprate strange metals, *arXiv:1501.03165.* 135

[104] L. de' Medici, G. Giovannetti, and M. Capone, Selective Mott physics as a key to iron superconductors, *Phys. Rev. Lett.* **112**, 177001 (2014). 135

[105] H. Oike, K. Miyagawa, H. Taniguchi, and K. Kanoda, Mottness in a doped organic superconductor, *arXiv:1409.4965.* 136

[106] H. Park, K. Haule, and G. Kotliar, Cluster dynamical mean field theory of the Mott transition, *Phys. Rev. Lett.* **101**, 186403 (2008). 144

[107] M. J. Rozenberg, G. Kotliar, H. Kajueter, G. A. Thomas, D. H. Rapkine, J. M. Honig, and P. Metcalf, Optical conductivity in Mott-Hubbard systems, *Phys. Rev. Lett.* **75**, 105 (1995). 144

CURRICULUM VITAE

Jaksa Vučičević

Scientific Computing Laboratory,
Institute of Physics Belgrade,
Pregrevica 118, 11080 Belgrade, Serbia

phone: +381 11 3713 152
mobile: +381 65 4462 562

email: jaksa@scl.rs

Born

May 30, 1984 in Belgrade, Serbia

Education

2009 - Diploma in Physics, Faculty of Physics, University of Belgrade.
2015 (expected) - Ph.D., Faculty of Physics, University of Belgrade.

Research experience

2009-*present* - Research Assistant at the Scientific Computing Laboratory, Institute of Physics Belgrade
2014 - three weeks visitor program at the Institute of Physics, Chinese Academy of Sciences, Beijing

Research interests

Quantum critical phenomena associated with the Mott metal-insulator transition

The Mott transition as observed in the dynamical mean field theory (DMFT) solution of the Hubbard model in infinite dimensions is of the first order up to some critical temperature, and features a coexistence region where both metallic and insulating states are locally stable. However, at sufficiently high temperature, a typical quantum critical behavior is recovered. All the linear response DC resistivity data can be collapsed onto two distinct branches when plotted against an argument of the form indicative of quantum critical scaling. The results obtained at half filling show excellent agreement with experiments on various Kappa organic materials.

In the case of doping-driven Mott transition at a fixed (large) value of on-site interaction, the critical temperature for the first order transition is found to be much lower than at half-filling. The quantum critical region here extends to lower temperatures and at high temperature covers most of the phase diagram. Furthermore, it matches the region of bad metal behavior, where resistivity is linear in temperature and of the order of Mott-Ioffe-Regel (MIR) limit and higher. This behavior can be explained in terms of quantum critical behavior - both the linearity and slope of resistivity around the MIR limit are consistent with the validity of a scaling function of a single argument. It turns out that the bad metal regime holds information about the hidden zero temperature Mott transition, and that critical exponents

can be extracted from the doping dependence of the slope of resistivity around MIR limit. A physical picture qualitatively similar to the DMFT result is found in cuprate films in the temperature range 200-1000 K, between 10 and 30% hole doping.

Cluster DMFT on a triangular lattice (work in progress)

Whether the QC phenomena observed in single-site DMFT are specific to the local approximation is an open question. The Mott transition and the crossover region are systematically examined as non-local correlations are introduced by considering 3,4 and 6-site clusters in DMFT.

Hybridization expansion CTQMC (work in progress)

The main limitation of the hybridization expansion continuous-time quantum Monte Carlo impurity solver is the cluster size. As compared to the interaction-expansion algorithm which allows for treatment of as many as 16 lattice sites in the impurity problem, hybridization expansion relies on exact calculation of the trace over impurity degrees of freedom which is practical only when cluster size is less than or equal 5. Already for 7 orbital clusters, a truncation of the basis set is required for the calculation to become feasible, but this is an uncontrolled approximation and should be avoided. A systematic solution to this problem is proposed by means of supplementing the hybridization expansion (HE) algorithm with a world line Monte Carlo. In each MC step of the HE-CTQMC, the impurity trace can be calculated by a world line algorithm, but even better performance is expected if both MC procedures are performed in a single, joint Markov chain. The severity of the sign problem is expected to be the same as in the original algorithm.

Competition between Anderson and Mott localization (work in progress)

Disorder in the Hubbard model can be modeled by considering an ensemble of impurities with various orbital energies, and closing the DMFT loop by the averaged result of impurity problems - when the geometrical average of the densities of states is used, the DMFT procedure is called the typical medium theory. Using this approach, one can analyze the interplay of disorder and interaction. It turns out that disorder protects the system from Mott localization, and vice versa - the system is found to be most metallic when the amount of disorder (width of the orbital energy distribution) is comparable to the strength of the interaction. With increasing disorder, the critical temperature for the first order Mott transition drops quickly, and the coexistence region transforms into two quantum critical lines, separating three distinct phases - the pure Mott insulator, the mixed Anderson-Mott insulator, and the Fermi liquid.

Unstable fixed point of DMFT (work in progress)

Close to the critical point of the first-order Mott transition, the correlation length diverges, and thus the domain walls separating the Fermi liquid and the Mott insulator become very thick. This can be explicitly shown by performing the inhomogeneous (real space) DMFT. The intermediate phase appearing at the middle of the domain wall is neither the Fermi liquid, nor the Mott insulator, and is expected to dominate the overall behavior of the system. It is found that this state corresponds to the unstable fixed point of the DMFT, which can be converged in the coexistence region by means of a root-finding-algorithm assisted DMFT loop, or using the phase-space extension technique. The properties of this unstable solution are analyzed and it is found that it is fairly metallic, with resistivity increasing linearly with temperature (when calculated along the trajectory of the first order transition where metallic and insulating solution are of the same energy).

d-wave superconductivity in honeycomb bilayer

The low-energy properties of a pair of Bernal stacked honeycomb lattices can be described by an effective single layer honeycomb lattice with additional third neighbor hopping amplitude. The interaction effects are expected to play a role in these systems and are modeled in a tJ-like manner, and solved by means of meanfield theory. A 5 parameter minimization of free energy reveals an instability towards superconducting order of various symmetries. The superconductivity is particularly favored when the Fermi level is around the vanHove singularity in the non-interacting density of states. At the van-Hove singularity and closer to halffilling, at low values of attractive interaction, a $d+id$ time-reversal symmetry breaking superconductivity is found.

Burkov-Macdonald model of QHE bilayer (work in progress)

Quantum Hall bilayer at filling factor one can be described by an effective Heisenberg model with anisotropic couplings. The long range Coulomb interaction of the original (continuous space) model enters the Heisenberg model also through next nearest neighbor couplings. Using the Schwinger boson representation of the Hesienberg model, a mean field theory can be formulated in terms of (anti)ferromagnetic bond operators. The solutions found feature lowest lying excitations at some finite momentum, in agreement with exact diagonalization of the QHE bilayer in torus geometry. A possible interpretation of the ground state as a Z2 pseudospin liquid is pursued.

Programming skills

C/C++, Fortran, Python, Java, Mathematica, parallel programming OpenMP/MPI/hybrid.

Data visualization in gnuplot, CorelDRAW, 3dsMAX/maxscript.

Interactive visuelization/GUI - Processing 2.0, Delphi, C#

Publications

2014 - J. Vučičević, D. Tanasković, M. Rozenberg, V. Dobrosavljević: "Bad-metal behavior reveals Mott quantum criticality in doped Hubbard models", Phys. Rev. Lett. 114, 246402 (2015)

2013 - J. Vučičević, H. Terletska, D. Tanasković, V. Dobrosavljević: "Finite temperature crossovers and the quantum Widom line near the Mott transition", Phys. Rev. B 88, 075143

2012 - J. Vučičević, M. O. Goerbig, M. V. Milovanović: "d-wave superconductivity on the honeycomb bilayer", Phys. Rev. B 86, 214505

2011 - H. Terletska, J. Vučičević, D. Tanasković, V. Dobrosavljević: "Quantum Critical Transport Near the Mott Transition", Phys. Rev. Lett. 107, 026401

In final stages of preparation

H. Braganca, M. C. O. Aguiar, J. Vučičević, D. Tanaskovic, V. Dobrosavljević: "Effects of disorder induced localization near the Mott metal-insulator transition"

T.H. Lee, J. Vučičević, D. Tanasković, E. Miranda, V. Dobrosavljević: "Unstable solution of the Mott MIT coexistence region as the domain wall phase"

X.Y. Xu, J. Vučičević, Z.Y. Meng: "Cluster DMFT on a triangular lattice"

Conferences/presentations

"Mott quantum criticality and bad metal behavior", talk at the Institute of Physics, Chinese Academy of Sciences, 2014.

"Finite temperature crossovers and the quantum Widom line near the Mott transition", poster presentation at APCTP, Pohang, South Korea 2013

"Finite temperature crossovers and the quantum Widom line near the Mott transition", poster presentation at
Autumn School on Correlated Electrons, Julich, Germany 2013

"Quantum Critical Transport Near the Mott Transition", poster presentation at NGSCES 2012, Portoroz, Slovenia

"Quantum Critical Transport Near the Mott Transition", poster presentation at SFKM 2011, Belgrade, Serbia

Doctoral training

Autumn School on Correlated Electrons: *Emergent Phenomena in Correlated Matter*, Julich, Germany 2013

Les Houches Doctoral training: *Statistical physics*, Les Houches, France 2012

Advanced School on scientific software development: *concepts and tools*, ICTP, Trieste, Italy 2012

Autumn-School Hands-on LDA+DMFT: *Practical introduction to modeling strongly correlated matter*, Julich, Germany, 2011

Advanced School in High Performance and GRID Computing, ICTP, Trieste, Italy, 2009

European School on Magnetism: *Models in magnetism, from basic aspects to practical uses*, Timisoara, Romania, 2009

Прилог 1.

Изјава о ауторству

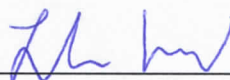Потписани-а   Јакша Вучичевић

број индекса   Д4/2009

Изјављујем

да је докторска дисертација под насловом

- резултат сопственог истраживачког рада,
- да предложена дисертација у целини ни у деловима није била предложена за добијање било које дипломе према студијским програмима других високошколских установа,
- да су резултати коректно наведени и
- да нисам кршио/ла ауторска права и користио интелектуалну својину других лица.

Потпис докторанда

У Београду,   26. мај 2015.

Прилог 2.

Изјава о истоветности штампане и електронске верзије докторског рада

Име и презиме аутора __Јакша Вучичевић_____

Број индекса _____Д4/2009_____

Студијски програм __Физика кондензованог стања материје

и статистичка физика_____

Наслов рада __Показатељи скривене квантне критичности у високо-температурном

транспорту наелектрисања у близини Мотовог прелаза___

Ментор ____др Дарко Танасковић_____

Потписани/а _____Јакша Вучичевић_____

Изјављујем да је штампана верзија мог докторског рада истоветна електронској верзији коју сам предао/ла за објављивање на порталу **Дигиталног репозиторијума Универзитета у Београду.**

Дозвољавам да се објаве моји лични подаци везани за добијање академског звања доктора наука, као што су име и презиме, година и место рођења и датум одбране рада.

Ови лични подаци могу се објавити на мрежним страницама дигиталне библиотеке, у електронском каталогу и у публикацијама Универзитета у Београду.

Потпис докторанда

У Београду, ___26. мај 2015._____

Прилог 3.

Изјава о коришћењу

Овлашћујем Универзитетску библиотеку „Светозар Марковић" да у Дигитални репозиторијум Универзитета у Београду унесе моју докторску дисертацију под насловом:

Показатељи скривене квантне критичности у високо-температурном

транспорту наелектрисања у близини Мотовог прелаза

која је моје ауторско дело.

Дисертацију са свим прилозима предао/ла сам у електронском формату погодном за трајно архивирање.

Моју докторску дисертацију похрањену у Дигитални репозиторијум Универзитета у Београду могу да користе сви који поштују одредбе садржане у одабраном типу лиценце Креативне заједнице (Creative Commons) за коју сам се одлучио/ла.

1.   Ауторство

2.   Ауторство – некомерцијално

3.   Ауторство – некомерцијално – без прераде

4.   Ауторство – некомерцијално – делити под истим условима

5.   Ауторство – без прераде

6.   Ауторство – делити под истим условима

(Молимо да заокружите само једну од шест понуђених лиценци, кратак опис лиценци дат је на полеђини листа).

Потпис докторанда

У Београду,   26. мај 2015.

1. Ауторство - Дозвољавате умножавање, дистрибуцију и јавно саопштавање дела, и прераде, ако се наведе име аутора на начин одређен од стране аутора или даваоца лиценце, чак и у комерцијалне сврхе. Ово је најслободнија од свих лиценци.

2. Ауторство – некомерцијално. Дозвољавате умножавање, дистрибуцију и јавно саопштавање дела, и прераде, ако се наведе име аутора на начин одређен од стране аутора или даваоца лиценце. Ова лиценца не дозвољава комерцијалну употребу дела.

3. Ауторство - некомерцијално – без прераде. Дозвољавате умножавање, дистрибуцију и јавно саопштавање дела, без промена, преобликовања или употребе дела у свом делу, ако се наведе име аутора на начин одређен од стране аутора или даваоца лиценце. Ова лиценца не дозвољава комерцијалну употребу дела. У односу на све остале лиценце, овом лиценцом се ограничава највећи обим права коришћења дела.

 4. Ауторство - некомерцијално – делити под истим условима. Дозвољавате умножавање, дистрибуцију и јавно саопштавање дела, и прераде, ако се наведе име аутора на начин одређен од стране аутора или даваоца лиценце и ако се прерада дистрибуира под истом или сличном лиценцом. Ова лиценца не дозвољава комерцијалну употребу дела и прерада.

5. Ауторство – без прераде. Дозвољавате умножавање, дистрибуцију и јавно саопштавање дела, без промена, преобликовања или употребе дела у свом делу, ако се наведе име аутора на начин одређен од стране аутора или даваоца лиценце. Ова лиценца дозвољава комерцијалну употребу дела.

6. Ауторство - делити под истим условима. Дозвољавате умножавање, дистрибуцију и јавно саопштавање дела, и прераде, ако се наведе име аутора на начин одређен од стране аутора или даваоца лиценце и ако се прерада дистрибуира под истом или сличном лиценцом. Ова лиценца дозвољава комерцијалну употребу дела и прерада. Слична је софтверским лиценцама, односно лиценцама отвореног кода.